Polymorphism of Organic Molecular Crystals

Dissertation

zur Erlangung des akademischen Grades

doctor rerum naturalium

(Dr. rer. nat.)

im Fach Physikalische und Theoretische Chemie

eingereicht an der

Mathematisch-Naturwissenschaftlichen Fakultät

der Humboldt-Universität zu Berlin

von

Dipl.-Chem. Thi Yen Nguyen

Präsidentin der Humboldt-Universität zu Berlin:

Prof. Dr.-Ing. Dr. Sabine Kunst

Dekan der Mathematisch-Naturwissenschaftlichen Fakultät:

Prof. Dr. Elmar Kulke

Gutachter/innen:	1. Prof. Dr. K. Rademann
	2. Prof. Dr. K. Balasubramanian
	3. PD Dr. U. Kolb
Tag der mündlichen Prüfung:	27. September 2017

Abstract

Crystallization is a complex process, which is used in different processes in the industrial production of various materials. The limited understanding about its fundamental mechanisms challenges the control of crystallization and influences the quality of the materials. The research of this work concentrates on the crystallization studies of organic model systems (active pharmaceutical ingredients) from different organic solvents in an acoustic levitator. This specific sample environment regulates the influence that solid surfaces, temperature, and humidity have on the crystallization process. The investigations were performed with *in situ* analytical techniques and theoretical simulations to gain a comprehensive insight into processes, occurring intermediates, and required reaction conditions. The results show that the model systems follow specific crystallization pathways different than those predicted by the classical nucleation theory. The crystallization proceeded via the evaporation of the solvent and the formation of characteristic amorphous phases (polyamorphism) into one crystalline structure of the compound. The targeted choice of the solvent and the concentration enabled the guidance of the pathways, therefore, resulting in the isolation of one desired crystalline structure.
The findings are of great interest and they help explain the crystallization mechanisms on a molecular level, which is a fundamental contribution for the optimization of manufacturing processes.

Kurzzusammenfassung

Die Kristallisation ist ein wichtiger Teilprozess bei der industriellen Herstellung vieler Materialien und Medikamente. Es ist jedoch ein vielschichtiger, physikalischer Vorgang, der noch nicht vollständig aufgeklärt ist.
Der Schwerpunkt dieser Arbeit liegt auf der Kristallisation von organischen, polymorphen Verbindungen aus unterschiedlichen Lösungsmitteln. Die Kristallisationsstudien wurden in einem akustischen Levitator mit Klimakammer, der den Einfluss von Temperatur, Feuchtigkeit und festen Oberflächen steuert, durchgeführt. Verschiedene analytische in-situ-Methoden und deren Kopplung kamen für die Analyse der Kristallisationsabläufe zum Einsatz. Als Unterstützung für die Interpretation der beobachteten Phänomene wurden unter äquivalenten Bedingungen Moleküldynamik-Simulationen vorgenommen.
Die Kristallisation der Modellverbindungen zeigte verschiedene spezifische Kristallisationspfade, die nicht dem klassischen Kristallisationsmodell entsprachen. Zunächst verdampfte das Lösungsmittel, was mit einer Konzentrationszunahme der Lösung und der Ausbildung von charakteristischen amorphen Phasen (Polyamorphismus) einherging, und schließlich trat die Kristallisation ein. Durch die oberflächenfreie Kristallisation wurde ausschließlich nur ein Polymorph ein- und derselben Verbindung als Kristallisationsprodukt isoliert. Die gezielte Wahl der Ausgangskonzentration und eines Lösungsmittels ermöglichte die Steuerung des Kristallisationsverlaufs hin zu einer gewünschten Kristallstruktur des untersuchten Materials.
Die Ergebnisse dieser Arbeit unterstützen das Verständnis über den komplexen Ablauf des Kristallisationsvorgangs, gleichzeitig zeigen sie weitere Ansätze auf, die Kristallisation zu untersuchen. Die neuen Erkenntnisse sind hilfreich bei der Optimierung der Herstellungsprozesse verschiedener Materialien.

Contents

List of Abbreviations

1D	one-dimensional
2D	two-dimensional
3D	three-dimensional
API	active pharmaceutical ingredient
approx.	approximately
CCD	charge-coupled device
CNT	classical nucleation theory
CPA	crystallization by particle attachment
CSD	Cambridge Structural Database
DSC	differential scanning calorimetry
DVS	dynamic vapor sorption
e.g.	exempli gratia
ESRF	European Synchrotron Radiation Facility
fs	femtosecond(s)
i.e.	id est
IMC	indometacin
IR	infrared
keV	kilo-electronvolt
LACC	liquid amorphous calcium carbonate

MD	Molecular dynamic
min	minute(s)
mm	millimetre
NIR	near-infrared
nm	nanometre
ns	nanosecond(s)
p.	page
PCM	paracetamol
PDF	pair distribution function
PNC	pre-nucleation cluster
ps	picosecond(s)
PSI	Paul Scherrer Institute
PXRD	powder X-ray diffraction
ROY	5-methyl-2-[(2-nitrophenyl)amino]-3-thiophenecarbonitrile
s	second(s)
S	saturation, $S = c/c_s$
SDF	spatial distribution function
TG	thermal gravimetric
TMS-DBC	7,14-bis((trimethylsily)ethynyl)dibenzo[b,def]-chrysene
WAXS	wide-angle X-ray scattering
XRD	X-ray diffraction

1 Introduction

One of the most interesting and one of the most difficult task is to link the relationship between physicochemical properties of materials and their crystal structures. The crystallization of solids is important in many geological, biological, and industrial processes and has been investigated for centuries.[1] Crystallization from liquid solution is the most widely applied method in fine chemistry and pharmacy because this single process combines both material formulation and purification.

The control of crystallization regarding the size, purity, morphology, and crystal structure is significant for the quality of materials. Nucleation is the first crucial step deciding on the crystal structure and size distribution. Therefore, understanding its fundamentals is an important challenge which has to be managed. Recent experimental and theoretical studies of solid nucleation in liquid solution suggest that crystallization not only proceeds following the classical theory, but rather follows more complicated routes. Intensive research activity resulted in various theoretical explanations for the molecular mechanism of crystallization in liquid solution. The following theories are currently discussed: the classical nucleation theory (CNT) and the non-classical crystallization pathways. The CNT states that the association of monomers leads to the formation of unstable species, whereas non-classical theories postulate the presence of different intermediates such as stable solute species in under- and supersaturated liquid solutions which participate by introducing a phase separation. The two-step model consists of the formation step of solute molecule clusters and a reorganization of these clusters into an ordered sequence. This is particularly the cases for macromolecules and small organic molecules. Despite considerable efforts, the understanding of nucleation and crystal growth,[2] and external influences on the crystallization process is still limited. Further analytical developments allow us to understand the crystallization process and the individual processes in more detail, and they help find the ideal conditions for the selective isolation of materials with desired features. A complete picture of the crystallization for the entire crystallization pathway must be issued to evolve the overall potential of many scientific disciplines.

The aim of this research is to study the crystallization process from liquid solution in more detail, identify the processes, and explain the observed phenomena on a molecular level. The results are expected to support the selective isolation of desired structures and to find the corresponding suitable conditions.
A specific solid-free sample holder, *in situ* analytical methods, and the combination of several others are used to investigate the crystallization process profoundly regarding the structural and kinetic aspects. Additionally, molecular-to-mesoscale modeling techniques supplement the crystallization examinations regarding insights into the nature of forces driving the crystallization, the role of surfaces, solvents, and saturations.
Especially, organic compounds are suitable for these crystallization studies. They are the basis of many industrial productions for drugs, pigments, polymers, or chemicals tend to form several polymorphs. The different structures with changed physicochemical characteristics can affect the quality and success of manufacturing processes. For this reason, knowing the structure-property relationship, the individual crystallization conditions for the required structure, and the energetics is crucial to optimize procedures and guarantee the materials' quality. That is why the studies are performed with crystal systems, which are diverse in structure pathways on one hand, and which allow the combination of the different analytical techniques on the other hand. The organic model systems 5-methyl-2-[(2-nitrophenyl)amino]-3-thiophenecarbonitrile (ROY), paracetamol, and indometacin were chosen for the crystallization studies from liquid solution. These compounds exhibit a large number of polymorphs and fundamental functional molecule groups. They offer diversity in investigations and allow the transfer of results to similar systems.

Strategy

To gain deeper insight into crystallization processes, especially from liquid solution, different aspects have to be investigated. In this work, the focus is on the crystallization control by using a custom-made acoustic levitator. This analytical tool enables the crystallization from liquid solution with conscious control of the surface, temperature, and humidity. In this way, the influence of the solvent, concentration, and saturation on the crystallization can be studied in more detail.
The crystallization process is investigated regarding the structural changes and kinetic aspects. This is done by means of time-resolved *in situ* X-ray scattering using synchrotron radiation, *in situ* Raman spectroscopy, gravimetric and thermoanalytical techniques. Wide-angle X-ray scattering (WAXS) provides information about crystalline phases and

the access to their crystal structures. In combination with synchrotron radiation, the fast acquisition of X-ray patterns to higher angles can be implemented. This enables the generation of pair distribution functions (PDFs) for studying the arising amorphous phases regarding their local structures. Raman spectroscopy as a complementary method renders the molecular vibrations of the materials, which gives information about the molecular conformations, inter- and intramolecular interactions between the molecules in solution, amorphous, and crystalline phases. This analytical method is also suitable for the detection of solvent amounts during the evaporation. The orthogonal coupling of both analytical methods, WAXS and Raman, allows the *in situ* characterization of the complete crystallization process from liquid solution via intermediate stages to the final crystalline form in the acoustic levitator. Additionally, theoretical computations are performed for selected crystallization scenarios to support the experimental results.

2 Literature Review

2.1 Crystallization

Crystallization is a fundamental part of natural processes (e.g. biomineralization, rock formation), industrial manufacturing, and scientific disciplines. Especially, in pharmacy and materials technology, the synthesis and purification of compounds based on crystallization are essential steps deciding the effectiveness of the active pharmaceutical ingredients (APIs) or the properties of a material. This leads to intense research activity to identify the underlying processes of crystallization processes. Thus, different theories for the crystallization process, including classical and non-classical pathways, can be found in the literature (see Figure 2.1, p. 6). The classical theory involves the formation of nuclei and crystals via monomer-by-monomer addition, whereas non-classical pathways comprise the concept of crystallization by particle attachment (CPA) for crystal growth, the binodal demixing/spinodal decomposition, the liquid-liquid separation, or the pre-nucleation clusters (PNCs) as first constituent units. The different pathways have high influence on the structure, morphology, and properties of the resulting crystalline solids. This basic knowledge about the individual crystallization processes allows the manufacturing control of requested materials with selective properties. Despite considerable efforts in research to date, the molecular mechanisms, especially, early stages at atomic and meso-scale are still insufficiently understood in order to manipulate processes reliably.[3] Two main steps in crystallization processes have to be considered: the nucleation[4–8] and the crystal growth[9–13].

2.1.1 Nucleation and crystal growth

Nucleation is the first step towards the crystallization. The constituents-atoms, ions, and particles aggregate to form crystal nuclei. According to the classical nucleation theory (CNT), the homogeneous crystallization of a nucleus in a supersaturated solution proceeds through stochastic random collisions of dissolved constituents (ions, atoms, molecules) and the resulting monomer unit. This nucleation is governed by the balance

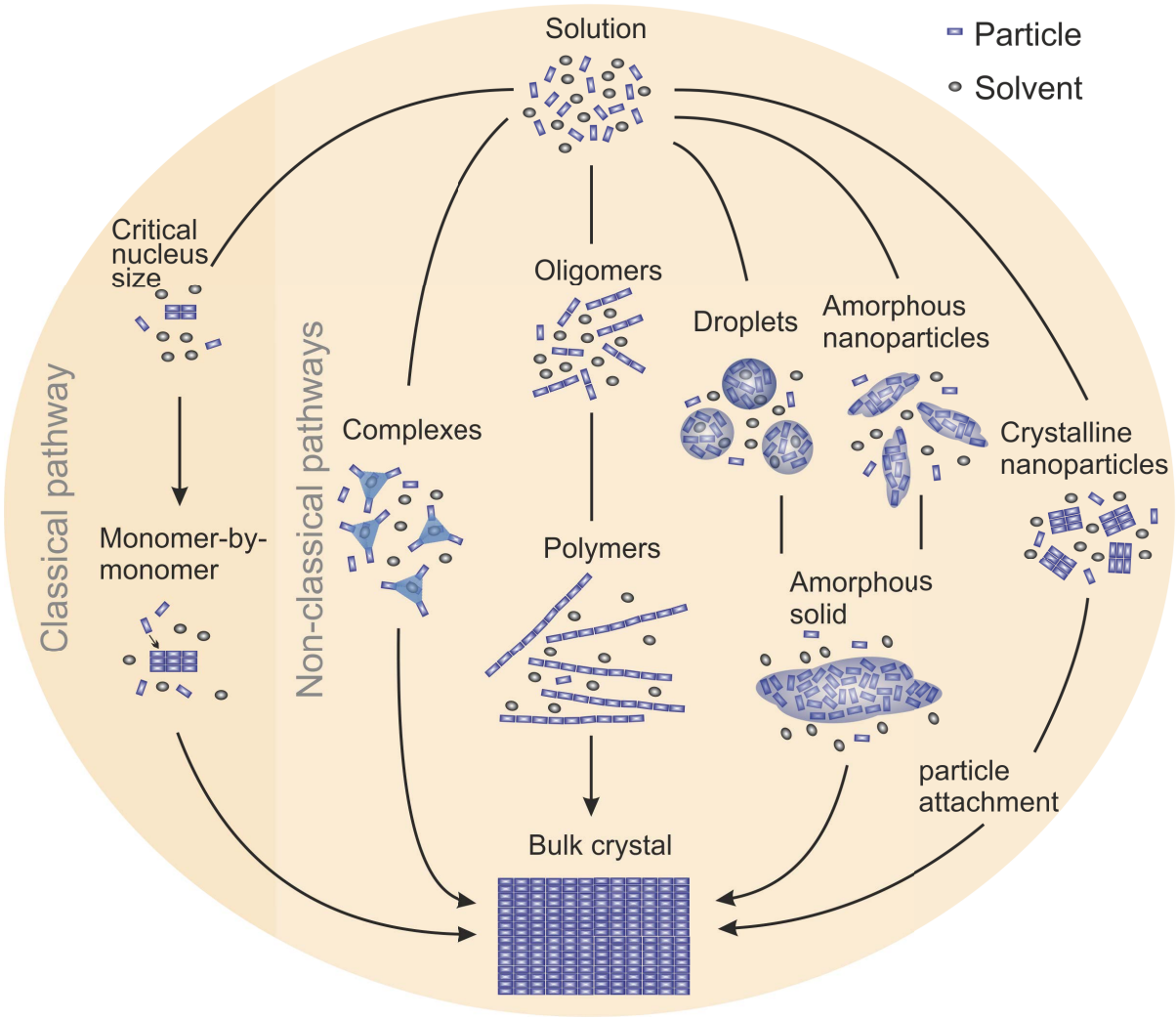

Figure 2.1: The graphical illustration demonstrates the diversity of crystallization pathways. The classical pathway proceeds via the formation of a critical nucleus size which grows through a monomer-by-monomer process to a bulk crystal. Bulk crystals arising from non-classical pathways can develop from various intermediates, such as complexes, oligomers, particle-rich liquid droplets, amorphous, or crystalline nanoparticles.

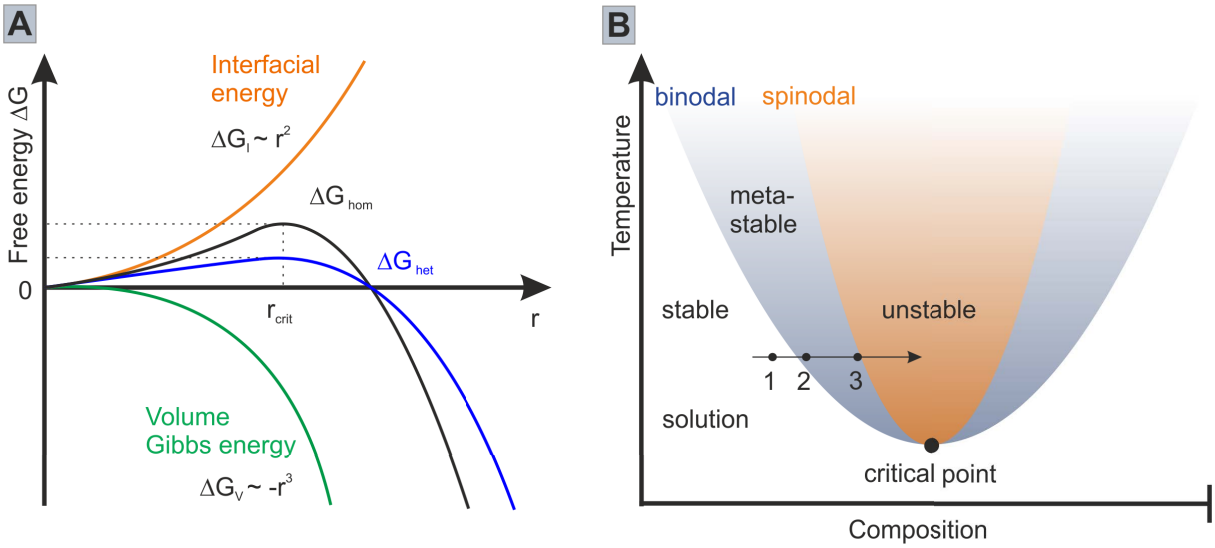

Figure 2.2: The graphical illustration shows the classical nucleation theory and the phase diagram for the spinodal demixing/binodal decomposition. A) In the classical nucleation theory, the free energy is given as a function of the radius r. The excess free energy is the sum of the interfacial free energy and the volume Gibbs energy. R_{crit} is the critical size where changes in radius decide on dissolution or crystal growth processes. B) The phase diagram of a two-phase system is divided into the solution, binodal, and spinodal area. Each area describes the stability of the system in dependent on the composition and temperature.

between two counteracting energies: the interfacial free energy and the volume Gibbs free energy between the liquid and crystal phases, both functions of the radius r (see Figure 2.2 A, p. 7). By assuming that the nuclei are spherical, the interfacial free energy with square of r as a contribution determines the formation of the nuclei at small r working as an energy barrier, while the stabilizing volume Gibbs free energy with cubic of the radius dominates the crystal nuclei at higher r. The sum of both contributions results in values of the excess free energy Δ_{hom}G of the nuclei (see Figure 2.2 A black line, p. 7). The r-value at the peak of the excess free energy is the critical nucleus size r_{crit} which corresponds to a metastable state. Any changes to the r_{crit} cause either the dissolution of the nuclei when going to small r, or the nucleus growth to a bigger crystal with the increase of r. The dependence of the excess free energy on the interface and volume implies a high energy barrier for a high crystal-liquid interfacial free energy, which allows the formation of high supersaturated and supercooled liquids. The crystal-liquid interfacial energy arises from configurational entropy differences between the crystal and liquid phases. Distinct differences in their local structural order between the crystal and the liquid phase lead to an increased interfacial energy and, thus, to a higher nucleation barrier.[14] Consequently,

the presence of interfaces in terms of impurities or container walls influences the height of the energy barrier. The provided surface lowers the crystal-liquid interfacial free energy (see Figure 2.2 A blue line, p. 7) and the energy barrier leading to an increase of the nucleation rate. The foreign surface has also a negative impact on the nucleation kinetics by reducing the effective nucleus surface for the incorporation of further constituents.[15] These cases refer to the heterogeneous nucleation.
According to the classical nucleation theory, crystal growth results from the monomer-by-monomer addition to form an isolated cluster. The terrace-ledge-kink model is assumed for this crystal growth.[12] The basic idea of this model involves the dependence of monomers' positions, being on the crystal surface, and the interactions to the neighboring monomers. Transition processes occur based on breaking und forming bonds. The classical nucleation theory was used to describe many experimental observations,[16–19] but it also shows limitations in several real systems, for example, when the structures of the nucleated phase and the final products are different. This fact becomes even more obvious, considering that the thermodynamic stability and the solubility change with dependence on the states and their sizes.[20] Further approaches explaining the crystallization are non-classical pathways. The diversity of these pathways is due to the complexity of free energy landscapes and the reaction dynamics which control the particles growing and their interactions. The particles involved in these approaches, such as multi-ion complexes,[21] amorphous phases,[22] dense constituent-rich liquid droplets,[23] crystalline nanoparticles,[24] oligomers,[25] polymers, or gels[26] are the basis for the crystal growth with assemblies of constituents through fluctuations or PNCs as previous steps. Regarding the phase diagram of a two-component system as a function of composition and temperature, three areas can be addressed with remarkable differences in stability and a critical solution temperature point (see Figure 2.2 B, p. 7). Along the arrow from left to right, the crystallization process starts from solution (outside the blue area, point 1) which is stable. The boundary between the stable and metastable section is marked by the binodal curve (point 2) describing the coexistence of the solid and liquid phase. Crossing the binodal curve and approximating point 3 by changing the conditions, the system becomes metastable and continuously more supersaturated. At this point, crystallization can occur. The described binodal demixing is a comparable description within the CNT going from undersaturated via saturated and supersaturated stage to the nucleation. In this range, the phase separation is based on the stochastic formation of small nuclei initiated by statistical fluctuations which are large in degree and small in extent.[27] The probability to overcome the nucleation barrier increases with growing supersaturation. The expanded

approach in the phase diagram includes the point 3 which lies on the spinodal curve and marks the boundary between the metastable and unstable regime. In many cases, crystallization occurs spontaneously and spreads throughout the whole volume of the system. Within the unstable area the barrier of the phase separation is negligibly low. The fluctuations are evanescent in degree and high in extent which leads to a diffusion-limited process with the loss of nucleus notion through the approachment of spinodal fluctuation centres and the surrounding solution. The particles are generated in such a large number that the growth of the crystalline phase by direct collision and coalescence with other particles dominates. This differs strongly from the binodal demixing and the CNT. Using the described illustration of the binary phase diagram, the liquid-liquid phase separation can also be explained with the main difference that the supersaturated solution divides into a solute-rich and -poor liquid phase. This assumption is of interest for the explanation of the crystallization of inorganic materials, where e.g. dense droplets rich in calcium carbonate act as liquid precursors during the precipitation of solid calcium carbonate. The formation of these liquid precursors in the metastable regime can be obtained by admixing polymer additives[23,28] or by increasing the supersaturation[29,30]. By entering the spinodal range, nanoparticles of amorphous calcium carbonate arises before the crystalline phase forms.[31] This kind of two-step pathway is also observed for proteins.[26]
The presented concepts explain the occurrence of phases, but the insights into molecular mechanisms are marginal. Furthermore, these concepts are not able to explain the existence of the pre-nucleation clusters (PNCs) in supersaturated and stable undersaturated areas of the phase diagram which was observed multiple times for biominerals and amino acids in recent years.[32] PNCs are small thermodynamically stable units of atoms, molecules, or ions showing no phase boundary between the clusters and the surrounding solution with a liquid-like character.[25] These highly dynamic molecular precursors precipitate through phase separation. Crystal growth can also proceed via further addition or particle attachment mechanisms (CPA), such as the molecular, cluster, or non-oriented attachment.[33] The CPA processes are significantly controlled by the interplay of free energy, surface energy, and reaction dynamics. The free energy determines the thermodynamic structure preference, morphology, and size distribution of the formed particles, whereas the surface energy influences the size of the free-energy barrier. The dynamic processes, monomer and particle diffusion and internal particle relaxation, decide on the progress proceeding through either the thermodynamically favored or the kinetically controlled pathway. A special case of the CPA is the oriented attachment where crystalline lattice-matched particles are added on specific crystal faces.[34] Crystals with pores or

branches can be formed through dendritic or spherulitic growth mechanisms.[35] Another particular kind of pathway proceeds according to the Ostwald's rule of stages describing the first formation of a thermodynamically metastable bulk phase which subsequently transforms into a more stable one.[36] Nonetheless, CPA mechanisms also have to compete with the concurrent process of Ostwald ripening.[37] This spontaneous process occurs because larger particles are energetically favored than smaller ones. Surface molecules detach from small particles via the Gibbs-Thomson relation and dissolve in solution leading to an increase of solution concentration.[38] The free molecules dock to the surface of larger particles, causing the small particles to shrink and the large particles to grow.
However, the reality of crystallization is even more complex with the sum of the mentioned processes and probably unknown procedures occurring concurrently. This is particularly evident from the knowledge gap regarding many experimental crystallization studies which connect the molecular information to larger growing units, the adaption for heterogeneous crystallization, or the explanation of polymorphism and polyamorphism (see Section 2.1.2). Further experimental investigations and theoretical computations are needed to get a more comprehensive and deeper understanding of early stages, the underlying crystal formation processes, and interactions.

2.1.2 Polymorphism and polyamorphism

Polymorphism is the ability materials have to form at least two different crystalline structures (polymorphs) with the same chemical composition (see Figure 2.3, p. 11). Polymorphism is relevant for many industrial sectors which handle crystalline materials including minerals, metals, polymers, or organic compounds. Polymorphism drew attention when it was discovered in pharmaceutical substances. First observations concerning polymorphism in organic compounds were described by Wöhler and Liebig as they were studying the reaction behavior of benzamide from boiling solution.[39] A slow cooling step produced silky-shinning crystal needles which transformed into rhombic crystals within days. Today, three polymorphs of benzamide are known differing in the π-π stacking between the benzamide molecules.[40] This example shows that the diversity in crystal structures resulting from the different packing in the bulk or the different conformers of the same constituent molecule. The fact is supported by weak directional and non-directional intermolecular interactions like hydrogen bonds, van der Waals interaction, or electrostatic dipole interactions within the crystalline material.[41–43] The polymorphs often feature minor differences in lattice energies. Therefore, spontaneous conversions from a less stable form to a more stable form can occur following the Ostwald's rule of stages.[44] If these

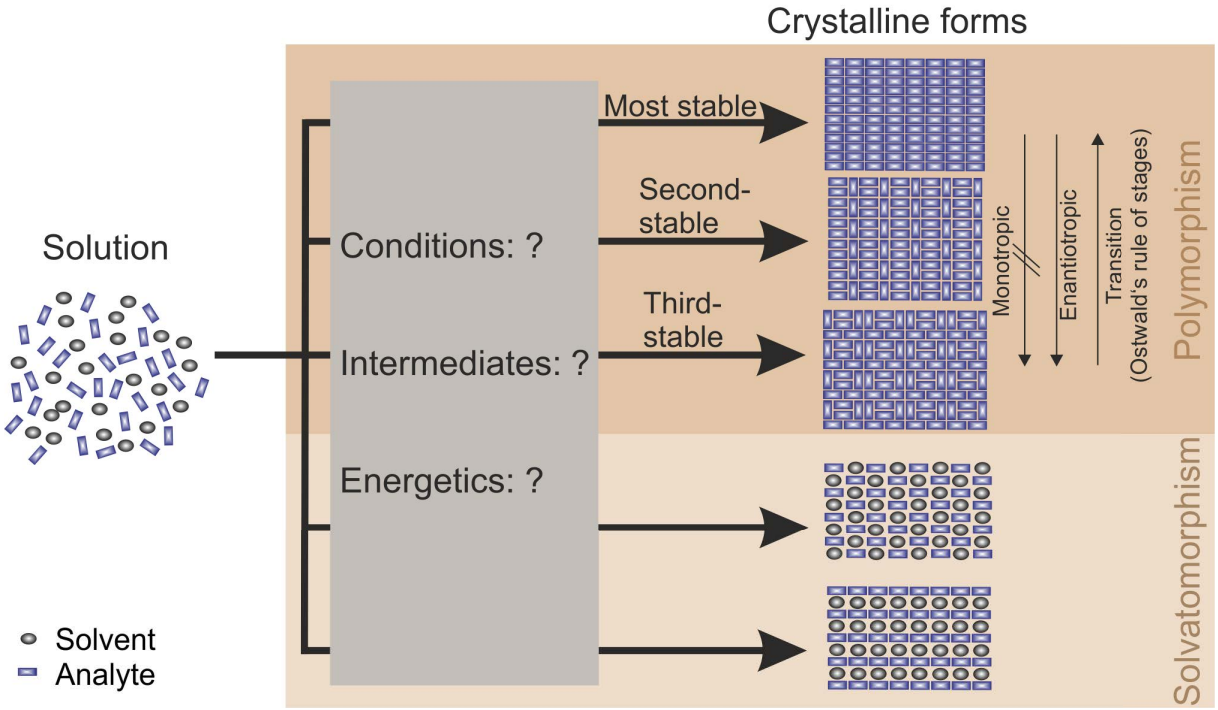

Figure 2.3: The picture illustrates the formation of polymorphs and solvates from liquid solution.

transitions are reversible without passing through the liquid or the gaseous phase, the system is enantiotropic. This differs from monotropic systems, which exhibit irreversible conversions. The marginal variations in the lattice energy among polymorphs can have a tremendous impact on the physicochemical properties of the crystalline compound, e.g. stability, melting point, or solubility. In the special case of active pharmaceutical ingredients (APIs), the individual crystalline form can have an influence on the effectiveness of the drug or the bioavailability due to changes in solubility. The antiviral drug ritonavir reflects the dramatic effect of polymorphism where different conformational molecule structures form different packing arrangements resulting in an inactive and active polymorph. On contact, the more stable inactive form converts the active to the inactive form demanding a change of the manufacturing formulation.[45]

Slight changes in the crystallization environment can push the process to a certain direction, and thus to the formation of a certain polymorph with target properties. Such environmental modifications can be implemented by the choice of the solvent, the used crystallization concentrations, or the presence of the solid surface, temperature, or humidity (see Section 2.1.3). These variations can change the pathways and the occurring interstages.

Amorphous phases are possible intermediates with the same ability for having more than one amorphous phase for the same compound.[46–48] Amorphous phases, i.e. glasses, amorphous solids, or supercooled liquids, lack long-range periodic molecule ordering, but they show significant differences in the local structure at interatomic scale. These short-range variations even cause distinctions in properties. In pharmaceutical science, the increased solubility of this metastable form of APIs is often used to gain increased bioavailability. A definition of polyamorphism given by Hancock *et al.* states that the presence of true polyamorphism prerequisites the existence, or usually coexistence, of two or more condensed amorphous phases separated by a clear phase transition.[49] Polyamorphism was reported for ice with different amorphous states which have different densities at ambient and high pressure,[50] inorganic compounds,[51,52] and alloys.[53] However, the detection of these unstable intermediates is very difficult or can be overlooked because of the high dynamic of the systems.[16] The theory based on the PNC concept might be capable to explain the polyamorphism in inorganic materials.[32] Computer simulations provided information regarding the structure, the molecular mechanisms of PNCs, and the following phase separation process. In recent years, polyamorphism in organic materials gets in the focus of scientific research. Citing the example of carbonic acid, two distinct amorphous states were found which have already showed infrared (IR) spectra features of the subsequently crystallizing polymorph. This fact indicates that hydrogen bond connectivity and conformational state of the polymorphs are imprinted in the amorphous precursors leading to a correlation between amorphous and resultant crystalline phase.[54] Due to the overlapping of intra- and intermolecular distances, the analytical limitations hamper the determination of amorphous structures in organic compounds.

Besides polymorphism and polyamorphism, the crystallization from liquid solution also evokes solvatomorphism where different crystal forms (solvates) of the compound containing additional solvent molecules arise.[55] The phenomena of polymorphism and polyamorphism still provide a wide scope for research activity, because they are not understood completely. McCrone has concluded that ‘every compound has different polymorphic forms, and that, in general, the number of forms known for a given compound is proportional to the money spent in research‘.[56] This statement applies to both the crystalline and the amorphous phases.

2.1.3 Homogeneous nucleation under acoustic levitation

The goal is to control specifically the progress of crystallization and, therefore, one of the most important part is to identify the influencing parameters and manipulate them. One main interest is the study of nucleation processes over a wide range of low and high supersaturation. To access these levels of supersaturation, homogeneous nucleation has to be warranted and any surfaces which might act as heterogeneous nucleation sites have to be circumvented. The implementation of a genuine homogeneous nucleation under ambient condition is demanding due to the present of impurities, vessel walls, and gravity. Previous ways to limit the role of surfaces on crystallization process from solution included the division of the sample into tiny portions that most of them do not contain heterogeneous nucleation sites. Another possibility is to generate conditions where the nucleation rate is high and the crystal growth rate is low. However, these methods are complicated and the application is not suitable for each system.

The use of strong acoustic fields for particle manipulation is a widely used technique for many applications. The ever increasing technical finesse in generating and shaping ultrasonic fields has introduced tools, such as ultrasonic motors[57], and contactless sample holders for sensitive materials[58] that go into large scale product processing. While there are various methods, as the magnetic, electrostatic or aerodynamic levitation, acoustic levitators generating an ultrasonic standing wave for the containerless levitation of objects have gained considerable interest in the past few years. The straightforward technical implementation and the minimal sample requirements are the reasons for the wide range of application in analytical chemistry and material processing.[59–61] The crystallization experiments in this research are performed in a custom-made acoustic levitator consisting of three main components: the sonotrode, the reflector, and an atmosphere control unit (see Figure 2.4, p. 14).[62] This device works in the most commonly used single axis geometry, where a transducer and reflector are arranged in a coaxial fashion, sharing the same axis of cylindrical symmetry. The sonotrode is an ultrasound transducer transforming the alternating voltage into mechanical waves with a piezo-electric crystal. This crystal works with an oscillating frequency of 58 kHz. A concentric reflector reverberating the longitudinally expanding ultrasonic waves locates on the opposite side of the sonotrode. Thus, a standing wave with several sound pressure nodes emerges by adjusting the distance between the sonotrode and the reflector resulting in a multiple of half the used wavelength. The Bernoulli effect, which describes the correlation between the velocity increase and the pressure decrease during the flow of gases, induces radial and axial forces. These forces hold liquids and solid samples in a fixed, levitated, and contactless position.

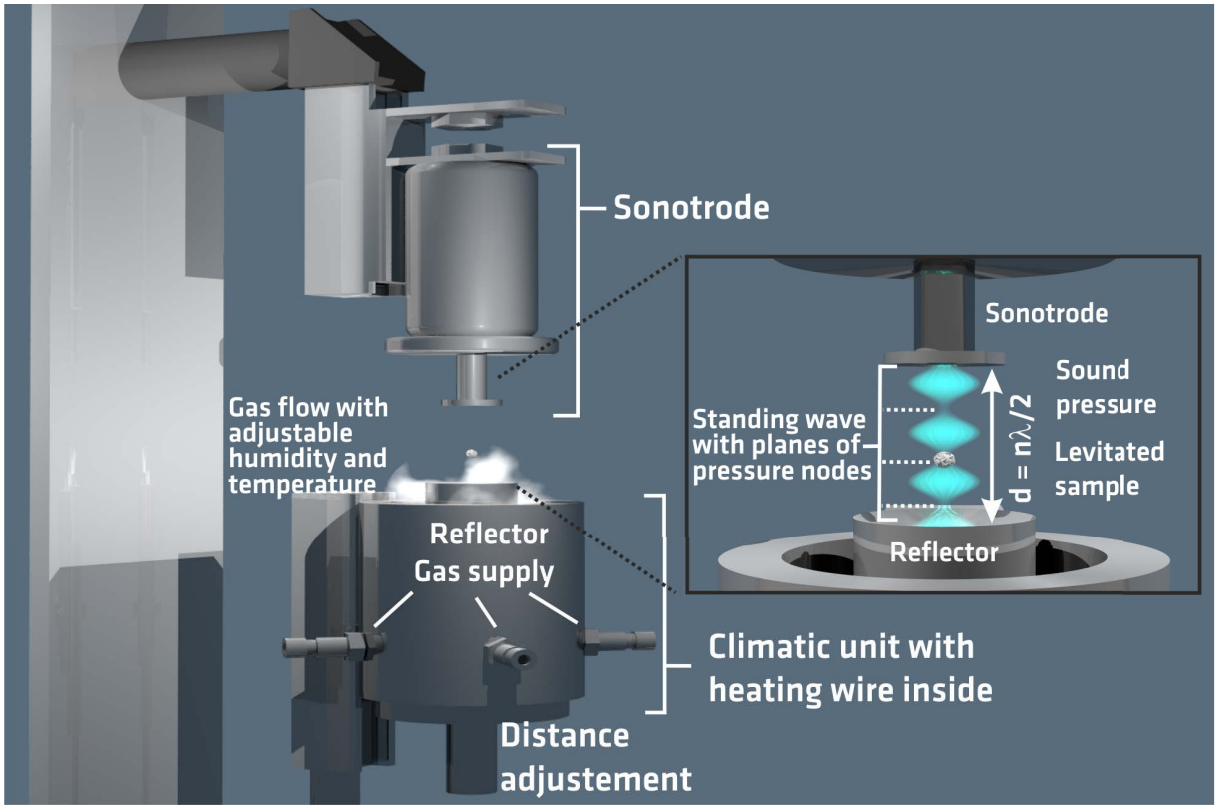

Figure 2.4: The acoustic levitator serves as a contactless sample holder. The device has three main components: the sonotrode, concentric reflector, and the control unit. The sonotrode emits the ultrasonic field which is deliberated by the reflector resulting in a standing wave with pressure nodes.

Droplets of liquids are transferred in the levitator by using a pipette. The size of the droplet is a function of the wavelength and can reach a maximal diameter of half the used wavelength. The maximal volume is dependent on the surface tension and the specific density of the liquid.[63] The acoustic levitator is used as a method to hold liquids and solid samples.[59] This technique uses the ultrasonic frequencies to position materials containerless in a fixed gaseous environment.[29,64–71] The special control unit allows the influence of the humidity and temperature of the sample surrounded by introducing a heatable/coolable nitrogen gas flow, which is tempered with the control device and can keep dust and impurities away from the sample. In view of recent studies, this is important for the crystallization control. Molecular dynamics simulations of titanium dioxide demonstrated the influence of humidity on the mediating particle interactions and the particle attachment event.[72] In vacuum, nanocrystalline titanium dioxide merges along its direction of approach forming a polycrystalline structure. However, the presence of water molecules with a high moisture content causes a reorientation of the nanocrys-

tals resulting in an aggregation process via the oriented attachment to develop a single crystal. Another example presents the strong impact of the temperature on the polymorphic structures. The synthesis of 7,14-bis((trimethylsily)ethynyl)dibenzo[b,def]-chrysene (TMS-DBC) and the following purification by growth of single crystals from solution and vapor deposition indicated the dramatic influence of the substrate temperature on the resultant polymorphs of TMS-DBC: fine red needles with 1D slipped-stack motifs at low temperature and large yellow platelets with 2D brickwork structures at high temperature.[73] By means of electronic-structure calculations, a distinct mobility property of the polymorphs was proven which affects the charge transport and is a strong interest in electronic applications. Besides the temperature and humidity, the nature of the used solvent is also crucial for crystallization pathways. Nifedipine which has the polymorphs α,[74] β[75], and γ[76] interacted strongly with solvents leading to different progresses. By using acetone or ethanol, hydrogen bonds between the solvent and solute were formed and the thermodynamically stable α polymorph arose including the β form as an intermediate.[67] The solvents dichlormethane and acetonitrile were not able to satisfy such interactions, so that the glassy modification is formed intermediately prior to the crystallization of the α form. These observations are consistent with the Ostwald's rule of stages.
The examples demonstrate the importance of crystallization control by the consideration of formation conditions and surfaces. The different crystallization theories imply surfaces as a controlling parameter of crystallization pathways for the simple reason that they lower the barriers to nucleation by reducing the interfacial free energy.[77] Holding samples in terms of levitated droplets is a good approach to avoid the interference with solid surfaces from vessels and, therefore, eliminates this parameter from the crystallization process. Additionally, the higher interfacial free energy of the droplets ensures achieving highly supersaturated systems where processes are comparable with genuine homogeneous nucleation processes. Thus, the acoustic levitator is an ideal analytical tool to control the reaction pathways by the selective setting of the crystallization environment, and it provides the possibility to perform homogeneous crystallization.

2.2 Monitoring of crystallization processes

The phenomena polymorphism, polyamorphism, and their formation processes need clarification by experiments. This leads to strict monitoring and phase screening during the crystallization process to identify and characterize the states. The investigation of the crystallization and the observed phenomena require the application of different analytical methods, which are able to characterize this process structurally and kinetically, to gain comprehensive information.

2.2.1 X-ray scattering

The most commonly used method to study and identify the structure of crystalline solids is the X-ray scattering analysis. Crystal structures of organic compounds can be assigned distinctly. This analytical method is based on the electromagnetic wave nature of X-rays with a wavelength in the range of atomic dimensions (10^{-8}–10^{-12} m) and the resulting interference effects with crystal lattices.[78] The structural information of a crystalline solid is accessible via the Bragg's law.[79]

$$2d_{\mathrm{hkl}}\ sin\ \theta = n\ \lambda, \tag{2.1}$$

where d_{hkl} is the interplanar spacing of parallel diffracting planes, θ the incident angle, n an integer, and λ is the wavelength of the incoming X-ray beam. This physical law postulates the diffraction scattering of X-ray radiation as a reflection of waves on a set of lattice planes. In crystallography, the planes in the crystal lattices are characterized by integers h, k, and l, the so-called Miller indices. The distance between the planes is determined by d_{hkl}. Thus, a prerequisite for the X-ray diffraction (XRD) analysis on the basis of the Bragg's law is the existence of a well-ordered crystalline solid consisting of several unit cells, typically more than ten per edge. The structure of crystalline solids can be described by means of their unit cell. The unit cell contains atoms arranged in the three-dimensional space, and it is determined by its lattice parameters, which are the lengths of the cell edges (a,b, and c) and the angles between them (α, β, and γ). The included atoms have defined atom positions. The bulk arrangement of the crystal structure results from stacked unit cells along the edges. The X-ray radiation penetrates inside the material where the atoms' electrons scatter the X-ray in the form of secondary spherical waves (elastic scattering). The scattered waves can cancel (destructive interference) or reinforce (constructive interference) each other determined by the equation (2.1). Constructive interference occurs when the path-length difference is an integer multiple of the wavelength

λ resulting in the formation of diffraction maxima. This is true for defined θ values. The disadvantage of the Bragg's law is the missing information about the spatial orientation of the planes, the incident, and scattered waves. This consideration requires this equation in the mathematical vector expression

$$\vec{k} = \vec{k}_1 - \vec{k}_0 = \vec{K}_{h,k,l} \tag{2.2}$$

with $\vec{k}_0 = \frac{\vec{s}_0}{\lambda}$ as the incident wave, $\vec{k}_1 = \frac{\vec{s}_1}{\lambda}$ the scattered wave, $\vec{K}_{h,k,l}$ the vector of the reciprocal lattice, $\vec{k}$ the diffraction vector, $\vec{s}_0$ and $\vec{s}_1$ as the corresponding unit vectors. Using this formulation and the Ewald's sphere model, which considers the real and reciprocal space of a sphere (see Figure 2.5, p. 18), spatial extension is provided. The examined crystal is the origin O_1 of the Ewald sphere with a radius of $\frac{1}{\lambda}$ which means that all wave vectors $\vec{k}$ with $\left|\vec{k}\right| = \frac{1}{\lambda}$ are on the surface of the Ewald sphere. The origin O_2 of the corresponding reciprocal space is the point of intersection of the Ewald sphere and the primary X-ray beam $\frac{\vec{s}_0}{\lambda}$. All planes whose reciprocal lattice points intersect with the Ewald sphere satisfy the Bragg's law. From a mathematical point of view, this corresponds with the vector difference $\vec{K}$ of the incident and the diffracted X-ray beam. The rotation of the crystal around the origin O_1 in the real space means a simultaneous rotation of the reciprocal lattice around the origin O_2 of the reciprocal space. This fact leads to a probability increment of finding reciprocal lattice points on the interface of the Ewald sphere. Here, each lattice point of the reciprocal space represents another set of planes.

However, Bragg's law shows limitation regarding the characterization disordered materials, such as liquid solutions or amorphous phases. The X-ray radiation also lends itself well to the characterization of non-crystalline amorphous phases. This approach is called total scattering analysis utilizing not only Bragg scattering, but also the diffuse scattering from the material in order to look beyond the average structure to examine the local short-range structure. Zernike and Prins derived the mathematically basis for this analysis by considering the atom pair correlation function and the isotropically averaged scattering function for a two-atoms molecule.[80] Taking the arrangement of electrons in atoms, atoms within a molecule, and between different molecules into account, the Fourier transformation resulted in G(r),

$$G(r) = 4\pi[\rho(r) - \rho_0] \tag{2.3}$$

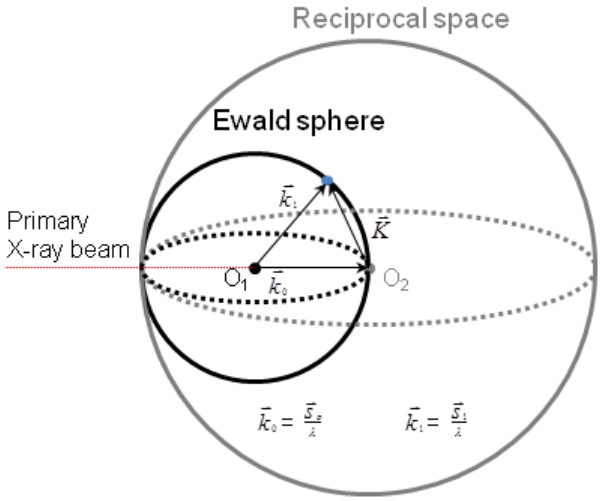

Figure 2.5: The Ewald sphere model describes the relationship between the wave vectors of the incident and diffracted X-ray beam, the diffraction angles, and the reciprocal lattice.

$$G(r) = \frac{2}{\pi} \int_0^\infty Q[S(Q) - 1] sin\ (Qr)\ dQ, \tag{2.4}$$

where ρ(r) is the microscopic pair density, ρ_0 is the average number density, and Q the momentum transfer. S(Q) is the normalized structure function determined from the experimental diffraction intensity.[81]

To perform total scattering or *in situ* XRD experiments with high time resolution for studying processes, synchrotron energy, an electromagnetic radiation generated in a cyclic particle accelerator, is needed. The experimental basic observation of this radiation phenomenon was made by Heinrich Hertz in 1888.[82] Pomeranchuk and Ivanenko described the first corresponding fundamental theory[83] after studying the entrance of cosmic electron rays in the earth's magnetic field and the resulting emission effect.[84] In 1947, a bright light was detected as a side effect at one of the first electron accelerator and from that time the radiation was named after it, the synchrotron radiation. This kind of radiation arises by deflecting accelerated electrons in a magnetic field, and it propagates tangentially to the propagation direction of the accelerated electrons. The radiation has a high flux and brilliance. The highly energetic radiation allows measuring of highly angle resolved XRD data in very short time intervals. Synchrotron institutions, such as BESSY II or the European Synchrotron Radiation Facility (ESRF), provide different beamlines modifying the raw synchrotron X-ray beam for the variety of requirements of scientific experiments. The construction of a beamline is divided in three main parts: the

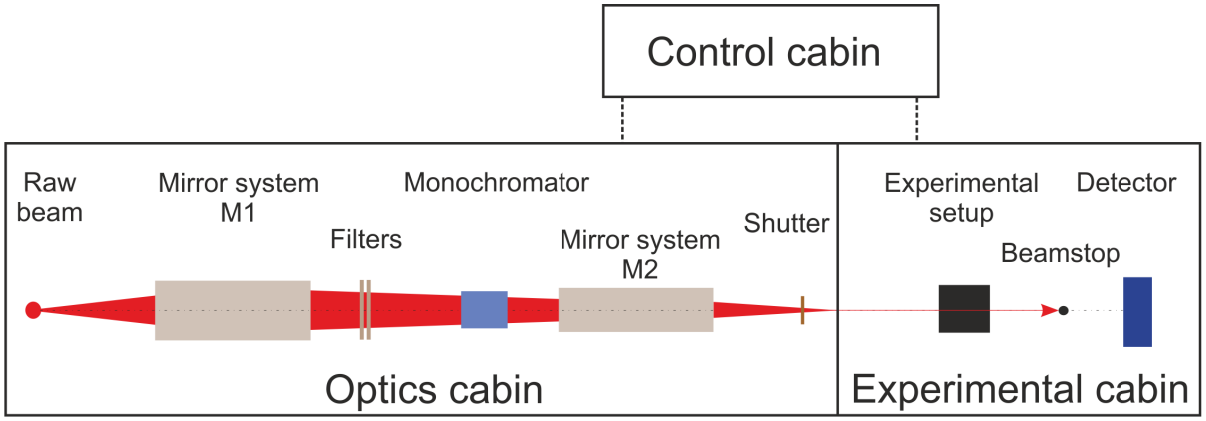

Figure 2.6: The general construction of a beamline at a Synchrotron facility is divided in the optics, experimental, and control cabin.

optics, experimental and control cabin (see Figure 2.6, p. 19). The optics cabin consists of specialized mirror systems, filters and crystal monochromators to focus and select the desired wavelength. The focused beam passes from the optics cabin to the experimental hutch where the setup of the experiment with the sample is established. Around the setup is a detector which records the scattered signals of the sample. The beamstop protects the detector against damage from the primary X-ray beam. The device control in the optics and experimental cabin, the beam adjustment, the acquisition and analysis of data are carried out in the control area by adapted softwares.

By means of the described theory and the Bragg's law, the XRD analysis became a powerful tool to determine crystalline phases. In the following years, many structures of inorganic elements[85–88] and more complicated inorganic compounds were determined by using the XRD phenomenon.[89] The structure solution of organic compounds was more difficult to implement because additional information, such as the symmetry of the carbon atom, the nature of the aliphatic chain, and the aromatic ring had to be considered. The great effort of scientists, especially Desmond Bernal and Dorothy Hodgkin, in further advanced development overcame the problems and the structure of biologically interesting molecules, including sterols, penicillin, vitamin B_{12}, and insulin were determined.[90] In 1953, Watson and Crick described the deoxyribonucleic acid (DNA) with its two entwined helices and paired organic bases.[91] The more complex the structures of compounds were, the greater became the data volume and complexity of the XRD patterns which have to be dealt with. Along with the rapid computer and software development in the last decades, new direct methods with the automation of many steps for XRD analysis were presented. Together with the advanced technique of diffractometers,

it caused an immense stream of new structures, which provided a vast primary base for crystallography, crystal chemistry, and quantum chemistry.
The widespread use of synchrotron radiation and the improved technical circumstances lead to the increase of total scattering experiments through the analysis of the PDF which considers the Bragg and the diffuse scattering of materials. Especially, it is used to study disordered systems. Crucial works were made by Warren and coworkers, who presented structural features of vitreous silicate by means of extensive calculations with Fourier transformed data.[92,93] With the development of computers, their performances, and the data analysis procedure, the Fourier transformation is easier to manage, so that the application of this technique has grown immensely.[94,95] Problems of the data quality, such as termination ripples and further artifacts coming from improper data normalization, could be solved. The solution is the data acquisition of q-values over a sufficiently wide range. This was realized in the late 1980's when spallation neutron and synchrotron sources with high energy and high flux became available to obtain a high maximum momentum transfer Q_{max} and, therefore, accurate PDFs with a high resolution and a reduced loss of elastic scattering intensity at high Q.[96,97] Combining these technical specifications with computer-based structural modeling and the development of two-dimensional (2D) image-plate detectors to collect data, qualitative and quantitative information could be gained within a very short time range.[98] The PDF analysis has proven to be successful in the structural analysis of amorphous, crystalline inorganic materials, and nanocrystalline compounds,[99,100] but its application to molecular organic systems has been used in few cases. The challenge is to model self-consistently the PDF by describing correctly the variety of bonds with extreme differences in strength including the covalent bonds, hydrogen bonds, electrostatic, and van der Waals interactions. The qualitative analysis of PDFs of organic compounds up until now consists of the data comparison by the visual inspection of measured and calculated reference curves.[101] In this way, structural information, such as arrangement of neighboring molecules or packing patterns, in poorly crystalline organic pharmaceutical compound was extracted. In 2015, Prill and coworkers achieved their first success in the refinement of organic PDFs with a good fit by introducing two different isotropic displacement parameters: one for the strong correlated intramolecular motions between atoms − the other one for the less correlated intermolecular distances.[102] But quantitative PDF analysis is still challenging, especially, when it comes to molecules with high internal degrees of freedom increasing the complexity of the data interpretation.

Combination of X-ray scattering with acoustic levitation

First experiments using the X-ray analysis in combination with an acoustic levitator to study the crystallization consisted of sample preparation steps and *ex situ* diffraction investigations, which were executed in succession. Nagashio *et al.* investigated the containerless processing of the $Y_3Al_5O_{12}$ by combining aero-acoustic levitation with a CO_2 laser irradiation system.[103] The crystallized compounds were characterized in *ex situ* powder X-ray diffraction (PXRD) experiments. To study the crystallization, the *in situ* approach provides a more detailed insight into ongoing processes. However, conventional laboratory diffractometers have X-ray tubes for generating the X-ray radiation whose properties enable measurements of XRD patterns within several hours. Therefore, the *in situ* XRD studies use synchrotron radiation for the record of XRD data within a few tens of seconds. So, preliminary test regarding the feasibility of synchrotron radiation for the *in situ* XRD experiments in combination with the acoustic levitation were carried out by Kloo and coworkers.[104] Emmerling *et al.* pioneered in the implementation of the acoustic levitator as a sample holder for hovering droplets in a synchrotron beam.[64] They performed *in situ* XRD experiments with a time resolution of 30 s providing a continuous set of XRD data for the crystallization of sodium chloride from solution. With the similar setup the detection of the non-classical crystallization pathway of the calcium carbonate system involving a liquid/liquid phase separation and an emulsified of a highly hydrated liquid amorphous calcium carbonate (LACC) succeeded.[29] The LACC developed from pure, neutral, and saturated calcium bicarbonate solution, and it crystallized homogeneously in acoustic levitation. Besides the XRD experiments, the identification of the liquids and amorphous phases required the X-ray absorption and the electrospray ionization mass spectrometry (ESI-MS). These characteristic amorphous intermediates were stabilized electrostatically, and they behaved like a classical emulsion.[30] Extended studies with additives resulted in destabilization phenomenon of LACC precursor using lysozyme, whereas the glycoprotein ovalbumin stabilized this transient state, which carried a negative surface charge, and prevented undirected mineralization of the egg-shell.[105]

2.2.2 Raman spectroscopy

In order to investigate the crystallization, the structure of crystalline, or amorphous organic materials, Raman spectroscopy is a good alternative enabling both non-contact diagnostics and *in situ* monitoring. Raman spectroscopy allows the distinction between crystalline and amorphous phases showing different vibrational signals. This analytical method uses the inelastic scattering, the Raman scattering, which arises when electromagnetic radiation interacts with molecules, to characterize materials and determine their properties. The result is a shift of the initial energy which gives information about characteristic processes, such as rotation or vibrational modes, of the material. The theoretical prediction of the Raman scattering was already described in 1923 by SMEKAL.[106] K. S. KRISHNAN and C. V. RAMAN proved this phenomenon with experiments in 1928. The method uses laser (light amplification by stimulated emission or radiation) light with a wavelength in the range of 100-1064 nm. This monochromatic, electromagnetic radiation has high coherence and intensity, and low divergence which is ideal for scattering experiments.

The classical theory for the Raman scattering assumes the induction of a dipole moment which is initiated by the electric field of the electromagnetic radiation. This means that the electrons and nuclei of the molecules move to opposite directions within the electric field and a polarizability is achieved. As the result, the induced dipole moment, which is proportional to the electric field strength, oscillates with the same frequency of the incident radiation v_0 which is the reason for the elastic Rayleigh scattering (see Figure 2.7, p. 23). The irradiated molecules themselves exhibit mechanically natural oscillations affecting the form of the electron clouds and, thus, the polarizability of the molecules. The resulting modulation of the imposed dipole vibration by its natural molecule oscillation leads to two additional wavelengths in the scattered spectra, the Stokes and Anti-Stokes Raman scattering. Both kinds of scattering are shifted in frequency, either with an energy loss or an energy gain ($hv_0 \pm hv_r$). The Stokes scattering illustrates the virtual stimulation of the molecule from its basic energy state and the following molecule relaxation from the virtual intermediate energy state onto the first excited energy state which results in an energy loss of $hv_0 - hv_r$. In case of the Anti-Stokes scattering, the molecule is stimulated onto the first excited energy state by the photons of the primary radiation and, subsequently, relaxes to its basic energy state leading to an energy gain of $hv_0 + hv_r$. Due to the low occupation of the first excited energy state in comparison to the basic energy state at ambient temperature, the Stokes scattering is much more intense. That is why the Stokes scattering is recorded at Raman experiments. By means of the Boltzmann distribution

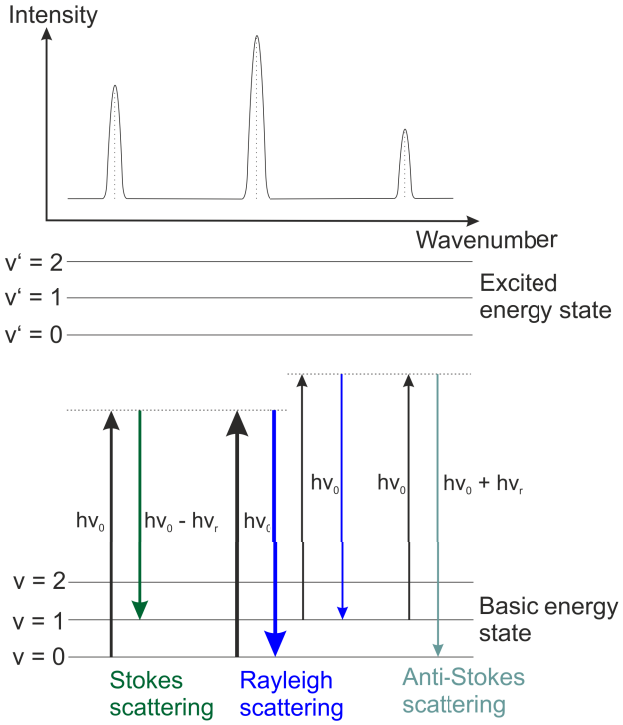

Figure 2.7: The graphic illustrates the different scattering types Rayleigh, Stokes, and Anti-Stokes scattering when materials are exposed to laser radiation.

(2.5) including a temperature dependence, the probability p of the occupation can be determined.

$$p = e^{-\frac{hv}{kT}} \tag{2.5}$$

The application success of Raman spectroscopy is often dependent on the excitation properties, such as the wavelength of the used laser. Usually, continuous wave lasers are used for analytical Raman spectroscopy. The development of the near-infrared laser enabled the elimination of interfering fluorescence which was demonstrated by Hirschfeld and Chase.[107] Since that time, Raman spectroscopy has a wide application in many scientific and industrial fields.

Raman spectroscopy combined with acoustic levitation

First experiments using the combination of Raman spectroscopy and the acoustic levitator were carried out on crystallization phenomena in levitated droplets where the wall-less conditions were used for homogenous nucleation and undercooling of the melt.[108] More recent studies used the coupling of Raman and levitated droplets for the investigation of L-cystein and tris-(hydroxymethyl)-aminomethane crystallization,[109] evaporation and

crystallization of salt/water solutions. For $(NH_4)_2SO_4$ the co-existence of the aqueous and the crystalline state of $(NH_4)_2SO_4$ was observed, and for Na_2SO_4 an intermediate state of $Na_2SO_4 \cdot 10\ H_2O$ has been determined.[110] In the same study, the coupling of Raman spectroscopy and acoustically levitated droplets was systematically tested regarding the droplet form, and the distance between microscope objective of the Raman system and the droplet. The highest Raman intensities were observed when the focus of the incident laser beam was in the middle of the droplet; apart from this effect the intensity was independent of the droplet form.[110] An influence of the droplet form was observed previously, where the Raman intensity was much higher for elliptical droplets compared to spherical ones.[111] This has been applied to study not only crystallization processes but also reactions and transformation processes. Variations in Raman spectra were observed for Aberchrom 540 fulgide while exposed to UV radiation.[109] Online monitoring using Raman spectroscopy was applied during the polymerization of acrylic acid and phenol.[112] The Knoevenagel reaction as an organic model reaction has been monitored in a levitated ionic liquid, well-suited solvents for wall-less microreactors due to their extremely low vapor pressure.[113]

Raman spectroscopy combined with X-ray scattering

The described examples highlight the potential of the powerful analytical methods to study the crystallization. A new experimental approach based on the combination of X-ray scattering, spectroscopy, or microscopy method hold promise for obtaining more detailed information about structural changes and dynamics during crystallization. Coupled time-resolved XRD and Raman spectroscopy were established for crystallization studies of pharmaceuticals.[67] This setup enables investigation of intermediates, phase transitions, and crystal growth during the crystallization from different solvents. The time-resolved data imaging indicates kinetics of processes. In order to investigate the structure of transient crystalline or amorphous intermediates Raman spectroscopy enables *in situ* monitoring of the crystal formation and transformation from one polymorph to another. Using this combined approach the authors succeeded in elucidating the crystallization process of the pharmaceutical nifedipine from different solvents, and the influence of the solvents on the crystallization. The crystallization ofthe thermodynamically stable α polymorph proceeds including the β form of nifedipine as an intermediate whenever the formation of hydrogen bonds between solvent and solute is possible. When such interactions are not given, the glassy modification is formed intermediately.
The promising experimental setup with combined X-ray scattering, Raman spectroscopy, and the acoustic levitator as the sample holder is used for the crystallization processes of

the organic model in the present work. This experimental setup is capable of providing comprehensive and simultaneous information from complementary analytical methods in a single experiment.

2.2.3 Thermal analysis

Besides the structural investigation of the crystallization process and occurring transformations, thermal analysis gives supplementary information regarding thermodynamics and kinetics as a function of temperature. The two main techniques in the study of pharmaceutical sciences include differential scanning calorimetry (DSC) and thermal gravimetric (TG) analysis. DSC measures the heat flow rate difference into a sample and reference material as the furnace goes through a controlled temperature program. Thermocouples determine the temperature of the furnace and a sensitive plate. If a phase change occurs, the heat is emitted or absorbed by the sample resulting in the modification of the heat flux through the heat sensitive plate. Knowing the heat capacity of the plate as a function of temperature, the enthalpy of the phase transformation can be calculated from the temperature change. This method was developed by Watson and O'Neill in 1962.[114,115] The method is used for the determination of thermodynamic events, such as crystallization, evaporation, glass transition, melting, or decomposition. The analytical method is used frequently to study the crystallization process and polymorphism.[116] The effect of thermal history and sample preparation on the polymorphic transformation profile from amorphous paracetamol were examined.[117] The velocity of the cooling process from liquid to the amorphous state and the encapsulation method determined the transformation scheme of the form III, II, and I.
The TG analysis, whereby mass changes are studied depending on the temperature, is helpful to interpret the DSC results. This method includes a highly precise analytical balance to which the pan with the sample is attached. The pan is surrounded by a heater controlling the temperature.[118] From the historical point of view, designs and construction of the first thermobalance can be traced back to 1903, where Nernst and Riesenfeld described the quantitative mass analysis with small sample amounts.[119] The TG analysis is ideal for determining kinetic processes involving mass changes. In this context, the study of the desolvation process of solvates is suitable. Joseph *et al.* demonstrated the potential of the TG analysis for kinetic studies by investigating the dehydration process of a hemisolvate of 4-hydroxynicotinic acid.[120] The robustness of this metastable hydrate regarding the dehydration stemmed from an increased activation

energy with the increase in particle size. An Avrami-Erofeev A2 model was assumed to describe the kinetic, which corresponds to a nucleation and growth mechanism.

2.2.4 Computational methods

The aim of the theoretical computations is to calculate the macroscopic phenomena from the microscopic interactions. Analytical and experimental possibilities are often limited due to technical reasons. Theoretical calculations and simulations coupled with the ever increasing speed of computers provide the chance to complement experimental information and predict crystallization processes and the outcome products. Developing reliable tools for understanding and prediction of polymorphism and crystallization has been a continuous effort. Besides the qualitative interaction studies to explain polymorphism, quantitative information are also required to predict progresses. It is necessary to understand the locality of intermolecular interactions, their influencing molecule components, and the consequent molecular packing motifs in the crystal.
Molecular dynamic and Monte-Carlo simulations are widely used methods to investigate structural and physical aspects of molecular systems. They serve as a complement to the conventional experiments, whose methods are limited in technical aspects. In the simulation, the molecular system can interact for a fixed period of time. This gives an idea of the dynamical evolution of the investigated system. The Molecular dynamic (MD) method solves the Newton's equations of motion for the molecular system, which results in trajectories for all components of the system. From these trajectories, a variety of properties can be determined. They can provide access to structural and energetic information of a system under specific temperature and pressure conditions, which is necessary to evaluate the stability of the phases. For example, by computing a spatial distribution function the organization of the molecules is available. This function is generated conventionally by averaging the entire simulated system and using long periods of simulation time. That also means that short-lived structural motifs during the MD simulation cannot be investigated. Recently, further software developments also concentrate on identifying and characterizing molecule clusters.[121] This procedure include distance criterion between atoms to establish the connectivity between molecules. The number of elements which form clusters, the cluster size distribution, the volumes of clusters, and the crystal packing motifs in solute clusters at the initial stages of nucleation process can be investigated.[121–124] The extraction of this information is valuable for studying the crystallization process and the resulting polymorphism. Furthermore, the crystallization from liquid solution is an important step in many production processes in industry and can be studied in more detail.

Theoretical predictions also bear limitations regarding the intricacy of the molecular system and the variety of influencing factors on the crystallization process. Although, theoretical computations make great progresses, the limits in the parameterization and the underlying molecular mechanics force fields to describe the real system restrict the capabilities. Therefore, experiments with sophisticated analytical techniques are still equally important as complementary methods. Nevertheless, the approximations and simplifications of the molecular model in MD simulations help us to understand and interpret the experimental results. Recent works emphasize the beneficial interplay of theoretical and experimental results, where a correlation between the molecular arrangement of dimers and trimers in solution, and the resulting molecular synthons in the crystallized material were confirmed.[125]

3 Methodologies and Materials

3.1 Materials

5-methyl-2-[(2-nitrophenyl)amino]-3-thiophenecarbonitrile, commonly known as ROY, is a highly polymorphic compound which is used as a precursor for the synthesis of the antipsychotic agent olanzapine.[126] Ten crystalline modifications are known and the structures of seven polymorphs were determined (see Table 3.1, p. 30).[127] The name ROY derives from the red, orange, and yellow color of the different polymorph crystals. The polymorphs R, Y, ON (orange needles), OP (orange plates), YN (yellow needles), and ORP (orthorhombic red-orange plates) could be obtained from liquid solution, whereas the RPL form developed from the vapor deposition on a single crystal.[128,129] The modifications Y04, YT04 (yellow plates), and R05 were observed during melting experiments, and the structure of YT04 was reported.[130,131] The structures of RPL, Y04, and R05 are unknown. Based on the structure analysis, the different conformers in the different crystal lattices of the polymorphs, who are significantly determined by the angle θ_{thio}, are identified to be responsible for the different crystal colors. θ_{thio} is the angle between the nitrophenyl fragment and the thiophene ring within a ROY molecule. As a consequence, the degree of $\pi-$conjugation between the *o*-nitroaniline chromophore and the thiophene group, and delocalization of the electrons change resulting in different color appearances. The crystallization experiments were performed with ROY ($\geq$ 98% purity) purchased from Intatrade Chemicals GmbH (Muldestausee, Germany). The purification of this material consisted of the dissolution in ethanol (Merck KGaA, Darmstadt, Germany) and the heating-up with active carbon. Filtration and recrystallization from ethanolic solution resulted in yellow crystals and small amounts of orange and red crystals. After separation from the supernatant solution, the crystals were manually sorted, and characterized by PXRD (Bruker AXS, D8, $CuK_{\alpha 1}$ radiation) and Raman spectroscopy. The yellow crystals were identified as the modification Y of ROY, whereas the orange and red crystals turned out to be the polymorphs ON and R, respectively. Liquid solutions of ROY were prepared from the sorted crystals in different organic solvents.

Table 3.1: This overview shows the studied organic model systems with the corresponding known polymorphs.

Compounds	Structure	Polymorphs/Solvates
5-methyl-2-[(2-nitrophenyl)amino]-3-thiophenecarbonitrile (ROY)	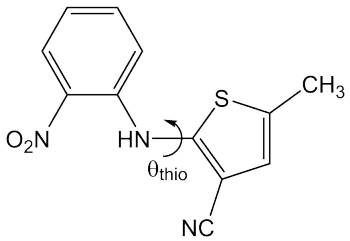	Y (yellow prism)[132] ON (orange needles)[132] R (red prism)[132] YN (yellow needles)[130] OP (orange plates)[130] ORP (orange-red prism)[130] YT04 (yellow prism)[130] Y04 (yellow)[130] RPL (red plates)[129] R05 (red)[130]
Paracetamol	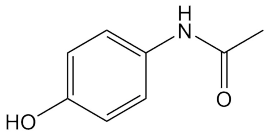	form I[133] form II[134] form III[135]
Indometacin	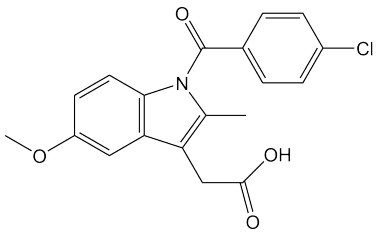	α/form II[136] β[137] γ/form I[138] δ[137] ϵ[139] ζ[139] η[139]

Paracetamol (PCM) is a mild analgesic to treat pain and fever. This API has already been discovered in 1878 by Morse.[140] In 1948, the analgesic became famous when the exceptionally good properties were discovered. Now, it belongs to one of the most essential drugs. The paracetamol molecule includes an acetamido group, one of the most important functional groups in pharmaceuticals which is capable to imitate the functional components in biopolymers. The intermolecular hydrogen bonds and the dynamics of the methyl group within the paracetamol molecule are responsible for the formation of different crystal structures. Three crystalline forms are known, but only the structures of the thermodynamically stable monoclinic form I and the metastable orthorhombic form II are well characterized. The commercially available form I is powdery with a poor compression affinity leading to a costly production process of tablets. The layer structure of form II allows a facilitated press procedure without additives. Haisa was the first researcher who succeeded in producing and determining the structure of form II from an ethanolic

solution in 1974.[134] At that time, the isolation was difficult because of the instability and the fast conversion from form II to form I. Even the seeding with form-II-crystals in a saturated solution resulted in a solvent-mediated transformation of the metastable form to the stable form within 15 minutes.[141] Finally, the isolation and stabilization of single crystals could be managed by the addition of polymeric heterogeneous seeds in aqueous solution.[142] The third crystalline modification was first mentioned by BURGER 1982;[143] PETERSON *et al.* could record a X-ray pattern and examine the structure features, but they failed to index the structure due to the low data quality.[144] Recently, PERRIN *et al.* succeeded in determining the structure of this metastable form by performing heating cycles under inert conditions.[135]
Paracetamol ($\geq$ 99% purity, Sigma-Aldrich) was used directly without further purification. Based on the PXRD (Bruker AXS, D8 Discover, $CuK_{\alpha 1}$ radiation) and Raman spectroscopy the crystal structure was determined as the thermodynamically stable monoclinic form I (Cambridge Structural Database entry HXACAN27). Liquid solutions of paracetamol in different organic solvents with concentrations of half the corresponding saturation were generated at 22.0 $\pm$ 1.0 °C. Concentration-dependent studies of paracetamol were performed in 1-propanol and methanol by preparing different concentrations referring to the saturation S (S = 0.1, 0.5, 0.8, 1.0).

Indometacin (IMC) is a nonsteroidal anti-inflammatory drug exhibiting a considerable tendency to form polymorphs and solvates. This drug was discovered in 1963.[145] Shortly after, the Food and Drug Administration released its intake as medication. To date, seven different polymorphic modifications, out of which just two crystalline structures (α or II, γ or I) were determined.[137,139,146] A wide range of solvates with acetone, benzene, dichlormethane,[147] tetrahydrofurane, propanol, chloroform, dimethylether, methanol, *t*-butanol, diethyloxide, carbon tetrachloride, cyclohexanone, ethanol, isoamyl alcohol, octan-2-ol, cyclohexanyl, and diethylether could be isolated.[137,148,149] In general, crystallization of these solvates leads to small crystals which are not suitable for single X-ray diffraction analysis, only the indometacin-*t*-butanol[150] and indometacin-methanol[151] solvates have been structurally characterized.
Indometacin ($\geq$ 99% purity, Sigma-Aldrich) was used without further purification. PXRD (Bruker AXS, D8 Discover, $CuK_{\alpha 1}$ radiation) and Raman spectroscopy identified the crystalline phases as the form I (or form γ) of indometacin. This result is in good accordance with the Cambridge Structural Database entry INDMET. The preparation of indometacin solvates was performed with different organic solvents, which were not

treated additionally. The solvate syntheses were conducted in 5 ml screw neck glass vials with plastic caps. The following amounts of solute and solvent were used: 0.206 g of indometacin and 1.5 ml of acetone for the IMC-acetone solvate ($C_{19}H_{16}O_4NCl \cdot 0.5\ (CH_3)_2CO$); 0.156 g of indometacin and 3 ml of chloroform for the IMC-chloroform solvate ($C_{19}H_{16}O_4NCl \cdot 0.5\ CHCl_3$); 0.104 g of indometacin and 4 ml of methanol for the IMC-methanol solvate ($C_{19}H_{16}O_4NCl \cdot CH_3OH$); 0.279 g of indometacin and 4 ml of 1-propanol for the IMC-1-propanol solvate ($C_{19}H_{16}O_4NCl \cdot 0.5\ C_4H_8O_2$); 0.510 g of indometacin and 2.5 ml of 1,4-dioxane for the IMC-1,4-dioxane solvate ($C_{19}H_{16}O_4NCl \cdot 0.5\ C_3H_8O$); and 0.578 g of indometacin and 2.5 ml of tetrahydrofuran for the IMC-tetrahydrofuran solvate ($C_{19}H_{16}O_4NCl \cdot 0.5\ C_4H_8O$). The suspensions with indometacin and the corresponding organic solvents were heated to 60 °C on a hotplate until the solid was completely dissolved. After storing the solutions in a fridge at 7 °C for at least 12 hours, cotton-wool-like suspensions consisting of tiny needles appeared. The prepared solvates were stable when being in contact with the solvent at 25 °C.

Acetone ($\geq$ 99.5%) was purchased from Th. Geyer GmbH & Co. KG (Renningen, Germany), acetonitrile ($\geq$ 99.8%) from J. T. Baker (Deventer, Netherlands), benzonitrile (99%) from Acros Organics (Geel, Belgium), dichloromethane ($\geq$ 99.5%) and methanol ($\geq$ 99.9%) from Carl Roth GmbH + Co. KG (Karlsruhe, Germany), ethyl acetate ($\geq$ 99.5%) from Fluka Chemie GmbH (Buchs, Switzerland), and 1-propanol ($\geq$ 99.5%) from Merck KGaA (Darmstadt, Germany). A Millipore system (conductivity $\leq$ 0.1 μS) produced the distilled and deionized water.

3.2 *In situ* analyses: Synchrotron X-ray scattering and Raman spectroscopy

The *in situ* XRD crystallization experiments of ROY, paracetamol (PCM), and indometacin (IMC) were performed at different beamlines and synchrotron facilities, each one had its specific features and advantages for the practical implementation of the designed experiments. Most of these experiments were conducted at the μSpot beamline (BESSY II, Helmholtz Centre Berlin for Materials and Energy) to capture the progress of crystallization with the main focus on the crystalline states (see Figure 3.1, p. 34). ACCEL instruments GmbH designed and installed this beamline permitting access to an adjustable beam size down to 10 μm and an energy range of 4-30 keV. A double crystal monochromator Si (111) was used to select the wavelength. In a typical experiment, a wavelength of 1.0 $\AA$ and an energy of approx. 12.4 keV were applied. The beam diameter had a size of 100 μm at a photon flux of 1 x 10^9 s^{-1} and a ring current of 298 mA with a resulting divergence of <1 mrad. Scattered intensities were collected with a 2D X-ray detector (MarMosaic, CCD 3072 x 3072) and a time resolution of 15 s.[152]
Additional measurements were performed at the Australian Synchrotron and the Paul Scherrer Institute (PSI) allowing the acquisition of a more highly angle- and time-resolved XRD data for the structure solution of occurring crystal forms. The Powder Diffraction Beamline[153] (Australian Synchrotron, Melbourne, Australia) and the MS-X04SA[154] (PSI, Villigen, Switzerland) beamline worked with similar settings: a Si (111) double-crystal monochromator selecting a wavelength of 1.0 $\AA$ with an energy of 12.4 keV. In both cases, a rotating capillary was setup with temperature control. The higher provided energy flux, and the advanced detector (Mythen 1D microstrip) enabled the implementation of highly efficient measurements regarding the angle and time resolution, especially, when it came to the radiation sensitive materials, such as organic compounds. The PXRD patterns were recorded with a time resolution of 50-180 s.
The total scattering experiments for the PDF analysis were recorded at the beamline ID11 at the ESRF with a tuneable X-ray beam from a few millimetre (mm) to 100 nm. For the total scattering studies with PCM a wavelength of 0.158154 $\AA$, and a beam size of 300 x 300 μm with a photon flux of 1 x 10^7 s^{-1} were used. A Frelon charge-coupled device (CCD) detector (47.2 x 47.2 pixels) located 85.8 mm behind the sample and captured the scattered signals with a time resolution of 1 s and 10 s for the PDF method.
Synchrotron 2D patterns from the μSpot and ID11 beamlines were converted into the equivalent 1D profiles (intensity versus scattering vector q) by employing an algorithm of

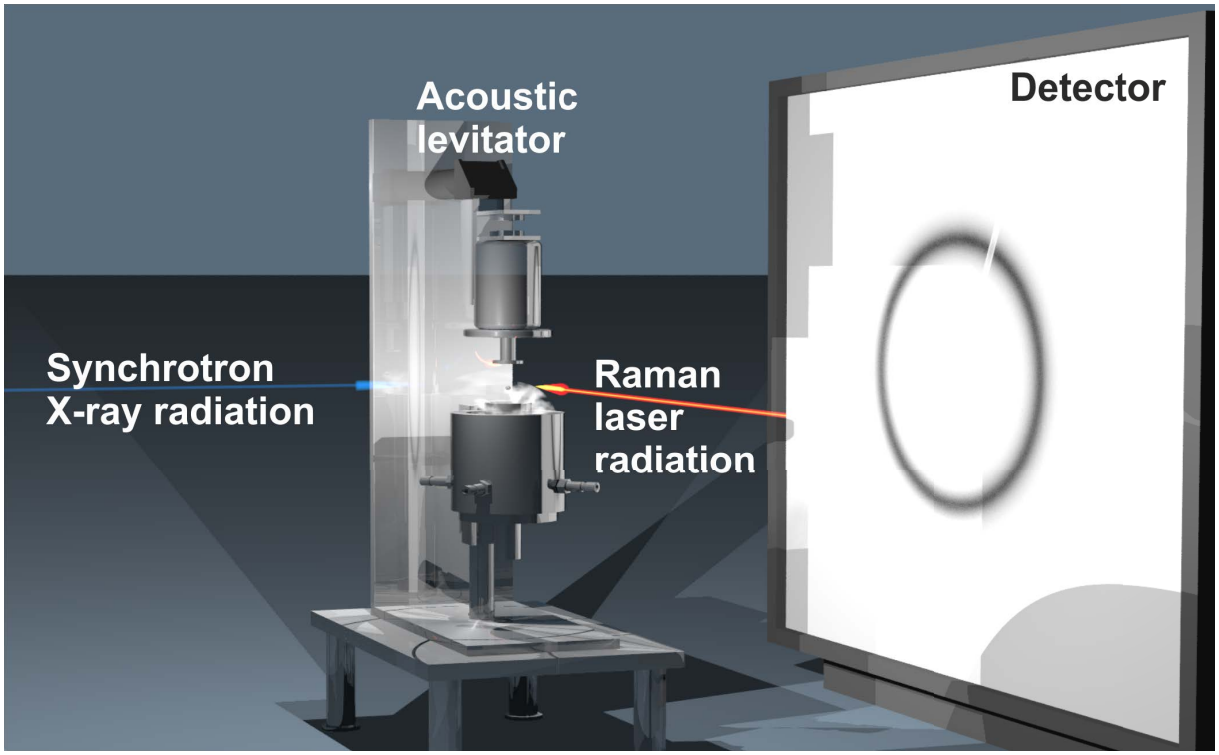

Figure 3.1: The setup of the crystallization studies with the acoustic levitator, and combined *in situ* synchrotron X-ray scattering experiments and Raman spectroscopy.

the computer program FIT2D.[155] PDF analyses based on the experimental total scattering data were generated using PDFgetX3.[156] The PDF data of the crystallization were analyzed qualitatively by comparing the probability distribution of the atom distances during the process.
The Raman spectroscopy, which relies on inelastic Raman scattering of monochromatic near-infrared (NIR) light, was suitable to study liquid solutions and amorphous phases. The sample composition and structural properties could be determined by analyzing fingerprint areas of the Raman spectra. The Raman measurements were performed with a Raman RXN1^{TM} Analyzer (Kaiser Optical Systems, Inc., Ecully, France) using NIR excitation at 785 nm, an irradiance of 6.6 W/cm^2 on the sample, and a CCD camera (1024 x 256 pixels). A non-contact probe head with a spot size of 1 mm diameter and a working distance of 1.5 cm was used for the experiments. An acquisition time of 5 x 5 s or 8 x 1 s was chosen resulting in a time resolution of 30 s or 15 s, respectively.

The combination of the two complementary analytical methods, synchrotron X-ray scattering and Raman spectroscopy, was a high-output approach to study the crystallization

from liquid solution. The acquisition of the XRD patterns and Raman data simultaneously within approx. 20 s period at the μSpot beamline permitted the determination of the phase composition from the onset of the first molecular assemblies in liquid solution and amorphous phases to the final crystalline structure.

3.3 Structure solution from PXRD

Powder X-ray diffraction (PXRD) patterns of the crystalline solids were recorded at the synchrotron (Powder Diffraction, Australian Synchrotron, Melbourne, Australia; MS-X04SA, PSI, Villigen, Switzerland). They were used for structure determination. The indexing was done with DASH 3.3.5[157] which includes the DICVOL[158] program. This helps to find the suitable cell parameters and the right space group. The subsequent structure solution is based on the Monte Carlo and simulated annealing process, respectively. When extracting the right structure, the structure refinement procedure was realized with TOPAS 5.[159–161] The process implements a Pawley refinement for the background, zero point errors, cell parameters, peak width, and the peak asymmetry. The Rietveld refinement adjusts the positions of the atoms, profile parameters, the background, and the isotropic temperature factor for non-hydrogen atoms.

3.4 Gravimetric analysis

Thermogravimetry studies to determine the stoichiometries and decomposition patterns of the indometacin solvates were carried out in a Perkin Elmer TGA7 apparatus using helium (Air Liquide N55) at a flow rate of 22.5 cm^3/min as the sample purge gas. The balance chamber was kept under a nitrogen flow (Air Liquide N45) of 38.0 cm^3/min. The mass scale of the instrument was calibrated with a standard 100 mg weight and the temperature calibration based on the measurement of the Curie points (T_c) of alumel alloy (Perkin-Elmer, T_c = 154.35 °C) and nickel (Perkin-Elmer, mass fraction 0.9999, T_c = 355.45 °C) standard reference materials. The solvates of indometacin were studied with this device. They were removed from the mother liquor, dried with a filter paper, and approx. 3-10 mg of the solvate was placed in an open platinum crucible. The heating experiment consisted of an isothermal step at 25.0 °C for 5-10 minutes, followed by the heating to 150 °C at a rate of 5 °C/min, and finally another isothermal step at 150 °C for 10 minutes. Five independent runs were carried out for each solvate.

3.5 Differential scanning calorimetry

Differential scanning calorimetry (DSC) experiments on indometacin solvates were performed in a Perkin Elmer DSC 7 apparatus. The samples were sealed under air in aluminum crucibles with punctured lids and weighed to 0.1 μg by using a Mettler UMT2 ultra-micro balance. Indium (Perkin Elmer; mass fraction 0.99999; T_{fus} = 156.75 °C, $\Delta_{fus}h^0$ = 28.45 J/g) was the calibration compound for the temperature and heat flow scales of the apparatus. The DSC studies were carried out in the temperature range of 10-180 °C and under a nitrogen flow (Air Liquide N45) of 25 cm^3/min. Starting at 25 °C the temperature was decreased to 10 °C at 5 °C/min and hold isothermally at this temperature for 3 minutes. Subsequently, the sample was heated up to 180 °C with a rate of 5 °C/min.

3.6 Crystallization under acoustic levitation

The crystallization studies from liquid solution were performed with a droplet volume of 5-7 μl and a corresponding diameter of maximal 2.3 mm. Unless otherwise stated, the humidity RH (RH = 17.5 ± 2.5 %) and temperature T (T = 22.0 ± 1.0 °C) maintained constant during all crystallization experiments. In a typical droplet experiment, the solution was injected with an Eppendorf pipette into the middle wave of the levitator. The droplet was held in a fixed position throughout the whole crystallization experiment. First, the volatile solvents evaporated over the entire droplet surface, which led to an increased concentration of the droplet until the crystallization occurred. The crystallization behavior of the analyte solutions was investigated in the acoustic levitator with simultaneous *in situ* synchrotron X-ray scattering and Raman spectroscopy at the μSpot (BESSY II, Helmholtz Centre Berlin for Materials and Energy). The volume of the shrinking droplet was monitored throughout the experiments based on recording pictures of the droplet. By using a reference object with known size, the volume and concentration of the droplet were available. Total scattering experiments with analyte solutions for PDF analyses of arising amorphous phases during the crystallization process were recorded at the ID11 beamline (ESRF, Grenoble).

3.7 Molecular dynamic simulation

The Molecular dynamic (MD) simulations of paracetamol in 1-propanol and in methanol were performed with the DL-POLY 4.08 package[162] and the initial input file prepared with PACKMOL[163] and DLPGEN[164]. The OPLS-AA force field,[165,166] whose parametrization is suitable for the accurate capture of the structural and energetic characteristics for organic polymorphic structures, was chosen for the calculations.[164,165] The first ratio of the components corresponds to the solubility of paracetamol at 30 °C (303 K) in the two solvents.[167] The mole fractions are $x_{PCM} \approx 0.07$ (246 paracetamol molecules and 3121 methanol molecules) in methanol and $x_{PCM} \approx 0.05$ (110 paracetamol molecules and 2080 1-propanol molecules) in 1-propanol. The supersaturated level was studied with $x_{PCM} \approx 0.09$ (246 paracetamol and 2484 methanol molecules; 154 paracetamol and 1555 1-propanol molecules) for both solvents.

The MD simulation calculates the connectivity between the molecules by comparing the distance between selected atoms and a defined threshold, the so-called cutoff. This information is used to identify the clusters which are previously defined, and appear in the simulation box. At the starting point of the simulations, the paracetamol and solvent molecules are far apart from each other in expanded simulation boxes. Subsequently, the boxes are equilibrated until a constant density is reached at a temperature of 30 °C and a pressure of 1 bar. To realize the maintenance of the temperature and pressure a Nosé-Hoover thermostat and barostat with relaxation time constants of 1 ps and 4 ps were used. The operations of 10 ns runs with a time step of 2 fs, and the atomic coordinates were recorded each 0.1 ps. The cutoff distance for the coulomb and van-der-Waals interactions is 1.5 nm. To consider the electrostatic interactions beyond this limit, the Ewald summation technique was applied.

The statistical analysis was performed from the MD simulation results and the spatial distribution functions (SDFs) were computed. The SDF determines the three-dimensional (3D) density distribution of finding a particle at a certain distance from one another. This allows a thorough view of the reference molecule and its surrounding atoms by computing the isosurface.

4 Results

The validation of literature shows the sensitivity of crystallization pathways, especially, the ones of organic compound to their different polymorphs. Therefore, the crystallization experiments in these studies are performed under controlled surface, temperature, and humidity conditions. The simultaneous acquisition of *in situ* X-ray scattering experiments and Raman data within 15-30 s period permits the determination of phase composition from the onset of the first molecular assemblies to the final crystalline structure. This coupled methods provide an unambiguous identification of the different phases. The conditions are defined by using the custom-made acoustic levitator and a nitrogen gas stream. The crystallization of ROY, paracetamol, and indometacin were monitored using different solvents. In a typical experiment, a droplet of the solution with the size of 5-7 μL are transferred in the levitator. The solvent evaporates, the concentration of the analyte increases resulting in a supersaturated droplet which crystallizes.
Additionally, the crystallization process in the levitator is investigated with further analytical and theoretical methods to gain supporting structural and kinetic information about the underlying processes.

4.1 Different crystallization pathways of ROY

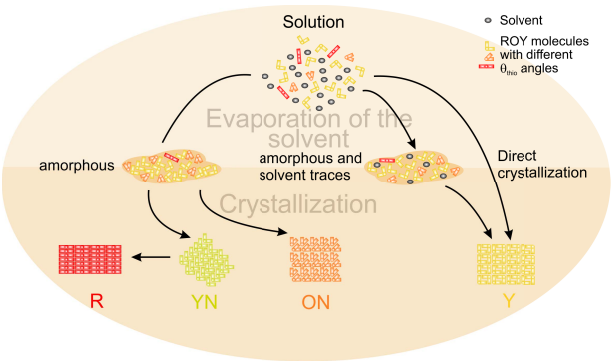

T. Gnutzmann, Y. Nguyen Thi, K. Rademann, and F. Emmerling. *Crystal Growth & Design*, 14:6445-6450, 2014.

Main aspects:

- The polymorphs of ROY crystallize from liquid solution via different pathways which are studied with the Raman spectroscopy and synchrotron XRD experiments.
- The crystallization process requires the control of influencing surfaces.
- One possibility to direct the crystallization process is the use of the acoustic levitator to realize a surface-free crystallization environment.
- The selective isolation of the polymorph Y, YN, ON, and R can be controlled by the proper choice of the solvent for the crystallization process in the acoustic levitator.
- The crystallization of the four polymorphs proceeds via an increase of the concentration through the evaporation of the solvent which leads to the formation of an amorphous phase as an intermediate.
- The amorphous phase is a metastable phase which can persist up to several hours and introduces the formation of the crystalline forms.

The ROY polymorphs have different distinct structures visualized in characteristic XRD patterns and Raman spectra. The selective crystallization of the ten ROY polymorphs is still difficult to accomplish. The crystal isolation of one structure without seeding is especially challenging. According to the classical and non-classical crystallization theories the surface effect on crystallization process is always emphasized. To study the surface influence, crystallization experiments in conventional glass beakers and on glass slides were compared with the crystallized products in the solid-free surface sample holder, the acoustic levitator, in terms of levitated droplets. In all cases, the experiments started

Table 4.1: This overview presents the crystallized polymorphs of ROY from different solvents in the acoustic levitator.

Solvent	Concentration [mmol/L]	Polymorph
Acetone	270	YN→R
	135	ON, YN→R, Y
	68	YN→R, Y, ON
	53	Y
Acetonitrile	131	Y
	64	Y
Benzonitrile	77	YN→R
Dichloromethane	502	Y, ON
	251	Y, ON
	123	ON, Y
Ethyl acetate	185	ON
	94	Y, ON, YN, YN→R
	47	ON
Methanol	21	YN
	10	YN, ON
	7	YN
1-Propanol	22	Y
	11	ON, Y
	7	ON

from the completely dissolved material in solutions of various solvents (see Table 4.1, p. 41). The different chosen concentrations for the experiments were below the saturation concentration and depended on the solubility of ROY in the corresponding solvents. The crystallization products could be distinguished unambiguously, fast, and easily with the Raman spectroscopy and the XRD experiments.

From the levitator crystallization experiments, four polymorphs and an amorphous phase could be identified with the simultaneously recorded XRD patterns and Raman spectra. The captured diffractograms of the crystalline products were in good agreement with the calculated reflexes of the polymorphs Y (QAXMEH01), ON (QAXMEH), YN (QAXMEH04), and R (QAXMEH02) from the Cambridge Structural Database (CSD) (see Figure 4.1, left colored markers, p. 43), which enabled the precise assignment of the crystalline forms. They are presented with the corresponding Raman spectra in Figure 4.1. The different crystal structures and conformational arrangements also effect

distinct differences in Raman signals. A common differentiation is possible by analyzing the stretching vibration band of the nitrile group (C≡N). This functional group shows characteristic bands in the range of 2210-2240 cm^{-1}. As the stretching frequency of the aromatic nitrile group depends on the electronic structure of the aromatic system, it is strongly influenced by the species and alignment of adjacent molecule fragments. ROY polymorphs exhibit a nitrile stretching band shift due to the different torsion angle between the thiophene and the nitrophenyl ring. The changed position varies the degree of π-conjugation and, thus, the nitrile group frequency.[128] The C≡N vibration mode is at 2232 cm^{-1} for Y, 2223 cm^{-1} for ON, 2222 cm^{-1} for YN, and 2212 cm^{-1} for R. By means of the fingerprint area from 400 cm^{-1} to 1700 cm^{-1} a clear distinction is provided only by using the Raman spectroscopy. Form Y is the thermodynamically stable polymorph of the known forms, and YN is the least stable one regarding the free energy. The R form is the second least stable modification. ON is more stable than YN and R, and enantiotropically related to Y.
The X-ray amorphous phase of ROY also shows a characteristic Raman spectrum in the fingerprint range from 400 cm^{-1} to 1700 cm^{-1} with broadened vibration bands. An explanation for these kind of signals is the disorder of the molecules in the amorphous state leading to a higher divergence within the local surrounding of each vibration mode. The nitrile vibration mode is at 2227 cm^{-1} with a shoulder at 2216 cm^{-1}. These distinct differences compared to the crystalline forms facilitate the identification of the amorphous phase. In combination with the known Raman spectra of used solvents, it is possible to distinguish the different crystalline and amorphous phases as well as the contributions of solvents.

The comparison of the crystalline products clearly shows the main differences in the purity of the resultant material. On slides, mixtures of different polymorphs arise, whereas the crystallization in the acoustic levitator leads to the formation of pure form Y, YN, and ON. The form R always crystallized concomitantly with small amounts of polymorph YN.
The four polymorphs exhibit characteristic crystallization pathways. After putting a droplet of the solution in the levitator the volatile solvent evaporated with the result of a steadily rising droplet concentration until the solvent completely vanished. Consequently, an intermediate phase of ROY developed which formed the appropriate crystalline structure. The following crystallization descriptions concentrate on separated characteristic reflexes and vibration bands for the identification of each polymorphic form. A detailed

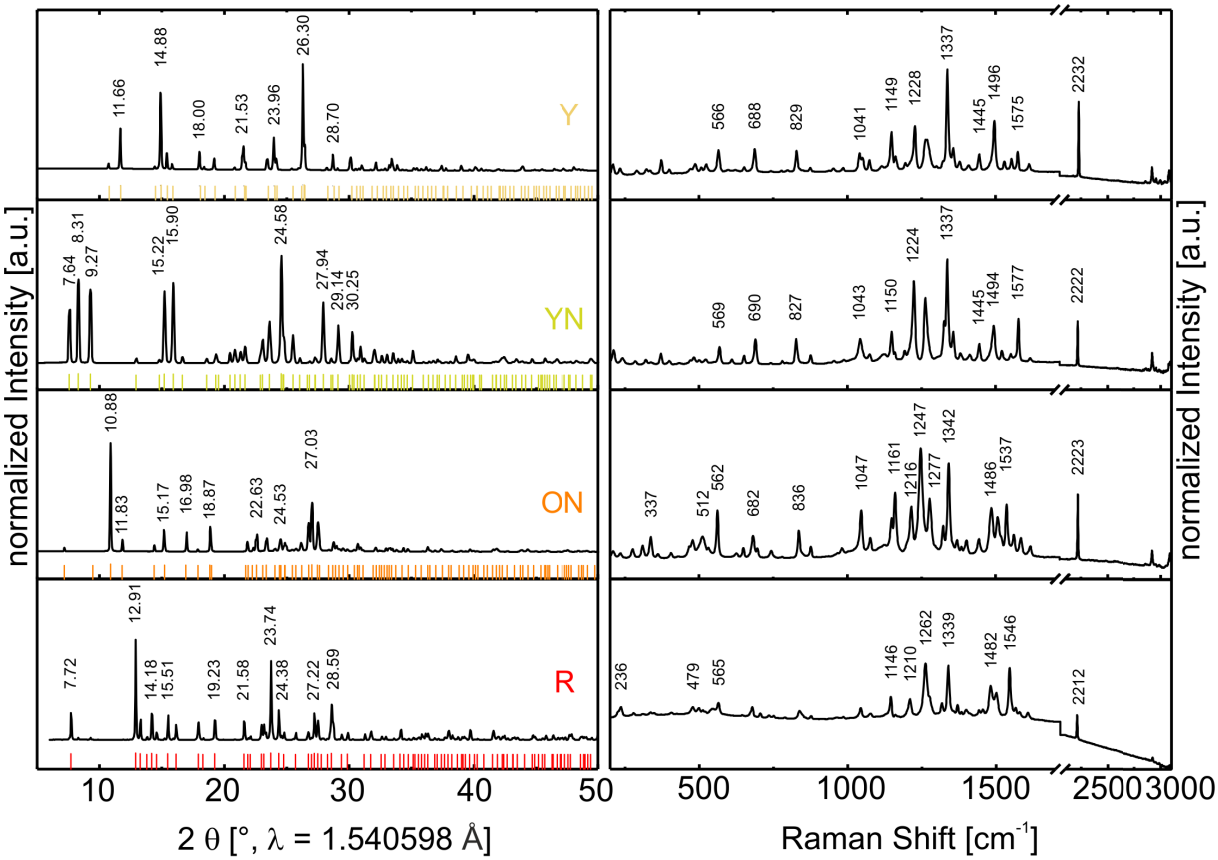

Figure 4.1: The XRD patterns (left) with the CSD entries as references marked with sticks and the corresponding Raman spectra (right) of the ROY polymorphs Y, YN, ON, and R obtained in the acoustic levitator are presented.

listing of scattering reflexes and vibration modes is given in the appendix (see Table 6.2, p. 108).

In the experiments acetone, ethyl acetate, and benzonitrile were able to form selectively the polymorph R. The simultaneously recorded wide-angle X-ray scattering (WAXS) and Raman data display the processes and intermediates involved during its formation process (see Figure 4.2, p. 45). At the beginning, the acetone solution showed only a broad scattering maximum at 21.3° 2θ (00.50 min) in the diffractogram. Within the next 6 minutes this maximum loses in intensity and shifts to 23.9° 2θ. Additionally, a second broad mount arises at 10.8° 2θ. First reflexes appear after 06.10 min, and they can be assigned to the pure metastable polymorph YN (06.25 min). The corresponding scattering pattern is shown as magnification on the left side with the calculated one from the single crystal data depicted in yellow bars in Figure 4.2. 15 seconds further, additional reflexes develop to the YN signals, which are contributions of the form R (see Figure 4.2, middle magnification, left side, p. 45). In the following, the relative intensity of the R reflexes increases in comparison to the YN reflexes until no further changes are detectable. The crystallization is completed after 07.35 min, where mainly signals of R can be identified with the calculated diffraction pattern from the single crystal data presented in red bars. It is worthwhile noting that still weak reflexes of YN at 8.3° 2θ and 9.27° 2θ are evident in the final crystallization product indicating a mixture of polymorphs with R as the main component. The corresponding Raman spectra of the crystallization on the right side of Figure 4.2 complement information about occurring intermediates. Initially, the Raman spectrum of the liquid solution exhibited two intense Raman bands at 2924 cm^{-1} and 788 cm^{-1}, which can be determined as the characteristic C-H and C-C stretching vibrations of acetone (00.10 min). The intensities of these modes correlate directly with the quantity of acetone in the droplet. Within the following 02.25 min the acetone signals decreases in intensity until they disappear. This presents the complete evaporation of the volatile solvent. At the same time, the Raman spectrum evolves characteristic vibration modes of the amorphous form with the broadened C≡N signal at 2227 cm^{-1}. Its magnification confirms the formation of pure amorphous ROY without any acetone residues. The metastable form remains stable for several minutes and crystallizes to the pure YN form after 06.00 min. This fact is obvious due to the isolated appearance of the YN Raman vibration bands without signals from the amorphous phase or other crystalline forms. At this point, the Raman spectroscopy reinforces not only the WAXS result, but also shows its greater sensitivity to the transformation. Shortly after, the Raman device detects new

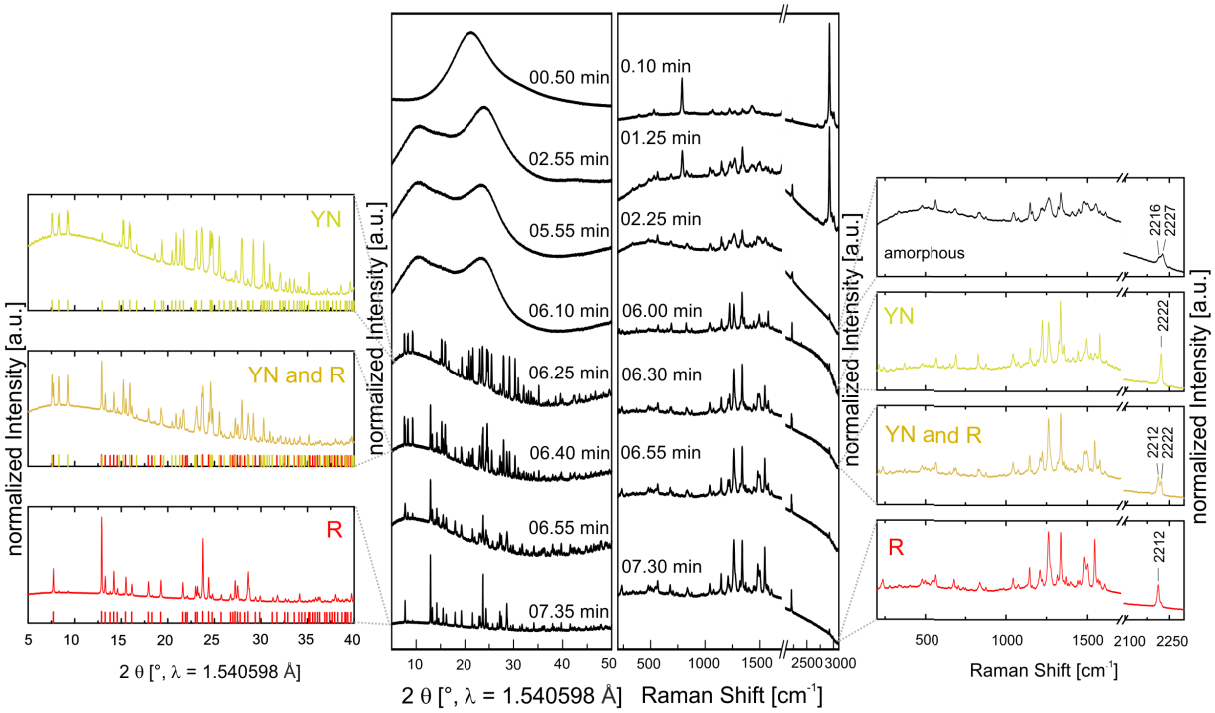

Figure 4.2: From acetone the polymorph R crystallizes in the acoustic levitator via the amorphous phase and the crystalline YN form. The crystallization product consists of a mixture of the R and YN form, whereas the R dominates.

bands of the modification R with the associated C≡N band at 2212 cm^{-1}. The continuous measurements show the increased intensity of this band, whereas the 2222 cm^{-1} signal of YN diminishes. The careful examination of the last Raman spectra (07.30 min) still shows small amounts of the YN polymorph in the form of a small shoulder at the 2212 cm^{-1} C≡N band. Those results are in good agreement with the mixed polymorphic product of the scattering data.

The crystallization of R always follows the described characteristic succession independent on the solvent. The evaporation of the solvent causes a rising solute concentration and induces the formation of a pure amorphous phase, which is stable for several minutes. This process is dependent on the properties of the used solvent. Afterwards, the YN nucleates from the amorphous phase, followed by the crystallization of R through the entire sample. From that moment, specific scattering reflexes and Raman bands of both polymorphs are detectable with R as the dominating form. The described crystallization sequence is in line with the Ostwald's rule of stages due to YN is the least stable and R the second stable crystalline form of ROY regarding their free energies.[128,130] The polymorphic mixture is an indication for a cross-nucleation. In that regard, the initially nucleated form

does not convert to another crystalline form, rather a second polymorph with a higher growth rate nucleates on the growing first one. Once R with its slightly higher growth rate in comparison to YN[131] nucleates, it is able to fill the whole material within the spherical sample. A solvent-mediated polymorphic conversion can be excluded because the Raman spectroscopy approves the absence of solvent residues during the formation of the crystalline modifications. In addition, the polymorph R has never been obtained without YN, so independent nucleation processes are unlikely.

The isolation of pure YN without the nucleation of R can be achieved by using methanol as the solvent. Comparable to the above described crystallization process the evaporation of methanol induces the formation of the amorphous phase in present of the remaining methanol. This process normally takes about 8 minutes (see Appendix, Figure 6.1, p. 109). The formed amorphous phase is stable for about 10 minutes and crystallizes within 3 minutes to the pure polymorph YN. This observation supports the fact that YN has a slower growth rate than R.
Transformation and nucleation of form R from the methanolic solution never appeared in the repeated experiments. Because of this characteristic crystallization pathway in methanol, it is assumed that the small methanol molecules are able to pre-orientate the ROY molecules during the evaporation process leading to a specific preferred arrangement in the amorphous phase. This arrangement might facilitate and stabilize the crystallization of form YN.
In the experiments, methanol is the strongest proton donor increasing the probability to protonate the nitrile group or the nitro group of the ROY molecules, which act as the proton acceptors. As a consequence, these functional groups lose their electron-supplying ability to the $\pi-$conjugation between the *o*-nitroaniline chromophore and the thiophene group. The $\pi-$conjugation changes are related directly to the degree of the θ_{thio} angle. This might be the reason behind finding ROY molecules with higher θ_{thio} values in liquid solution and the resultant amorphous phase.

The formation of form ON proceeds via comparable intermediate states. After the evaporation of the solvent, one more amorphous phase is provided. The difference in this case is the long-lasting lifetime of the pure amorphous phase up to several hours in the majority of the crystallization trials (see Appendix, Figure 6.3, p. 111). It is independent on the solvent. During that term the Raman signals of the amorphous phase become more pronounced and the corresponding amorphous X-ray scattering maximum slightly shifts

to higher 2θ values. These changes indicate a rearrangement of the amorphous phase. The spontaneously start of the ON nucleation is followed by a fast crystallization process through the whole sample within a minute. During the observation time, no further transformations to a more stable polymorph are detected. ON is a kinetically stable form which can be stored for several months.

The frequently obtained form is the stable polymorph Y, that arises via two possible pathways: i) During the evaporation of the solvent Y nuclei have already occurred in the present of solvent amounts. This is demonstrated by the appearance of characteristic solvent signals and vibration bands of Y at the same time. The signal intensity of the solvent decreases and finally disappears with further time until only signals of Y remain. This process without passing through less stable intermediates does not correspond to the Ostwald's rule of stages. The reason might be the too small differences in the free energies of the polymorphs. ii) The second process also exhibits an amorphous phase as an intermediate (see Appendix, Figure 6.2, p. 110). With the continuing volatilization of the solvent the amorphous state develops so that the nucleation of Y starts from this metastable phase with solvent residues. Subsequently, the solvent amounts vanish completely leaving the pure crystalline material of Y. The crystallization process from the amorphous state to the crystalline form is finished within less than a minute. It is obvious that both pathways leading to form Y show a crystallization process with the common property of having solvent portions at the beginning. The duration of one entire crystallization experiment strongly depends on the boiling point and the vapor pressure of the used solvents.

The pathways of the performed crystallization experiments with ROY from various organic solvents are summarized in the illustration 4.3. Each polymorph has its characteristic crystallization sequence with specific intermediate stages. YN, ON, and R always include an amorphous phase as an intermediate prior to the formation of the crystalline form, however, only YN and ON nucleate from the pure amorphous phase. The forms YN, ON, and Y always crystallize as a pure material. On the other hand, the form R needs the present of YN crystallites to nucleate and grow resulting to a mixture of both polymorphs. The results of the crystallization experiments from different solvents and in different concentrations are summarized in the Table 4.1. The repeated experiments show a remarkable reproducibility and purity of the polymorphs. Literature presented results often reported about the poor selectivity of the crystallization from liquid solution

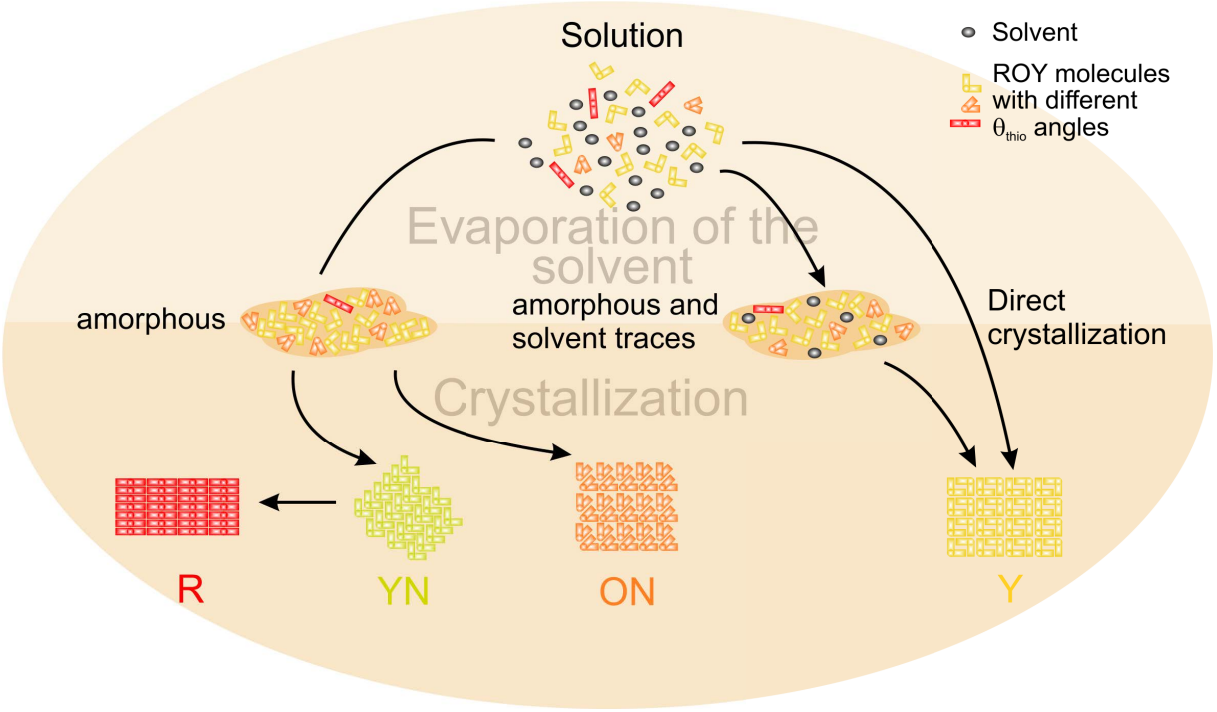

Figure 4.3: The graphical summary displays the different crystallization pathways of the ROY polymorphs from different solvents. Depending on the specific crystalline form, amorphous phase, or liquid solution the ROY molecules adopt different θ_{thio} values. θ_{thio} is the angle between the nitrophenyl fragment and the thiophene ring within a ROY molecule.

in conventional sample holder. For example the crystallization from a methanolic solution yielded the form R, ON, OP, ORP, YN, or Y.[128] However, in our studies YN is obtained with greatest probability from methanol. Looking at the results, it is also evident that the thermodynamically stable form Y is often observed. This form is favored in presence of solvent amounts. Some of the solvents are also able to crystallize different modifications from one and the same solution, but even then only one phase is obtained.

4.2 Selective crystallization of the paracetamol polymorphs

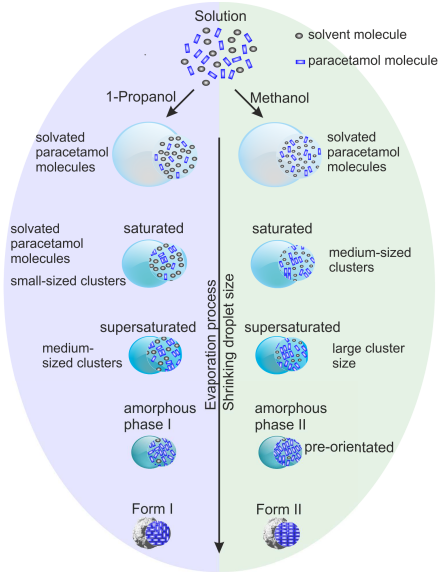

Y. Nguyen Thi, K. Rademann, and F. Emmerling. *CrystEngComm*, 17:8967-9244, 2015.

T. Y. Nguyen, E. A. Roessler, K. Rademann, and F. Emmerling. *Zeitschrift für Kristallographie - Crystalline Materials*, 232:15-24, 2017.

Main aspects:

- The crystallization of paracetamol from liquid solution are studied with *in situ* synchrotron XRD experiments and Raman spectroscopy, PDF analysis of total X-ray scattering experiments, and molecular dynamic simulations.
- The research focusses on the influence of the solvent and the concentration on the crystallization pathway and the resulting crystalline forms.
- Two solvent groups are identified where one group prefers to form polymorph I and the other one the polymorph II of paracetamol.
- The crystallization process proceeds depending on the solvent via different saturation stages where the solutions exhibit different cluster sizes.
- The formation of the pure polymorphs passes through amorphous phases which are assumed to have different local molecule arrangements. The phenomenon of polyamorphism is suggested for paracetamol.
- The amorphous phases are imprinted precursors of the resulting crystalline forms.
- In the specific case of methanol as the solvent, the initial concentration also guides the outcome of the crystalline structure.

Table 4.2: The crystallization of paracetamol from different solvents with half the corresponding saturation as the initial concentration[167] leads to two groups of solvents. The one group of solvents crystallizes preferentially the form I and the other one very likely provides form II.

Solvents	Crystallized polymorph
acetic acid, acetone, acetonitrile, chloroform, ethanol, 1,4-dioxane, 1-propanol, 2-propanol, tetrahydrofuran	form I
2-butanone, ethyl acetate, methanol, water	form II, (form I)

The crystallization studies with paracetamol can be divided in three different sections: the *in situ* synchrotron X-ray scattering and Raman spectroscopy studies of the different liquid solutions, the PDF analysis of the total X-ray scattering patterns received from different crystallization pathways, and the dependence of crystallization pathways from the initial concentration.

4.2.1 *In situ* X-ray diffraction and Raman spectroscopy studies

The crystallization started from liquid solutions in different solvents. In all solvents, the half the saturation concentration was used as the initial concentration. Table 4.2 lists the crystallization products obtained from each solvent in the acoustic levitator. In the repeated experiments with combined synchrotron XRD and Raman spectroscopy, two groups of solvents become evident. The first group forms preferentially the thermodynamically stable polymorph I, however, the second group including for instance methanol prefers to form the orthorhombic polymorph II. Though, the crystallization of monoclinic form I cannot be completely ruled out.
The thorough analysis of the X-ray scattering patterns and Raman data of the crystallization products always shows the formation of pure crystalline modifications. The XRD data and Raman spectra have exclusively characteristic signals of one of the two polymorphs (see Figure 4.4, p. 51). A mixture of both polymorphs was never obtained.
Exemplarily, crystallization processes, one for each solvent group, are presented in Figure 4.5. In these examples, form I arises from 1-propanol and form II from methanol. During the first minute the liquid solutions appear as amorphous scattering halos in the XRD patterns. The corresponding Raman spectra exhibit the characteristic vibration signals of the methyl rocking and C-C stretching at 859 cm^{-1} for 1-propanol. This solvent has the symmetric and asymmetric methyl stretching vibration at 2878 cm^{-1} and

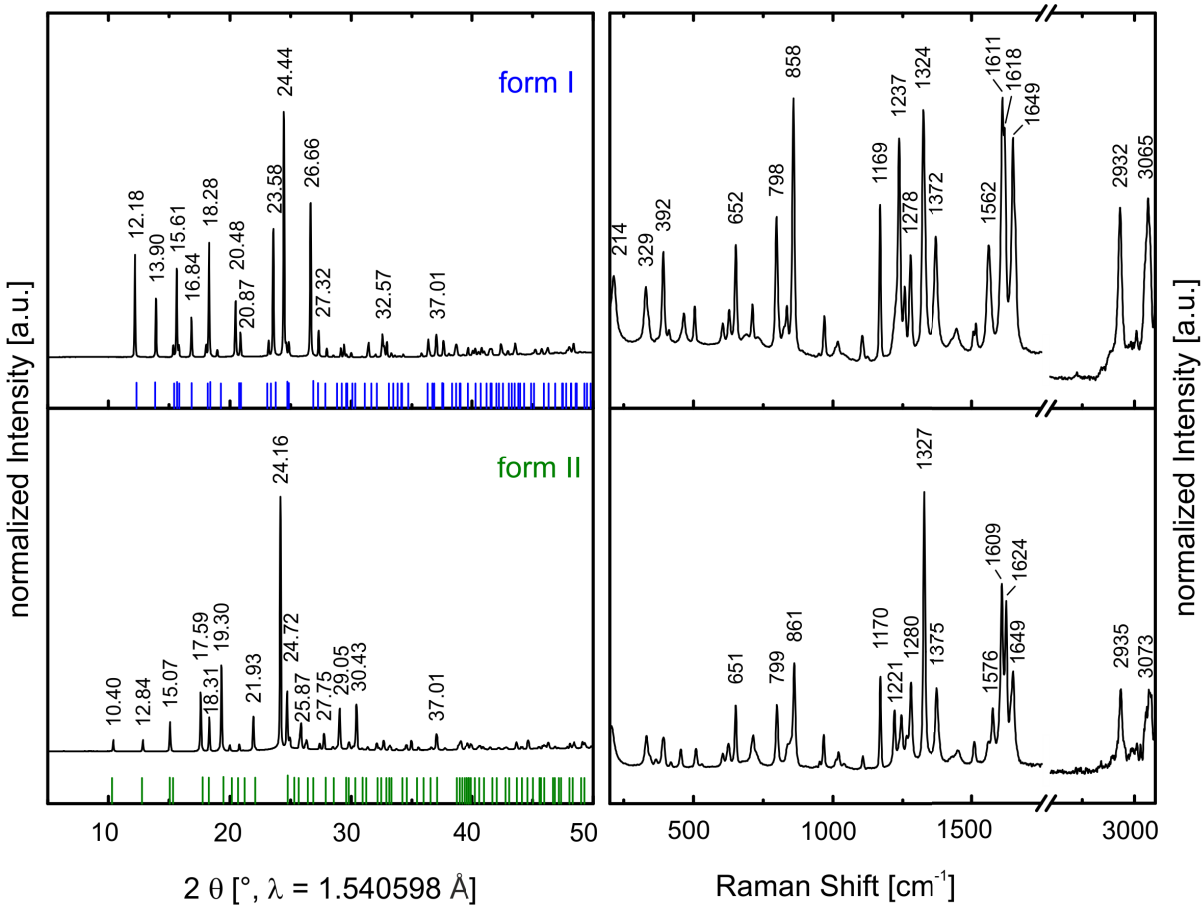

Figure 4.4: The X-ray diffraction patterns and the Raman spectra of the thermodynamically stable form I and metastable form II of paracetamol under ambient conditions are shown. The XRDs of the both polymorphs are in good agreement with the calculated patterns of the database entries HXACAN27 (blue markers) and HXACAN31 (green markers). The analytics display exclusively signals of one form suggesting the purity of the crystallization products.

2964 cm^{-1}, whereas the equivalent vibrations can be found at 2835 cm^{-1} and 2941 cm^{-1} for methanol.[168] With increased reaction time, the intensity of the above mentioned signals decreases describing the evaporation of the solvents. At the same time, the specific bands of the amorphous paracetamol phase at 1236 cm^{-1}, 1280 cm^{-1}, 1326 cm^{-1}, 1376 cm^{-1}, and 1618 cm^{-1} are detected in both cases (see Figure 4.5, 10.00 min and 18.30 min, p. 53).[169] Up to the respective point in time, the XRDs show shifts of the scattering maxima, but no reflexes occur. First reflexes appear with the onset of the crystallization (see Figure 4.5, 10.20 min and 18.40 min, p. 53), and they gain in intensity with the progressive crystallization process. The onset of the crystallization is also visible on the changes of the vibration bands in position, intensity, and narrow band widths in the Raman spectra.

The two crystallization pathways have many common steps: the evaporation of the solvent proceeds and introduces the formation of a pure amorphous phase; the corresponding crystalline forms crystallize from this metastable phase. When looking carefully at the XRD patterns of the amorphous phases arising during the crystallization of form I and II (10.05 min and 18.25 min), a shift of around 1° in 2θ of the scattering maxima emerges (see Figure 4.5, enlargement left, p. 53). The simultaneously recorded Raman spectra of these states exhibit the same broad vibration bands in the range of 200 cm^{-1} to 1700 cm^{-1} (see Figure 4.5, enlargement right, p. 53). This fact can be explained by the distribution of bond lengths and bond angles within the disordered amorphous phases. In the range of 2800 cm^{-1} to 3100 cm^{-1}, where the symmetric and asymmetric vibration signals of the methyl group and the C−H stretching vibrations of the phenyl ring appear, differences in vibration positions and relative intensities can be indicated. In both cases, the characteristic symmetric methyl stretch vibration of 1-propanol and methanol, respectively, with lower intensity are detectable. This is an indication of smallest solvent residues next to the amorphous phases. These residues evaporate completely with the start of the transformation to the crystalline form. The marginal differences expressed in the XRDs and Raman spectra indicate the occurrence of two different amorphous phases with different local structures.

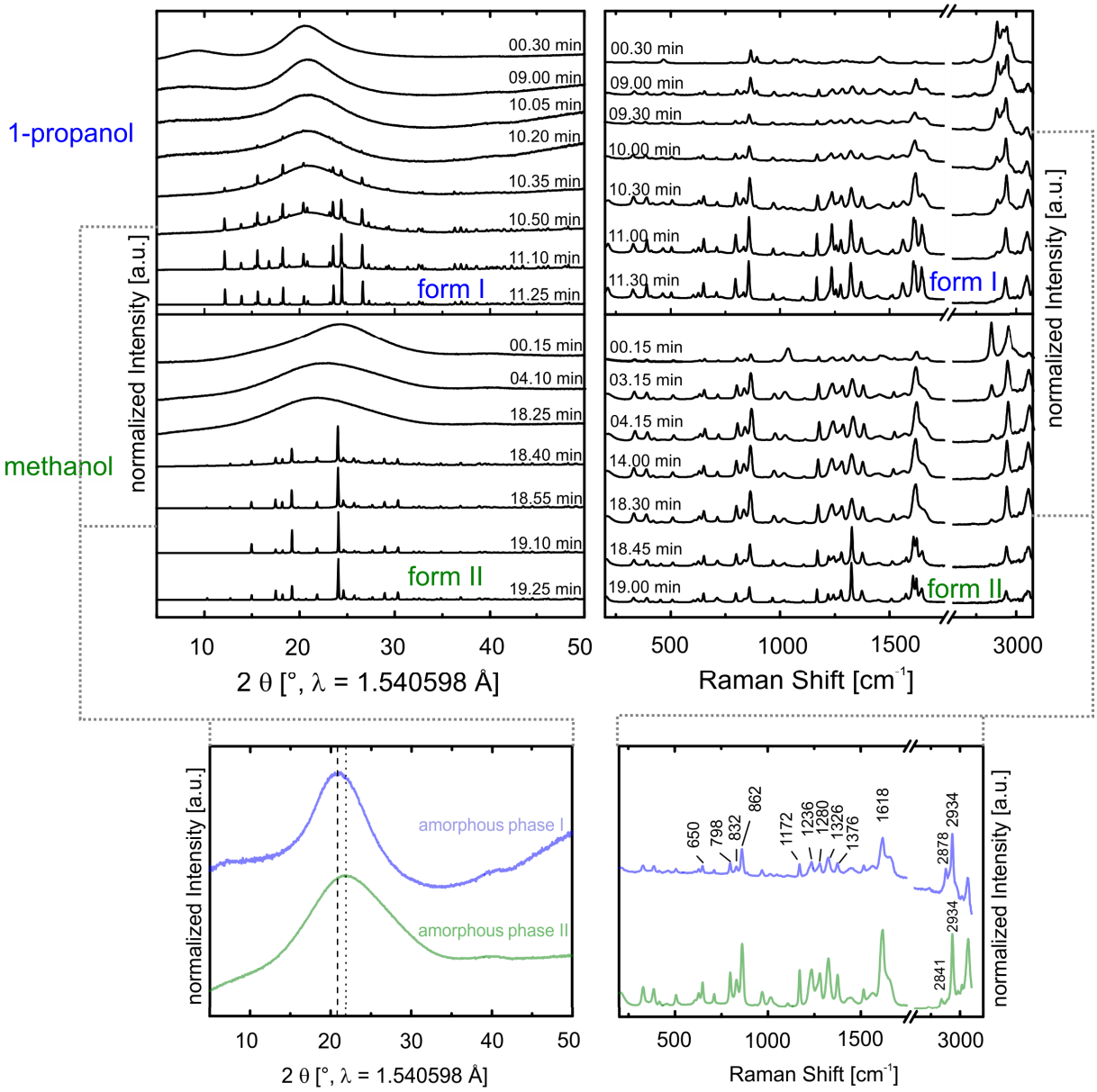

Figure 4.5: The crystallization processes of the form I from 1-propanol and form II from methanol proceed via amorphous phases. The metastable phases crystallize either to form I or form II. The enlargements present the XRDs and Raman spectra of these amorphous phases. The slightly shift of the scattering amounts in the XRDs (dashed markers) and the differences in Raman bands at higher wavenumbers from 2800 cm^{-1} to 3200 cm^{-1} indicate the occurrence of two different amorphous phases.

4.2.2 Total X-ray scattering and PDF analyses

To study these amorphous phases, the PDF analysis, displaying the probability to find two atoms at a certain distance r, is capable to extract structural information of non-crystalline materials from total scattering experiments. The application is widely used for inorganic compounds, but by now only few studies with PDF analysis focus on investigating crystalline and amorphous organic compounds.[102,170] The rapid acquisition of total scattering experiments with subsequent PDF analysis is suitable to investigate time-resolved above-described amorphous intermediates. The crystallization of paracetamol from 1-propanol and methanol were repeated under the same conditions. The total X-ray scattering patterns and the corresponding transformed PDFs of these crystallization processes are presented in Figure 4.6. By means of the X-ray scattering patterns, amorphous and crystalline phases can be distinguished, and the start of the crystallization becomes visible by the appearance of Bragg reflexes.
The solution of paracetamol in 1-propanol has its scattering maximum at q = 14.46 nm^{-1} (20.42° 2θ, Cu_α), the maximum of the methanolic solution is shifted to higher values at q = 16.88 nm^{-1} (23.89° 2θ, Cu_α). With the gradual evaporation of the solvents and the formation of the amorphous phases the scattering maxima approach each other. Shortly before the crystallization starts, the maxima of the two amorphous phases are shifted in a range of 0.64 nm^{-1} (0.82° 2θ, Cu_α). This is in good agreement with the previous XRD experiments. The total X-ray scattering patterns were transformed to G(r) functions by using data up to q_{max} = 170 nm^{-1}. The generated PDFs are divided into three different parts including the intramolecular, the intra- and intermolecular, and only the intermolecular range (see Figure 4.6, p. 55). The distances within a paracetamol molecule are defined as $i \leq 8$ $\AA$, whereas $j \geq 2.5$ $\AA$ describes the atom-atom distance between different paracetamol molecules. The overlapping area marked grey in Figure 4.6 is the interesting interval for the evaluation. The PDFs of liquid solutions and amorphous phases lack in significant intermediate range order. In these cases, the PDFs can be considered as a PDF of a single molecule. During the evaporation process of the solvent the intramolecular distances within the paracetamol molecule remain unaffected. Therefore, the focus of the analysis is the intersection of intra- and intermolecular distances where changes in the PDF can be traced to changes in intermolecular distances and interactions. The structure of the paracetamol polymorphs is determined by hydrogen bonds between the functional groups: the hydroxyl and the oxygen atom of the carbonyl group. These interactions lead to the formation of molecule chains, which are interlinked by further hydrogen bonds between the N−H unit and the hydroxyl group. The results are folded

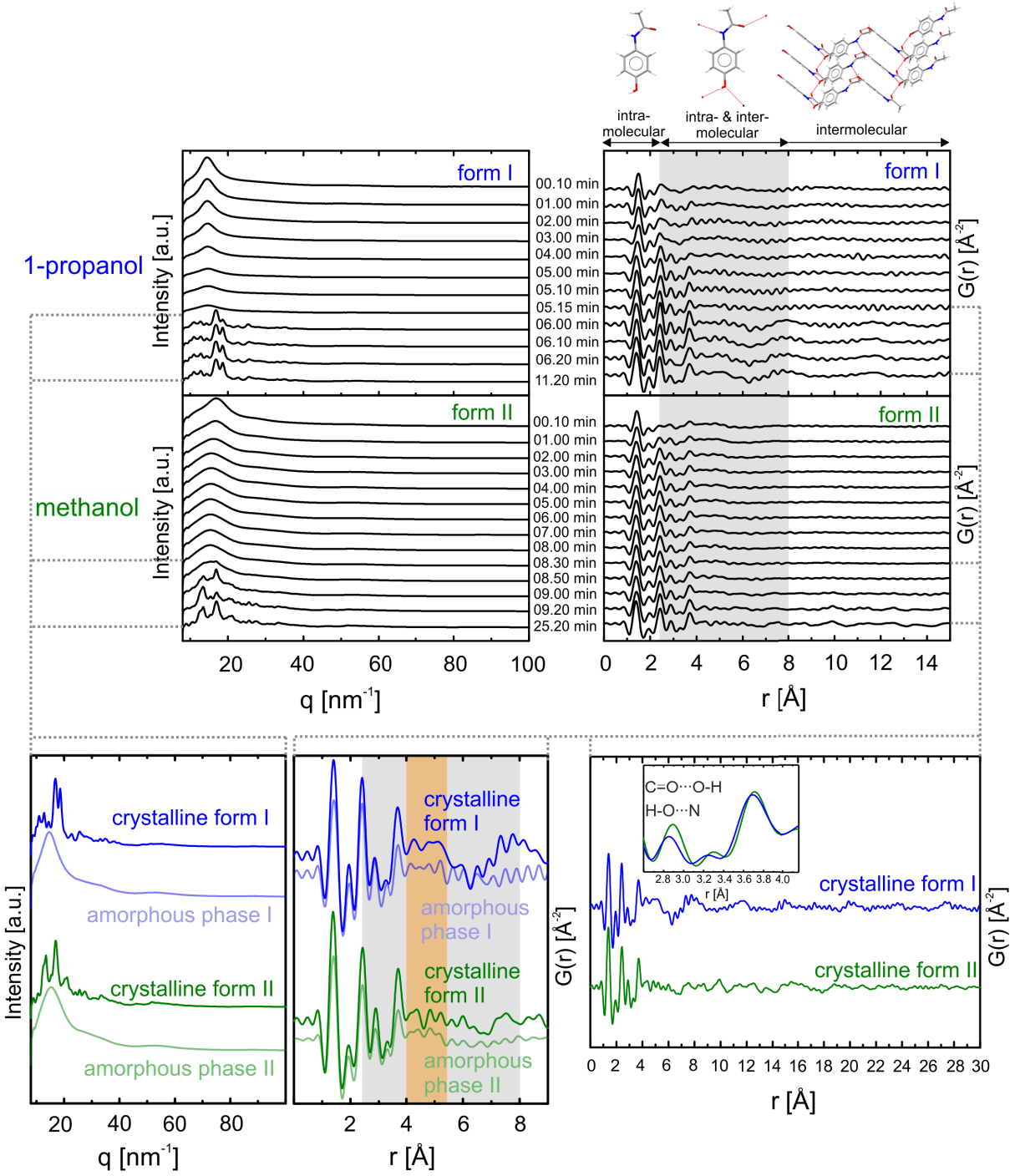

Figure 4.6: The crystallization process of form I from 1-propanol and form II from methanol are analyzed time-resolved by high energy synchrotron X-ray to gain high q-range data (top left). The corresponding PDFs of the processes are generated (top right). The enlargement (bottom right) compares the PDFs of the crystalline forms with some structural characteristics in the inset. The figure in the lower left part shows selected total X-ray scattering patterns and the corresponding PDFs of the amorphous phases shortly before crystallization starts compared with the PDFs of the resultant crystalline forms.

Table 4.3: The characteristics D···A (D = hydrogen donor, A = hydrogen acceptor) hydrogen bond distances between neighboring molecules in the crystalline structure of form I (data base entry HXACAN27) and form II (data base entry HXACAN31) of paracetamol are presented.

Intermolecular distances D···A	Form I [$\AA$]	Form II [$\AA$]
C=O···O−H	2.65	2.71
H−O···N	2.90	2.93
C=O···C−OH	3.46	3.48
O=C···O−H	3.69	3.76
HO−C···N	3.73	4.00

layers in the crystal structure of form I and flat layers in form II. Careful analysis of the atom distances enables the assignment of the range from 2.65-2.93 $\AA$ in the PDFs as the C=O···O−H and H−O···N hydrogen bonds. They show pronounced peaks as well as the distance distribution of their adjacent atoms involved in these hydrogen bonds in the range of 3.46-4.0 $\AA$. The PDFs of the crystalline products (see Figure 4.6, bottom right, inset, p. 55) have two distinct distance peaks in the above-mentioned ranges. The inset displays a slight shift of these peaks to smaller atom-atom distances in the PDF of the crystalline form I (blue) compared to the PDF of the form II (green). This fact reflects the shorter and stronger intermolecular hydrogen bond interactions in the polymorphic structure of form I (see Table 4.3, p. 56). The results are consistent with the diffraction and spectroscopic investigations of the paracetamol at low and high temperatures. They confirm the higher stability of form I by demonstrating the larger strength of the individual hydrogen bonds between the hydroxyl and the acetamido group in form I.[171,172] Both polymorphic structures present longe-range order in the range $j \geq 8.0$ $\AA$ in the PDFs. It is evident that with increased atom-atom distance the peak intensities decrease and broaden which can be explained by the limited q-range used for the Fourier transformation and the low motion correlation in long distances.

At the beginning of the crystallization experiments, only atom distance distributions up to about 8 $\AA$ are apparent in the PDFs. This effect was expected due to liquid solutions and amorphous stages lack in long-range order and the extensive network between the paracetamol molecules. This fact is supported by the low intensities of the two typical peaks representing the intermolecular hydrogen bonds in the range of 2.65-2.93 $\AA$ and 3.46-4.0 $\AA$. With progressive evaporation of the solvents the intensities of these peaks increase indicating the formation of first structurally defining hydrogen bonds (after 05.00 min in 1-propanol and 01.00 min in methanol). The analysis of the PDFs assigned

to the amorphous phases shortly before crystallization starts (05.15 min in 1-propanol and 08.30 min) shows a similar distance distribution compared to the corresponding resultant crystalline forms (see Figure 4.6, bottom right, marked orange, p. 55). One can assume that the metastable phase already contains the characteristic hydrogen bonds between the hydroxyl and the acetamido group determining the developing crystalline form. The mentioned characteristic distance peaks in the PDFs also exhibit the shift to lower distance values during the crystallization of form I. The pronounced hydrogen bonds between the functional groups can already be identified at this intermediate stage. Comparing the PDFs of the amorphous phases, major differences in peak positions and relative peak intensities arise in the region of 4.0-5.3 $\mathring{A}$. This is an indication of different molecule arrangement in the amorphous phases, therefore the two different amorphous states are called amorphous phase I and amorphous phase II.
To summarize the results from the PDF analysis the following aspects are highlighted: i) The PDFs of the amorphous phases and the resultant crystalline forms show similar features. Particularly, the overlapping region, where intra- and intermolecular atom distances occur, indicates imprinted hydrogen bonds in the amorphous phases of the subsequently crystallized form. ii) The two different amorphous phases assume to be crucial intermediate stages with local pre-ordered molecules during the crystallization process. They are proto-crystalline precursors. The imprinted structure motifs facilitate the crystallization of the corresponding crystalline structures. iii) The crystallization of paracetamol starting from half saturated solutions and under controlled temperature and humidity shows two different crystallization pathways with two different amorphous phases as intermediates.

4.2.3 Concentration experiments

The crystallization studies described before were only performed with half saturated concentrations in the corresponding solvents (S = 0.5). The results show that at that concentration 1-propanol forms form I and methanol favorably generates form II of paracetamol, but in very few exceptional cases form I can also occur. The question arises whether the concentration is an influencing factor guiding the crystallization pathway of paracetamol. Therefore, the next step concentrates on the crystallization experiments from 1-propanol and methanol starting at different initial concentrations of paracetamol in the corresponding solvent. They were performed under the same conditions as the previous runs. Analyzing the images of the droplet during the evaporation time of the solvent, the concentration of the droplet can be quantified as a function of time (see Figure 4.7, p. 58).
All concentration experiments with 1-propanol do not show a significant correlation be-

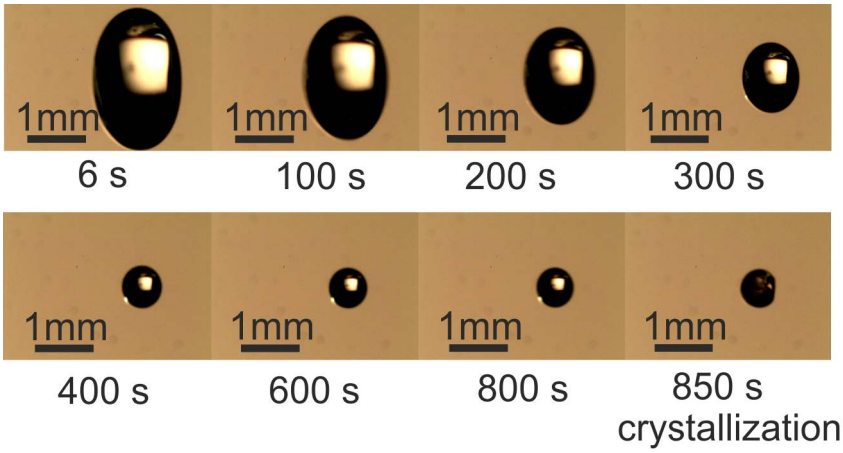

Figure 4.7: The size profile of the droplet during the crystallization process in the acoustic levitator is presented. The continuous decrease of the droplet's size (methanol solution) and the transformation from liquid to solid crystalline phase is shown in the picture series. The droplet shrinks in the diameter from 2 mm to 0.6 mm.

tween the initial concentration and the resulting polymorph of paracetamol. The concentration of the 1-propanol droplets beginning at S = 1.0 and S = 0.8 rises steadily (see Figure 4.8 A, p. 59). They reach a saturation of S = 5.5-7.0 within approx. 600 s, where the crystallization of form I always occurs through all the repetitions. At the crystallization onset, 1-propanol is still present. The concentration increase with S = 0.1 is low within the first 600 s. Then a sudden rise of S from 1.0 to 9.5 within the next 200 s is remarkable. In some cases, crystallization occurs before reaching a plateau of saturation. However, a crystallization progress via an amorphous phase is more likely. In Figure 4.8 B, an example is demonstrated where a saturation plateau at around 9.5 has been detected for 300 s followed by a step which raises the plateau to a saturation of about 11. This state corresponds to the amorphous form I. The step between the both plateaus can be explained by the evaporation of last trapped solvent residues. The crystallization in the levitator starts in most instances at the surface of the droplet leading to the formation of a shell with imbedded solvent amounts. The crystallization is finally introduced after 1500 s.

In methanol, crystallization processes beginning with concentrations near the saturation S (S = 1.0, 0.8) always produce the stable form I. The initial concentration progresses in both cases are very similar (see Figure 4.8 B, p. 59). Starting at S = 1.0 the crystallization occurs directly from solution within 200-250 s, however, the droplet with S = 0.8 increases its concentration quickly within the first 250 s and achieves a plateau at around S = 4.5. This state is amorphous with small amounts of solvent residue from which the crystalliza-

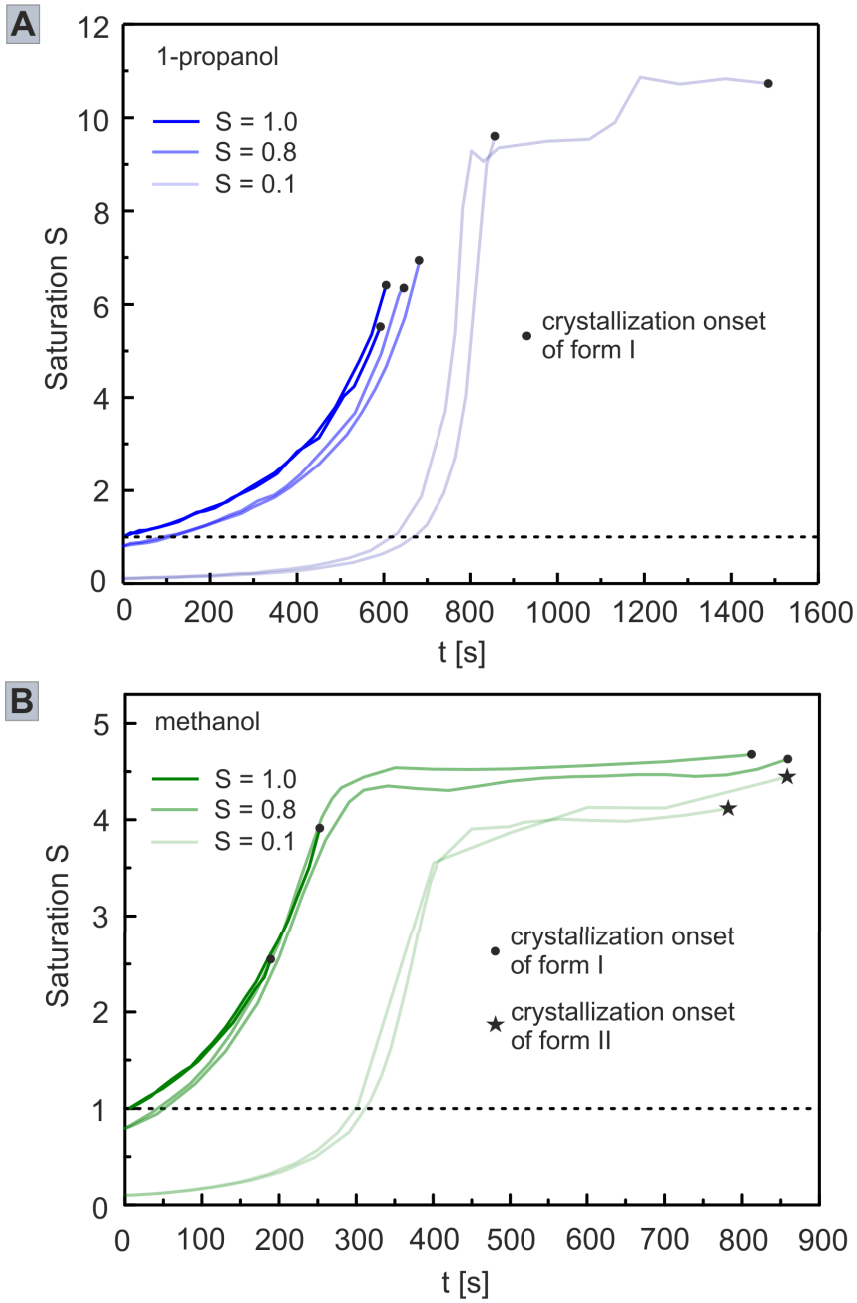

Figure 4.8: The concentration profile of the droplet during the crystallization of paracetamol in 1-propanol and methanol is shown. The corresponding saturation ratio ($S = c/c_s$) of the droplet is plotted as a function of time. Starting from the liquid solution and different initial concentrations (see color code) the crystallization process was studied with *in situ* XRD until the start of the crystallization could be detected. The black filled circles mark the crystallization onset of form I, whereas the black filled stars present the crystallization onset of form II. The two same colored lines for each concentration stem from repeated runs. A) The saturation concentration of paracetamol in 1-propanol is $c_s = 0.59$ mol/l. B) The saturation concentration of paracetamol in methanol is $c_s = 1.45$ mol/l.

tion of form I proceeds. Comparing the absolute concentration value of this plateau with the value of the amorphous phase I achieved during the 1-propanol run with S = 0.1, the concentration is around 6.5 mol/l in both solvents. The progress and the crystallization result of the diluted solutions (S = 0.1) differs from the previous ones. The increase of the concentration rises slowly and steadily within the first 300 s, followed by a fast step where S goes from 0.8 to almost 4.0 within 100 s. Another plateau between 4.0-4.5 is reached for further 400 s. This intermediate corresponds to the assumed amorphous phase II which always introduces the crystallization of metastable form II. The experiments show that for methanol the variation of the initial concentration can also affect the crystallization pathway and its outcome. The probability to generate form II increase with decreasing initial concentrations. The initial concentration and half the saturation represents a turning point. Form I could be formed, but form II arises most likely. Whether an amorphous phase is formed or not is determined by the number of solvent molecules. Liquid solutions with concentrations below the saturation S = 1.0 always form an amorphous phase.
The overall concentration experiments suggest that the initial concentrations have influence whether an amorphous phase is formed. In the specific case of methanol, it also has a directing effect on the crystallization pathway and the formation of the resulting polymorph.

4.2.4 Molecular dynamic simulations of paracetamol solutions

The next step to understand the crystallization process of paracetamol from liquid solution in more detail is to explain the mentioned experimental phenomena. Therefore, MD simulations of the two selected liquid solutions were chosen to study the interactions between the paracetamol and solvent molecules. The MD simulations of the paracetamol solutions at two different saturation levels were performed in cooperation with Dr. Carlos Bernardes from the University of Lisbon. The solutions in 1-propanol and methanol represent the solvent group producing preferably either form I or form II of paracetamol (see Table 4.2, p. 50).
In order to achieve an approximation to the crystallization conditions in the ultrasonic levitator, simulations of the solutions at saturated and supersaturated levels were performed. The MD simulations of the saturated level can be considered as one snapshot of the molecular motions in the droplet during the evaporation process when concentration increases. The supersaturated level is close to the corresponding amorphous phases which appear as intermediates. Considering the concentrations of paracetamol in methanol and 1-propanol as mole fractions, the saturation in both solvents are slightly different with

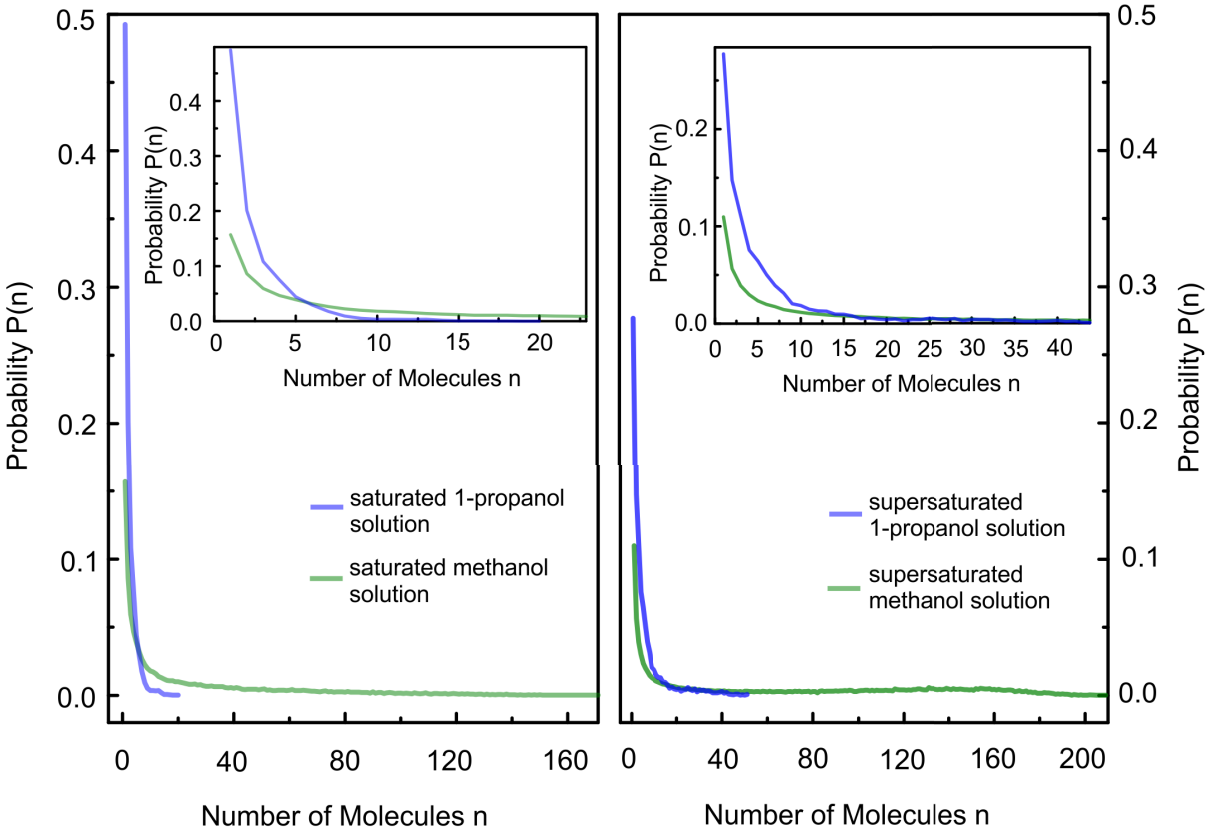

Figure 4.9: The size distribution of paracetamol clusters is evaluated from the MD simulations. The number of paracetamol molecules n and the corresponding probability $P(n)$ in 1-propanol and methanol at different saturation levels are compared.

mole fractions of $x_{PCM} \approx 0.07$ and $x_{PCM} \approx 0.05$, respectively. To investigate the early stages in these liquid solutions, the focus of the simulation analysis is the interactions of paracetamol-paracetamol and paracetamol-solvent molecules.

In the first step, the size distribution profile of the paracetamol molecules in liquid solutions are studied. The MD simulations of the saturated level emphasize the formation of smaller clusters in 1-propanol in comparison to methanol (see Figure 4.9 left, p. 61). Almost 50% of the paracetamol molecules are completely solvated in 1-propanol and over 40% of the molecules form clusters with 2 to 5 molecules. This results in low probability of forming large solute aggregates in 1-propanol; units up to 20 paracetamol molecules can be identified. In contrast, in methanol around 40% of the paracetamol molecules are completely solvated or form clusters with 2 to 5 molecules. More than 60% of the molecules are in arrangement of 6 up to 170 molecules in the clusters.

In supersaturated solutions, the molar fraction corresponds to $x_{PCM} \approx 0.09$. This reflects

a changed solution state with a lower number of solvent molecules shortly before crystallization starts. Here, the MD simulations indicate an increase of the average aggregates size in both liquid solutions. A shift of the probability distribution to bigger cluster sizes is generated. In 1-propanol, 32% of the molecules form clusters with 6 up to 50 molecules, and the methanolic solution enables the formation of sizes with 6 up to 200 molecules with more than 75% probability. This has a strong impact on the molecular arrangement in the solutions.
The careful analysis of the spatial distribution functions emphasizes this aspect. The interactions of the paracetamol molecules with the nitrogen and oxygen atoms of neighbors are much higher in methanol than in 1-propanol in the saturated and supersaturated level. This is especially evident in the case of the higher blue and pink isosurfaces of the nitrogen and oxygen atoms in the immediate vicinity (see Figure 4.10, p. 63). When comparing the isosurfaces of the 1-propanol solution in both concentration levels the interactions change marginally and the intermolecular organization of the paracetamol molecules remains almost the same (see Figure 4.10 C and D, p. 63). The main interaction consists of the hydrogen bonds with the hydroxyl group of the neighbors. On the other hand, a remarkable rise of intermolecular interactions between neighbored paracetamol molecules with the nitrogen atom and the hydroxyl group is evident in the methanol solution (see Figure 4.10 A and B, p. 63). The molecules are able to arrange themselves in a large variety and closer way. The diversity in spatial arrangement and the formation of multiple clusters increases the probability to form pre-arranged local areas. These results support the previous XRD experiments and the PDF analysis of the crystallization of paracetamol in 1-propanol and methanol where a pre-orientated amorphous phase could be detected as the reason for the formation of the metastable polymorph II.

The graphic 4.11 summarizes the two crystallization pathways of paracetamol which could be identified with the analytical and theoretical analyses. The scattering experiments with the X-ray and laser radiation, the concentration studies, and the simulations give a deep insight into the underlying processes. The observed appearances at the macro level can be explained with interactions at molecular level. Especially, the characteristics and the amount of the solvent are decisive parameters determining and guiding the crystallization pathways. These results support the selective isolation of one desired polymorph of paracetamol, and they give indications referring to the specific conditions.

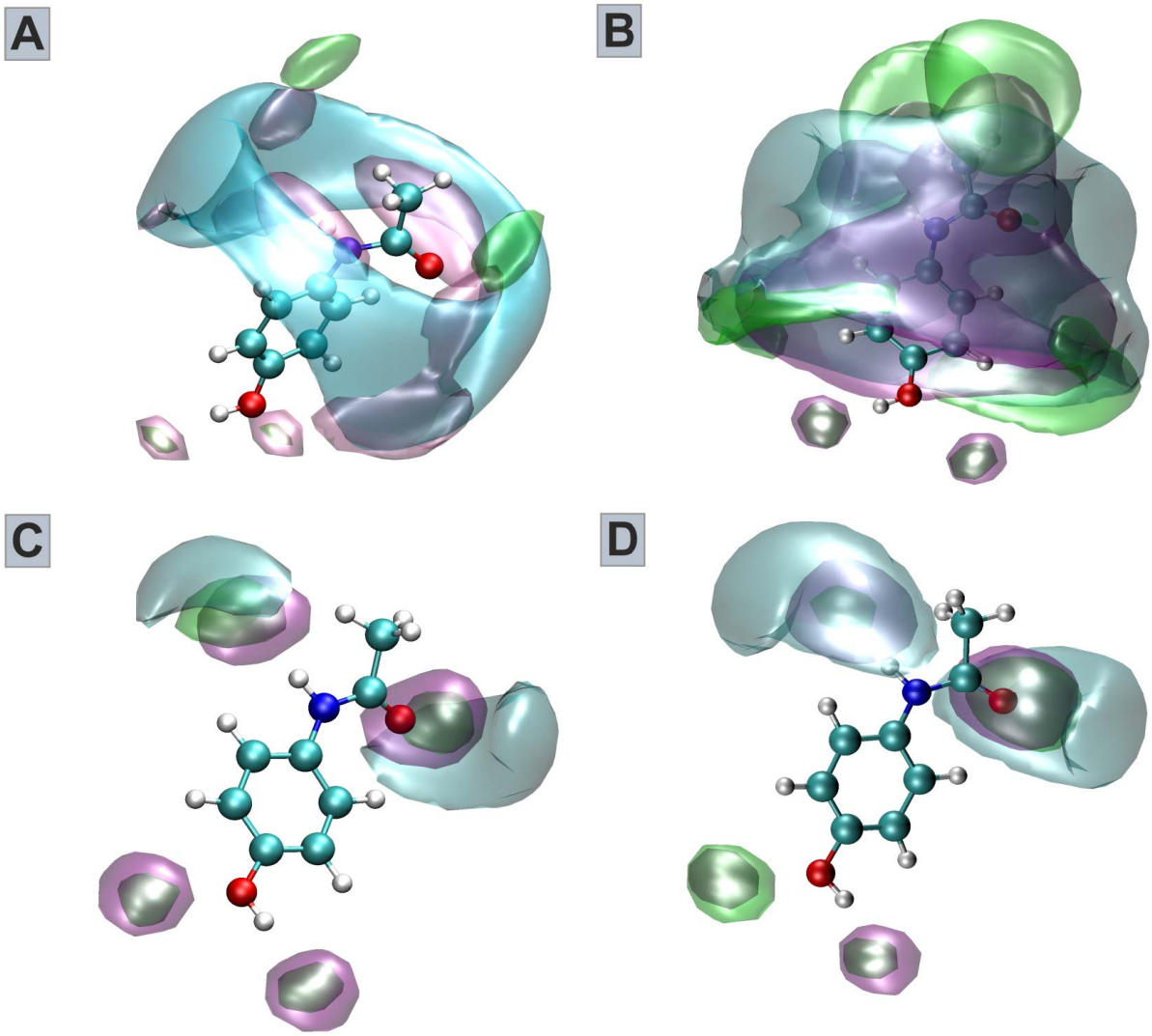

Figure 4.10: The images show the spatial distribution functions of the paracetamol in methanol (A, B) and 1-propanol (C, D). The colored isosurfaces correspond to the distribution of neighbored paracetamol molecules with their nitrogen atoms (blue), oxygen atoms of the hydroxyl group (pink), and oxygen atoms of the carbonyl group (green). A ($x_{PCM} \approx 0.07$) and C ($x_{PCM} \approx 0.05$) present the saturated solutions, whereas B and D show the results for the supersaturated solutions ($x_{PCM} \approx 0.09$) at 30 °C.

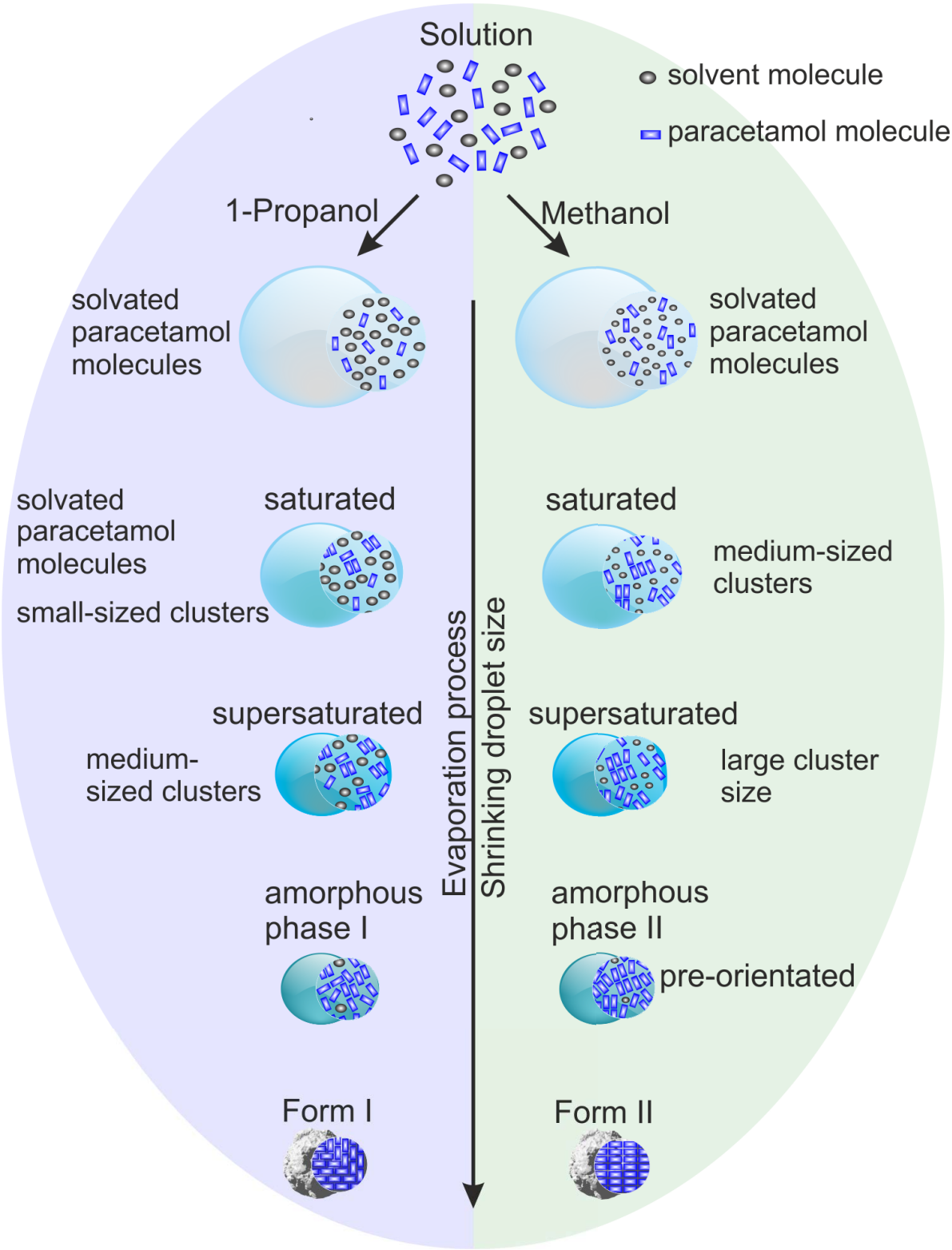

Figure 4.11: The graphical illustration summarizes the results for the crystallization process of paracetamol from 1-propanol and methanol. Depending on the solvent different cluster sizes and interactions to neighbored paracetamol molecules are formed resulting in two different amorphous phases. These intermediates are imprinted with structural motifs of the resultant crystalline forms.

4.3 Crystallization of indometacin

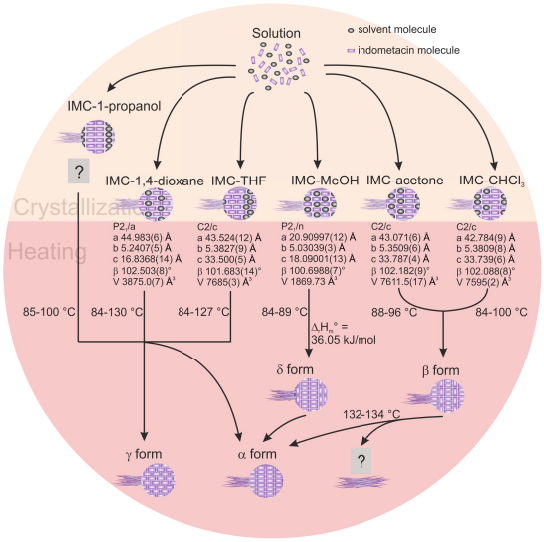

T. Y. Nguyen, C. Bernardes, M. E. Minas da Piedade, G. Matveeva, U. Kolb, K. Rademann, and F. Emmerling, in preparation.

Main aspects:

- The crystallization of indometacin from organic solvents are studied structurally and kinetically.
- Indometacin forms solvates with a variety of organic solvents.
- Most of the solvates are formed as a mixture of an amorphous phase and solvent amounts.
- The structures of the solvates with methanol, chloroform, acetone, tetrahydrofuran, and 1,4-dioxane are presented and discussed.
- The desolvation of the methanol solvate by heating proceeds via the metastable δ polymorph. This process has an enthalpy of $\Delta_r H_m^\circ = 36.25 \pm 1.04$ kJ/mol.
- The desolvation of the chloroform and acetone solvate by heating proceeds via the metastable β polymorph.

The previous studies of ROY and paracetamol focused exclusively on the investigation of structural aspects of the intermediates and the crystallization process with different methods. The following section deals with the structural and thermal analyses of indometacin from organic solutions. The structures of the solvates are strongly correlated with their stabilities which can be described with kinetic parameters.

4.3.1 Structural features

The crystallization studies of indometacin are performed similarly to the ones of ROY and paracetamol. As a result, solvates of indometacin with acetone, chloroform, 1-propanol, tetrahydrofuran (THF), 1,4-dioxane, and methanol were always formed starting from liquid solution. Only the solvents ethanol and acetonitril tended to introduce the polymorph α, or a mixture of α and γ. The XRD patterns and Raman spectra of the crystalline solvates are shown in Figure 4.12. Comparing the XRD patterns and Raman spectra of the solvates with acetone, chloroform, 1,4-dioxane, THF, and 1-propanol many similarities regarding the positions of the diffraction reflexes in the XRD patterns and vibration signals in the Raman spectra are visible. The distinction of the solvates among the Raman spectra is especially challenging. Due to the strong dependence of the Raman scattering on the structural environment of the material, the close resemblance indicates similar structural features of these solvates. Vibration signals in the range of 2750-3200 cm^{-1} assigned to the C−H stretching region of the solvents are helpful to identify the materials. The XRD patterns, on the other hand, have more significant differences implicating slight changes in the cell parameters of the different crystal structures. Only the methanol solvate differs from the rest of the solvates which is clearly demonstrated by the variation in the diffraction reflexes (see Figure 4.12, p. 67).

The crystallization pathway of all mentioned solvates is comparable. The example with 1,4-dioxane shows that initially the present of the solvent 1,4-dioxane is visible at the intensive vibration band at 835 cm^{-1}, 2856 cm^{-1}, and 2968 cm^{-1} in the Raman spectra which belong to the symmetric ring stretching vibration and the C−H stretching vibration, respectively (see Figure 6.7, p. 115).[173] 1,4-Dioxane evaporates gradually and, at the same time, the amorphous indometacin evolves. In accordance with these observations, the vibration intensities of the solvent decrease and the signals of the amorphous phase at 1683 cm^{-1}, 1591 cm^{-1}, and 738 cm^{-1} become more intense.[174] After around 5 minutes the mixture of the solvent and amorphous phase starts to crystallize to the solvate. This is indicated by the characteristic reflexes in the XRD patterns and the typical Raman signals. In the Raman spectrum of the solvate, the ring stretching vibration of 1,4-dioxane is still at 835 cm^{-1}, whereas the C−H stretching vibration in the crystalline phase shows a slight shift to 2851 cm^{-1} and 2972 cm^{-1}. This change is caused by the different molecular environment in the crystal structure, where the C−H bond is involved in other intermolecular interactions in comparison to the liquid solution.

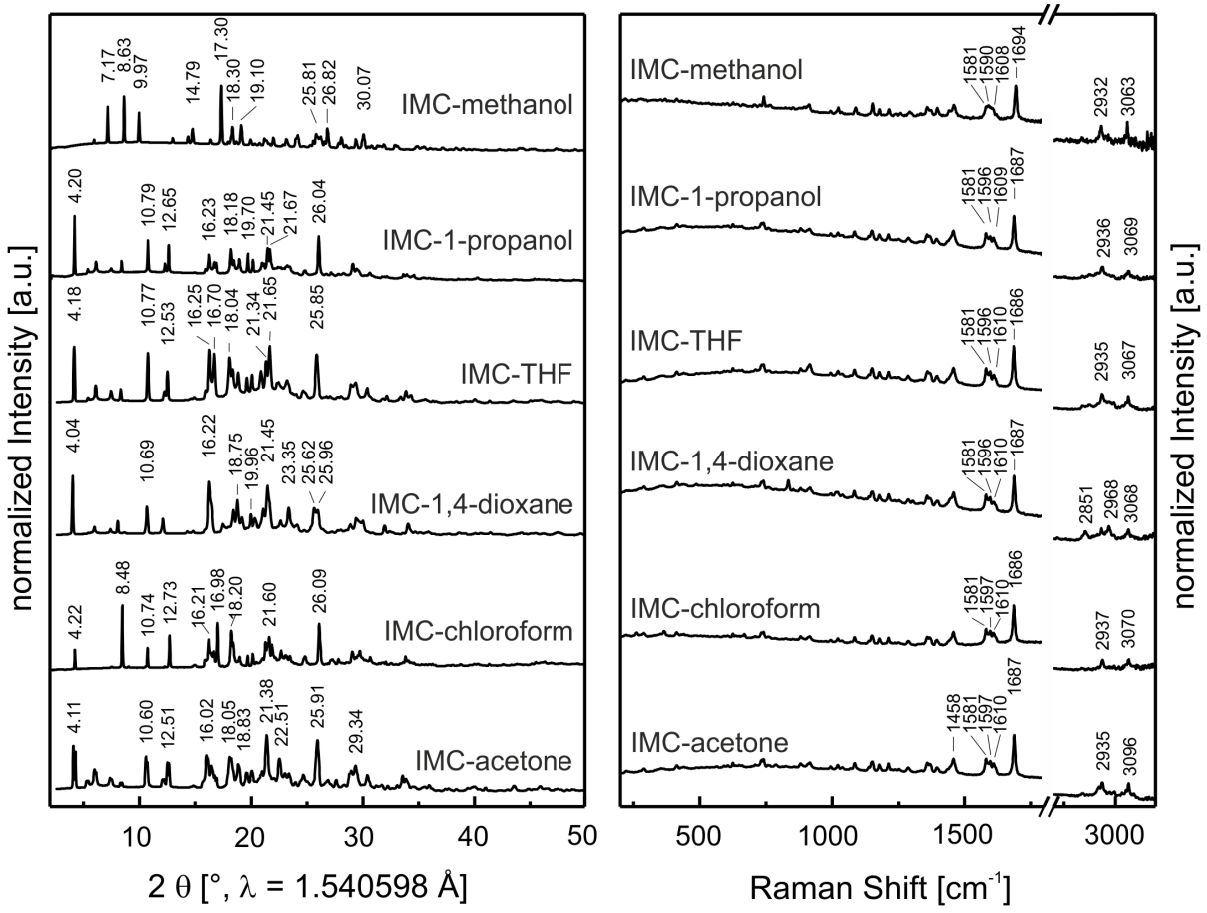

Figure 4.12: The XRD patterns (left) and Raman spectra (right) of indometacin solvates with different organic solvents are presented. Important reflections and Raman bands are highlighted.

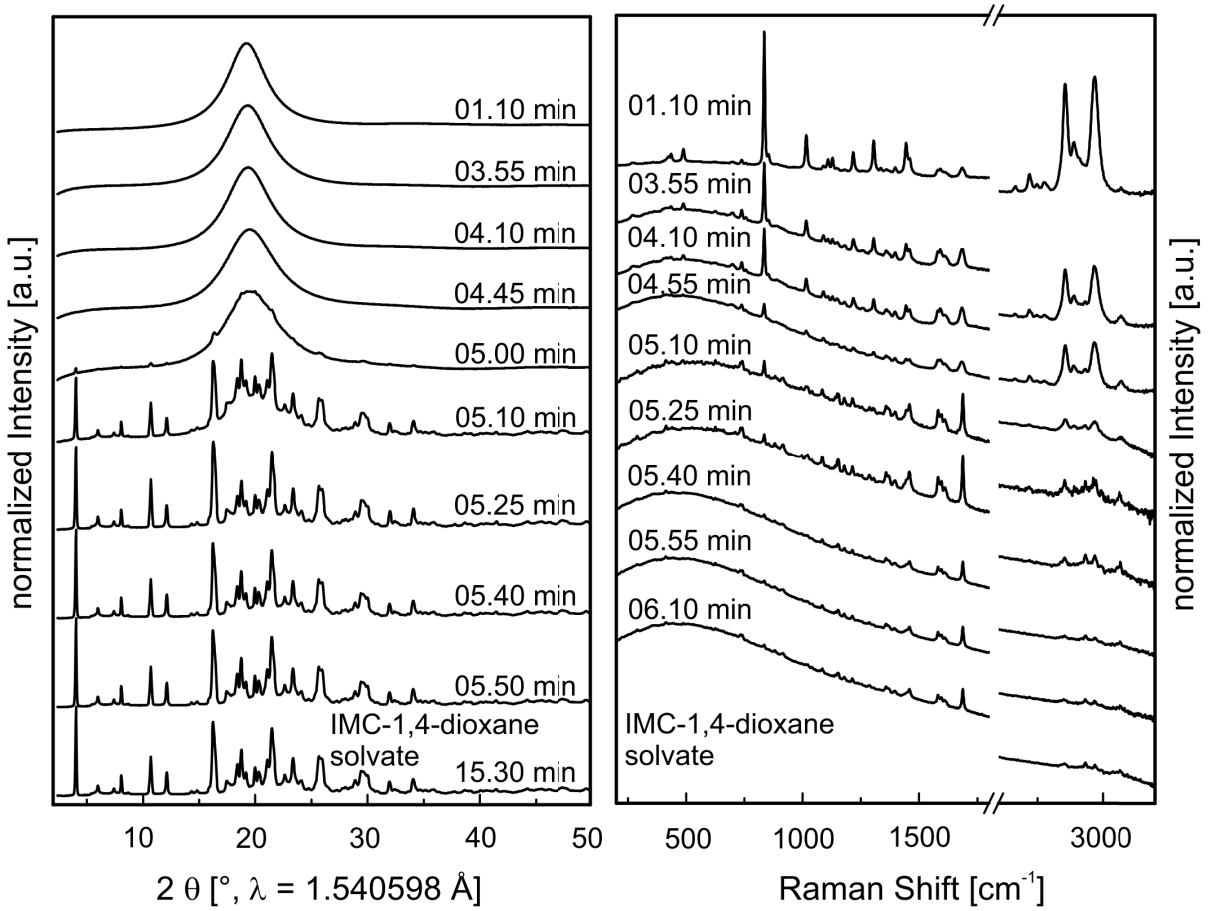

Figure 4.13: The crystallization process of the indometacin solvate with 1,4-dioxane is studied time-resolved with synchrotron XRD (left) and Raman spectroscopy (right). The XRD patterns and Raman spectra show that the crystallization from liquid solution proceeds via a mixture of solvent and an amorphous phase to the final crystalline solvate.

At this point, the structures of the solvates can be classified into two groups: the structure of the methanol solvate and the other solvates. For the structure solution of the methanol solvate a high angle-resolved PXRD pattern was recorded at the synchrotron (PSI, Villigen, Schwitzerland). This XRD pattern is of good quality and allows the indexing, structure determination, and structure refinement of this solvate. Figure 4.14 A displays the structure of the methanol solvate and the picture below the corresponding Rietveld refinement. The simulated and measured powder pattern are in good agreement. The solvate forms a monoclinic space group $P2_1/n$ (a = 20.90997(12) $\AA$, b = 5.03039(3) $\AA$, c = 18.09001(13) $\AA$, β = 100.6988(7)°, V = 1869.73 $\AA^3$). In the unit cell, four indometacin molecules and four methanol molecules are included. This stoichiometry is consistent with the TG analysis described in section 4.3.2. The structure is determined by the hydrogen bonds between the carboxyl groups of the indometacin molecules and the methanol molecules (see Figure 4.14 A, orange colored, p. 70). Within the crystal structure of pure indometacin the formation of the synthon between two carboxyl groups is characteristic, and it is crucially involved in the stability of the structure. In this solvate structure, this synthon is extended by additional two methanol molecules resulting in a stable six ring of hydrogen bonds. The carboxyl group and methanol molecule are arranged in a slightly shifted manner. From a side view, a base of a chair arrangement can be assumed. The hydrogen bond length are $d_{C=O\cdots H-OCH_3}$ = 1.535 $\AA$ and $d_{O-H\cdots O-HCH_3}$ = 1.753 $\AA$. Compared with the hydrogen bonds of the synthon in the α and γ structure ($d_{O-H\cdots O=C}$ = 1.60-1.87 $\AA$), the hydrogen bonds are in the same length range, which suggest a high stability of the methanol solvate.

The indexing of the PXRD patterns of the solvates with chloroform, acetone, and THF suggests similar fundamental structure features (see Table 4.4, p. 71). All solvates have the same space group and only differ slightly in the lattice parameters and volume of the unit cell. Compared to the structure parameters of the polymorphs and the other solvates of indometacin, the unit cell is larger. Sixteen indometacin molecules and eight solvent molecules are included in the large cell resulting in a stoichiometry of 2:1 (indometacin:solvent). Depending on the chemical properties of the solvent strong or weak interactions between the solvent and the carboxyl group of the indometacin molecules can occur. The stability of the corresponding solvate is associated with the strength of the intermolecular interactions. A closer look along the c-axis reveals single or double row arrangements of the solvent molecules within the space of the fundamental indometacin molecule framework (see Figure 4.15, purple areas, p. 73). The indometacin molecule fragments with the chlorine are faced towards each other, while the carboxyl groups of

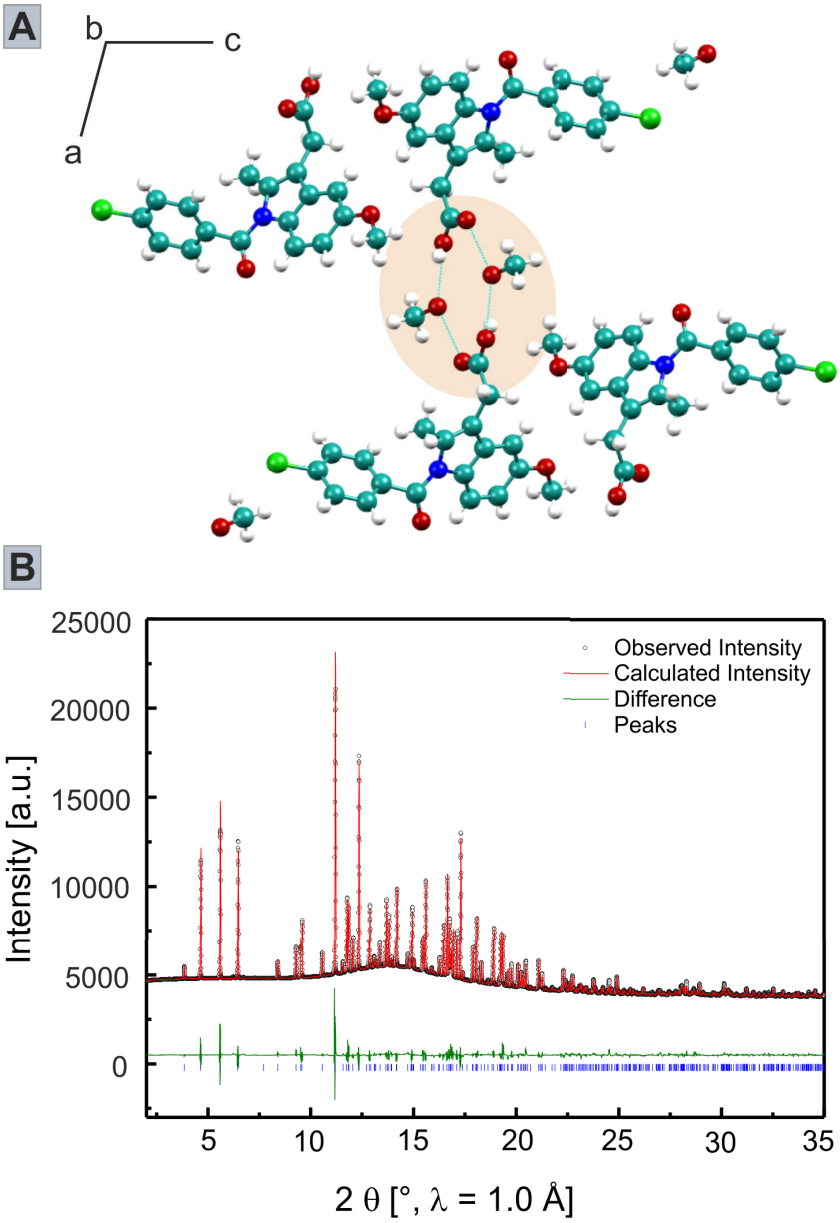

Figure 4.14: A) The structure of the indometacin-methanol solvate is presented along the b-axis (turquoise = carbon, red = oxygen, blue = nitrogen, white = hydrogen, green = chlorine). The turquoise dashed line emphasizes the hydrogen bonds. The structure has a characteristic synthon (orange colored) consisting of two methanol molecules and two carboxyl groups of two different indometacin molecules. B) The Rietveld refinement of the indometacin-methanol solvate structure with the scattered X-ray intensity under ambient conditions is shown as a function of the diffraction angle 2θ. The observed pattern (black circles), the best Rietveld fit profile (red line), the reflection positions (blue tick marks), and the difference curve (green line) between the observed and calculated profiles are visible. The R values are $R_p = 2.366$ and $R_{wp} = 4.158$. They refer to the Rietveld criteria of fit for profile and weighted profile defined by Langford and Louer.[175]

Table 4.4: The structure information of the indometacin solvates with chloroform, acetone, tetrahydrofuran (THF), and 1,4-dioxane are suggested by the PXRD experiments.

Solvates	IMC-chloroform	IMC-acetone	IMC-THF	IMC-1,4-dioxane
Crystal system	monoclinic	monoclinic	monoclinic	monoclinic
Space group	C2/c	C2/c	C2/c	$P2_1/a$
a [$\AA$]	42.784(9)	43.071(6)	43.524(12)	44.983(6)
b [$\AA$]	5.3809(8)	5.3509(6)	5.3827(9)	5.2407(5)
c [$\AA$]	33.739(6)	33.787(4)	33.500(5)	16.8368(14)
α [°]	90	90	90	90
beta [°]	102.088(8)	102.182(9)	101.683(14)	102.503(8)
γ [°]	90	90	90	90
Volume [$\AA^3$]	7595(2)	7611.5(17)	7685(3)	3875.0(7)
R_p	6.04	7.74	5.96	7.85
R_{wp}	10.18	12.77	9.02	13.05

the indometacin molecules protrude into the solvent channels. The chloroform molecules interact with the carboxyl groups forming medium strong halogen bonds. The chlorine atoms of the chloroform are the electron acceptors (Lewis acid) and the oxygen atoms of the carboxyl group (Lewis base) are the electron donors. In the solvate structure, two chloroform molecules form with two carboxyl groups ring-shaped interactions, which support the stability of the overall structure (see Figure 4.16 A, p. 74). In the case of acetone, no closed unities of interactions between the solvent and the carboxyl groups are visible. A hydrogen bond occurs between the carbonyl group of the acetone molecule and the hydroxyl unit of the indometacin carboxyl group (see Figure 4.16 B, p. 74). The formation of a six-ring-like arrangement between two acetone molecules and two carboxyl groups similar to the structure in the methanol solvate cannot be observed. The reason for that might be the steric hinderance of the two acetone methyl groups. This suggests a reduced solvate stability with acetone as the solvent. A comparable situation occurs in the solvate structure with THF. The oxygen atom of the THF molecule interacts with one indometacin carboxyl group (see Figure 4.16 C, p. 74).

The solvate with 1,4-dioxane differs more strongly from the letter three mentioned solvates. The dimension of the a- and b-axis is similar to the values of these structures, only the c-axis is half the size (see Table 4.4, p. 71). This leads to a changed space group and reduced cell volume which includes eight indometacin and four 1,4-dioxane molecules. Looking along the c-axis the channel arrangement of the solvent molecules is not defined, but they are rather integrated. One oxygen of the solvent molecule interacts with one

carboxyl group of one indometacin molecule (see Figure 4.17 B, p. 75). This interaction seems to disturb the formation of the favored synthon consisting of two carboxyl groups of indometacin molecules. The less optimal intermolecular interaction influences the stability of this solvate.
A structure suggestion for the solvate with 1-propanol is missing, because of the insufficient quality of the X-ray scattering pattern. The similar X-ray scattering pattern in comparison to the other solvates indicates close related structural features of the indometacin-1-propanol solvate.

The desolvation process is often used to isolate the pure material or to study the stability of the solvates. It is not unusual that this process is complex and proceeds via several processes. The following section describes the structural changes during the desolvation process of the indometacin solvates. The crystallized solvates were positioned in the levitator. A heated nitrogen flow controlled the environment of the compound. During the gradual heating process in the levitator *in situ* synchrotron XRD experiments were performed to analyze the transformations. The desolvation experiments demonstrated that in particular the methanol, acetone, and chloroform solvate exhibit a complex transformation behavior with metastable crystalline forms as intermediates (see Figure 4.18 and 4.19). The experiments with 1,4-dioxane, THF, and 1-propanol only showed a single transition of the solvate to the α form or a mixture of α and γ.
The methanol solvate can be identified by the distinctive signals at 2θ = 7.16, 8.58, 9.95, 17.24° (see Figure 4.18, enlargement, p. 77). Heating this product leads to the development of new reflexes at 9.54° 2θ and 10.38° 2θ. They start to develop at near the boiling point of methanol (65 °C). With increasing temperature up to 80 °C these signals gain in intensity and additional characteristic signals at 2θ = 16.64, 20.11, 22.63° evolve. The developing structure can be assigned as the polymorph δ (see Figure 4.18, enlargement, p. 77). The XRD pattern and Raman spectrum of this polymorph corresponds to the ones presented in the literature.[139] On the other hand, the intensities of the significant reflexes of the methanol solvate decrease and vanish completely at the temperature of 80 °C. The structure of δ is so far unknown. In the corresponding XRD pattern, the reflexes are broadened resulting from smaller crystal sizes. The observed process points out that the crystal structure of the solvate is destroyed with the increasing temperature. The solvent molecules are displaced evoking a rearrangement of the indometacin molecules. In the crystal lattice structure of the methanol solvate, the indometacin molecules are preliminary coordinated by the methanol molecules in such way that the formation of metastable

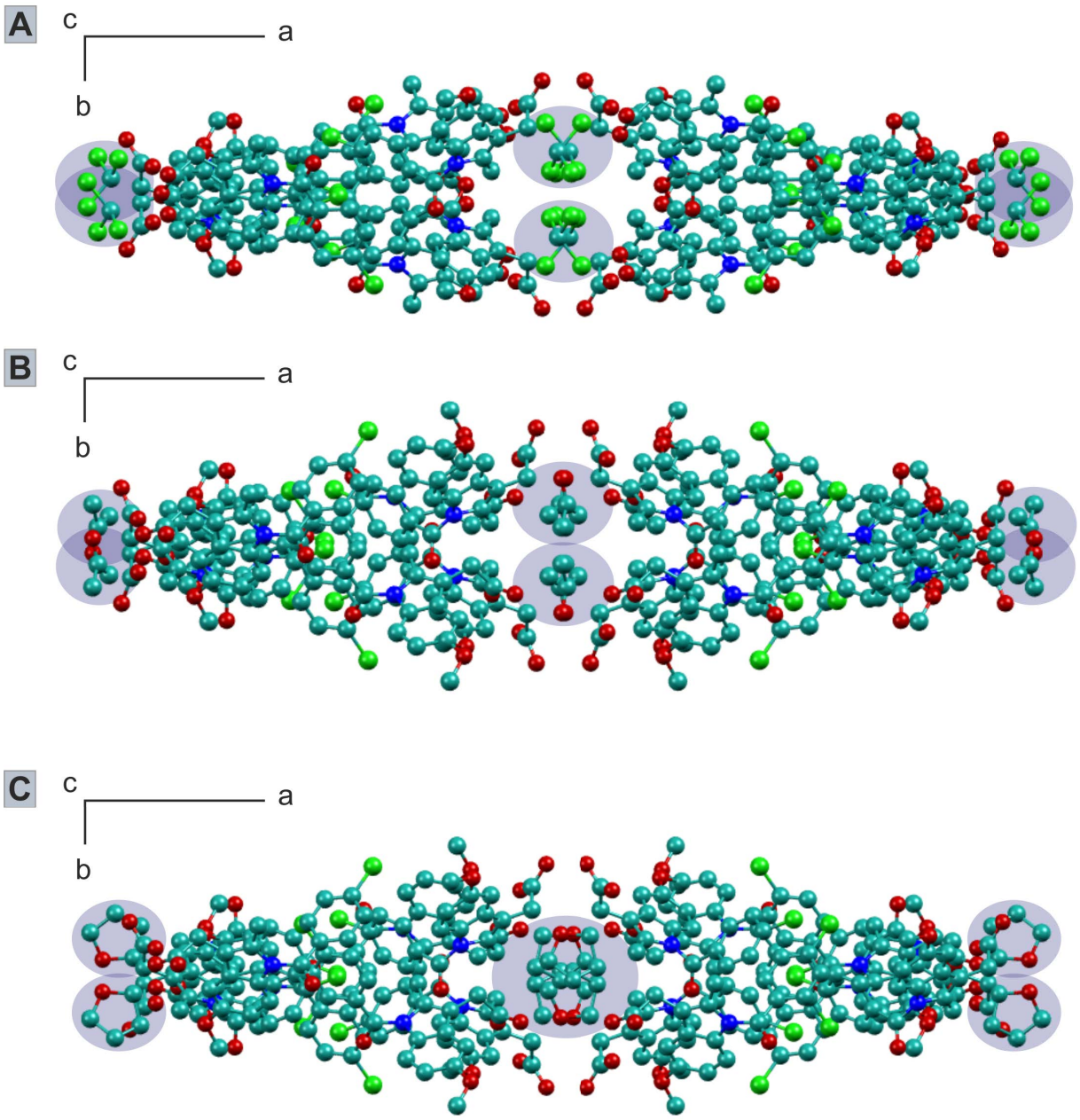

Figure 4.15: The structures of the indometacin solvates with chloroform (A), acetone (B), and THF (C) are presented along the c-axis (turquoise = carbon, red = oxygen, blue = nitrogen, green = chlorine). For the sake of clarity, the hydrogen atoms are left. The purple colored areas mark the channel arrangement of the solvent molecules in the form of rows along the c-axis.

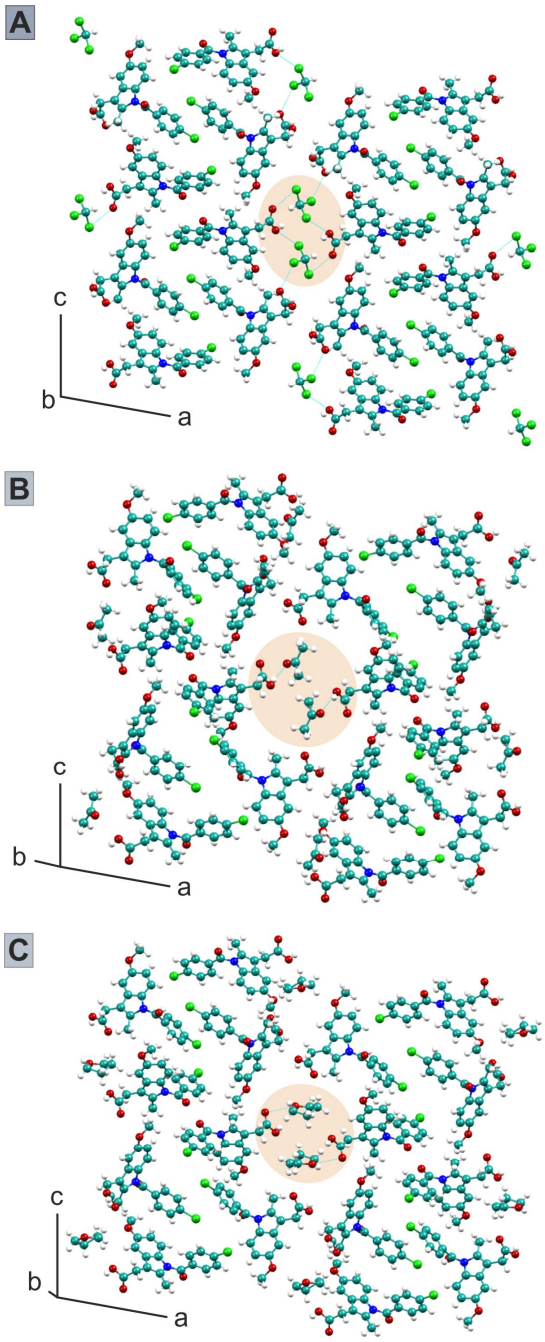

Figure 4.16: The structures of the indometacin solvates with chloroform (A), acetone (B), and THF (C) are presented along the b-axis (turquoise = carbon, red = oxygen, blue = nitrogen, green = chlorine). The orange colored areas mark the intermolecular bonds of the solvent molecules with the carboxyl groups of the indometacin molecules.

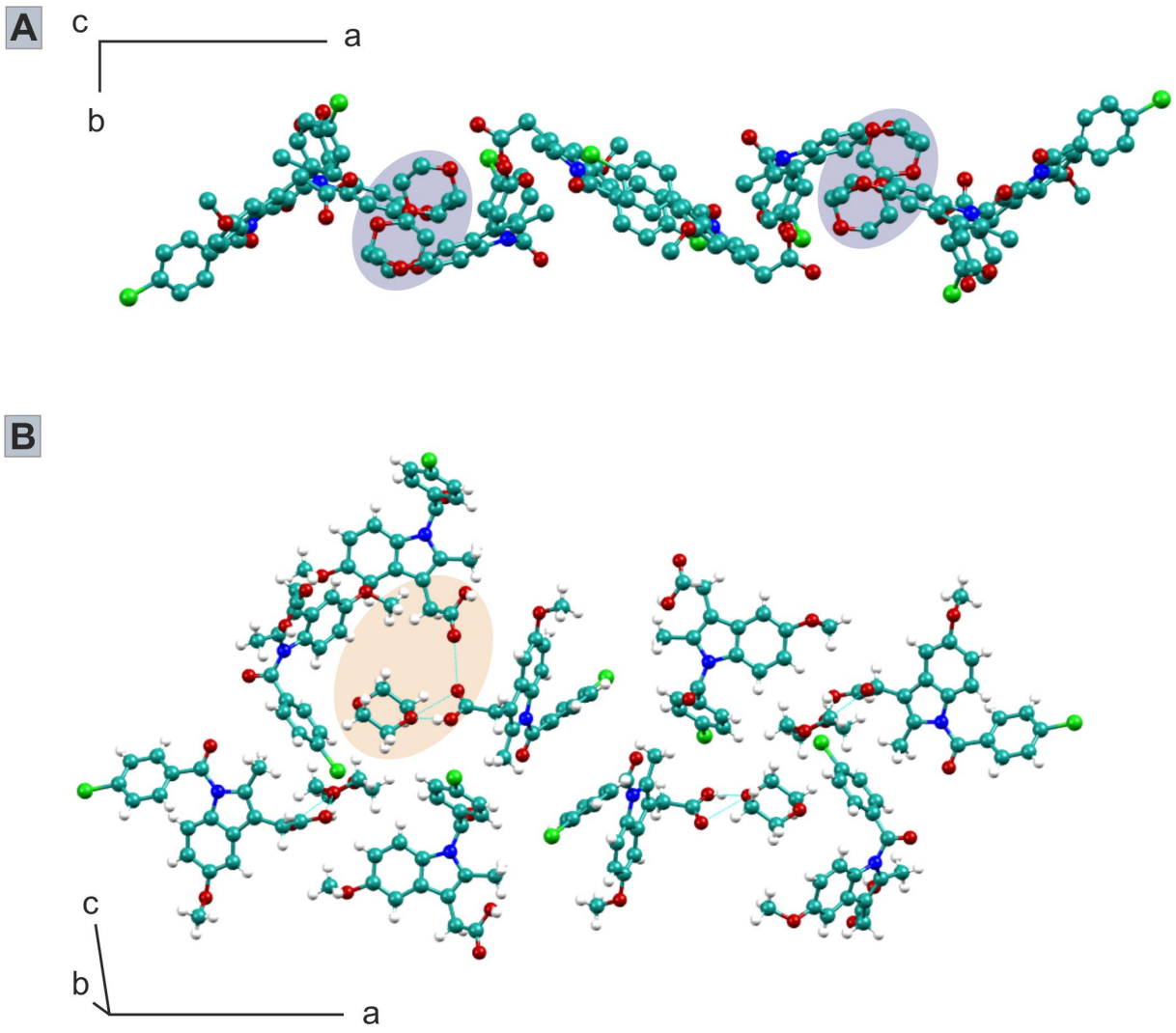

Figure 4.17: A) The structure of the indometacin solvate with 1,4-dioxane is presented along the c-axis (turquoise = carbon, red = oxygen, blue = nitrogen, green = chlorine). For the sake of clarity, the hydrogen atoms are left. The purple colored areas mark the integrated 1,4-dioxane molecules. B) The same structure is shown along the b-axis. The orange colored areas mark the intermolecular bonds of the solvent molecules with the carboxyl groups of the indometacin molecules.

polymorph δ is facilitated. This form is stable for a broad range of temperature. At a temperature of 135 °C, another transformation to the modification α takes place. Significant signals of form α at 2θ = 6.97, 8.42, 10.23, 11.49, 30.73° (λ = 1.540598 $\mathring{A}$) become more intense; at the same time the reflexes of δ decrease in intensity. The corresponding Raman spectra of the crystalline forms presented in Figure 4.18 were recorded in separated experiments. Finally, with a temperature more than 150 °C no further transitions could be detected.

The structure of the intermediate δ has not been solved until now. Comparing the Raman spectrum of δ with the Raman spectra of the known polymorphs α and γ gives hints about structural features. The carbonyl and carboxylic acid groups in the indometacin molecule are capable of participation in hydrogen bonds. Thus, interpretation of the C=O band is suitable to analyze the hydrogen bond arrangements in the crystal structure. The assignment is based on published theoretical predictions.[176] The theoretical predictions include the Raman spectra of a dimer, corresponding to the cyclic hydrogen bonds between the carboxylic acid groups in the γ form, and a trimer, simulating the asymmetric unit of the α form with hydrogen bonds between the carboxylic acid groups of the first two molecules and the hydrogen bonds between the carbonyl group of the second and the carboxylic acid group of the third molecule. The different hydrogen bonds in the trimer motifs result in two vibration modes of the carbonyl signals at 1649 cm^{-1} and 1680 cm^{-1}, and one mode for the carboxylic acid group at 1689 cm^{-1} in the α polymorph. The more simple dimer motif in γ causes one vibration signal for the carbonyl group at 1698 cm^{-1}. The δ polymorph has one characteristic signal at 1689 cm^{-1} for the carbonyl vibration. This indicates a similar hydrogen bond arrangement in comparison to γ. The carboxylic acid groups of indometacin molecules could also form a cyclic synthon via hydrogen bonds. This vibration mode is shifted to a lower wave number in δ.

The acetone and chloroform solvate crystallize within a few minutes in the levitator. The enlargements of the XRD patterns suggest the similar structures for both solvates (see Figure 4.19, p. 78). The high similarity complicates the differentiation by the XRD patterns. Heating the solvates in the levitator, the solvate structures start to change from a temperature of 70 °C upwards (transition from yellow to light purple colored area). This temperature is higher than the boiling points of acetone (56 °C) and chloroform (61 °C). In both cases, new reflexes of intermediates increase in intensity and the distinctive solvate signals continually lose intensity. The intermediates have characteristic reflexes at 2θ = 3.90, 10.38, 11.5, 15.70, 29.23° in the XRD patterns. In both cases, the intermediate can be identified as the polymorph β. This metastable form was reported to form only

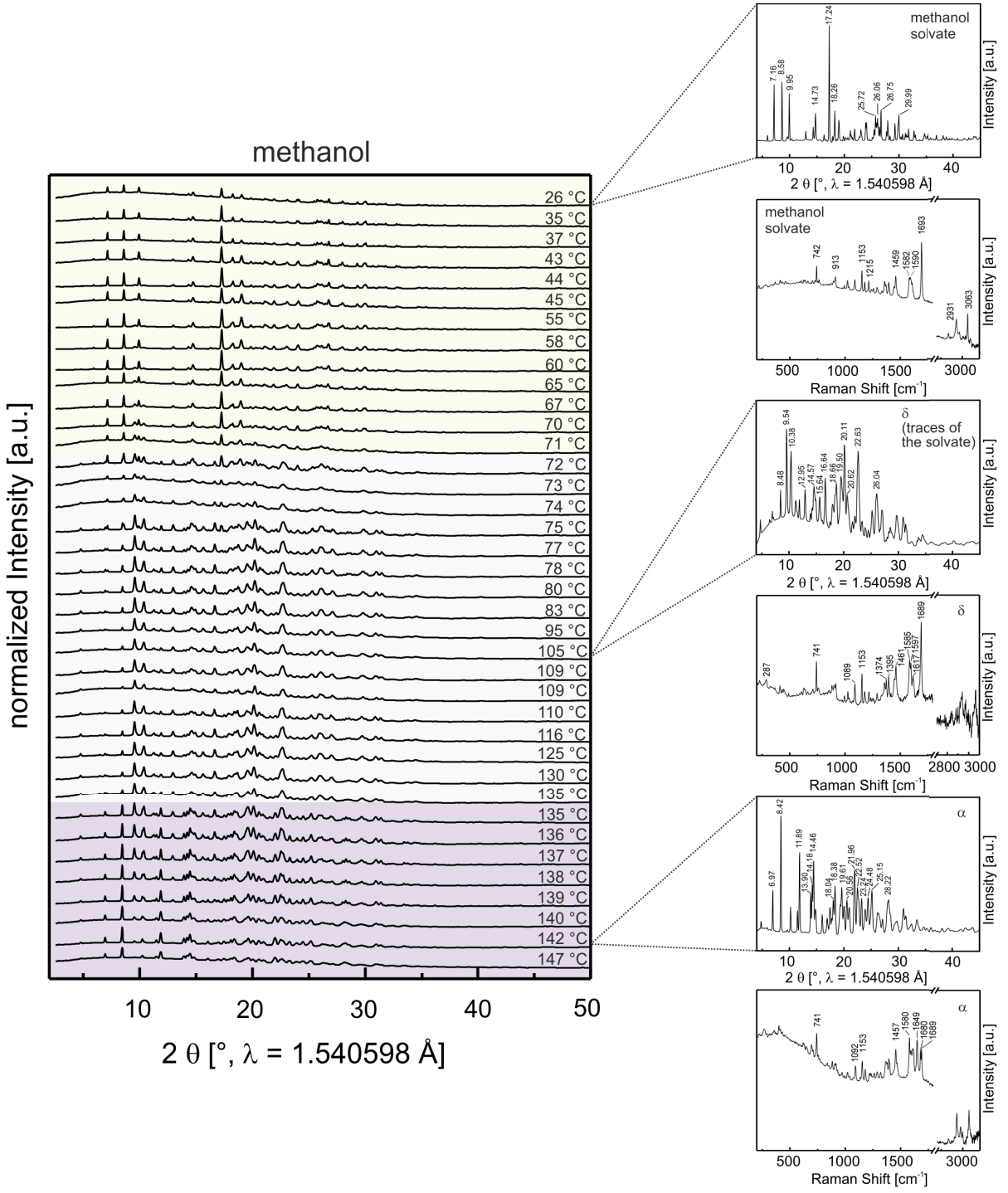

Figure 4.18: The XRD patterns of the heating process starting from the indometacin-methanol solvate via the δ to the α form are presented. The different colored areas mark the appearance of the three crystalline forms (yellow = solvate, light purple = δ, medium purple = α). The enlargements show the XRD patterns and the Raman spectra of the crystalline forms. The Raman spectra are measured in a separate experiment.

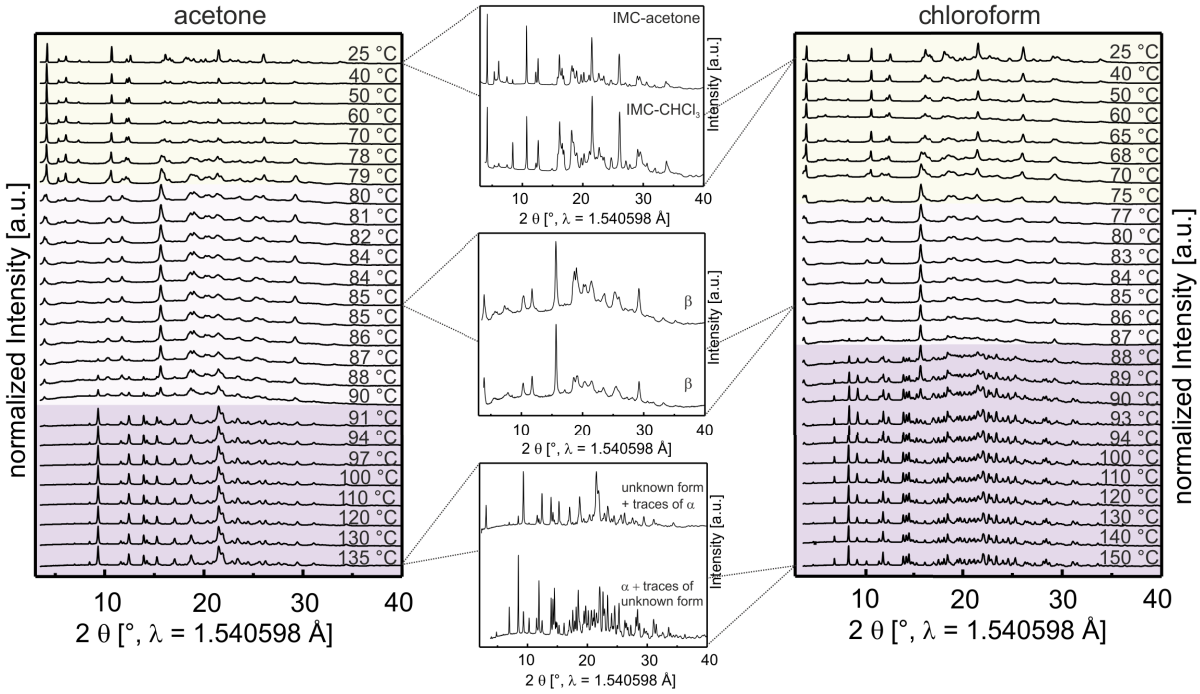

Figure 4.19: The XRD patterns of the heating process of the indometacin-acetone (left) and -chloroform solvate (right) are shown. The different colored areas mark the appearance of the different crystalline forms (yellow = solvate, light purple = β, medium purple = α and unknown form). The enlargements compare the XRD patterns of the different crystalline stages during the heating process.

during the recrystallization process from benzene.[146,177] During the desolvation process the thermal energy breaks the interactions of the solvent molecules with the indometacin molecules. The solvent evaporates. The indometacin molecules left behind reorder themselves in a more stable structure forming the β polymorph. At a temperature of approx. 88 °C, a second transition is detectable (transition from light to medium purple colored area). Again different signals of the new crystalline phases start to develop. The specific β reflexes diminish the intensity with increasing temperature. Signals of the α polymorph can be assigned in both heating processes, with the difference that α is the main phase when starting from the chloroform solvate. Additionally, reflexes at 2θ = 9.29, 11.62, 12.42, 15.26, 17.05, 18.72° are visible at the end of second transition. Some of the signals coincide with signals of the η[139] polymorph, but a clear assignment is difficult. In the case of the acetone solvate, theses reflexes dominate the XRD pattern with small proportion of α reflexes.

4.3.2 Thermodynamics and kinetics of the indometacin solvates

Besides the structural studies of the solvate, the thermal analysis complements the understanding of the structural composition. Investigating the structure stability of the solvates, the thermodynamics and kinetics can provide appropriate theoretical framework to assess the relative stability of the molecular structures.

The thermal analyses include the differential scanning calorimetry (DSC) and thermal gravimetric (TG) investigations. Knowing the mass of the to be examined solvate at the beginning and the end after the evaporation of the solvent, the stoichiometry of the solvate is accessible. The TG analyses of the indometacin solvates lead to the following solvent/IMC molar ratios: 0.94 ± 0.04 in methanol, 0.49 ± 0.01 in THF, 0.51 ± 0.01 in 1,4-dioxane, 0.52 ± 0.03 in 1-propanol, 0.47 ± 0.03 in chloroform, and 0.50 ± 0.05 in acetone (see Appendix for detailed calculations). Thus, all compounds are hemisolvates except for methanol. The result for the methanol solvate is in good agreement with the structural determination in section 4.3.1. The obtained stoichiometries are also consistent with the previous XRD studies indicating a strong structural similarity of all solvates except the methanol one.

The DSC experiments give an idea about the stability of the solvates (see Figure 4.20, p. 80). The desolvation temperature range of the solvates extends to a wide temperature from 85 °C to 130 °C. The desolvation temperature range is always above the boiling point of the corresponding solvent, which is a hint for medium strong interactions of solvent molecules with the indometacin host framework.

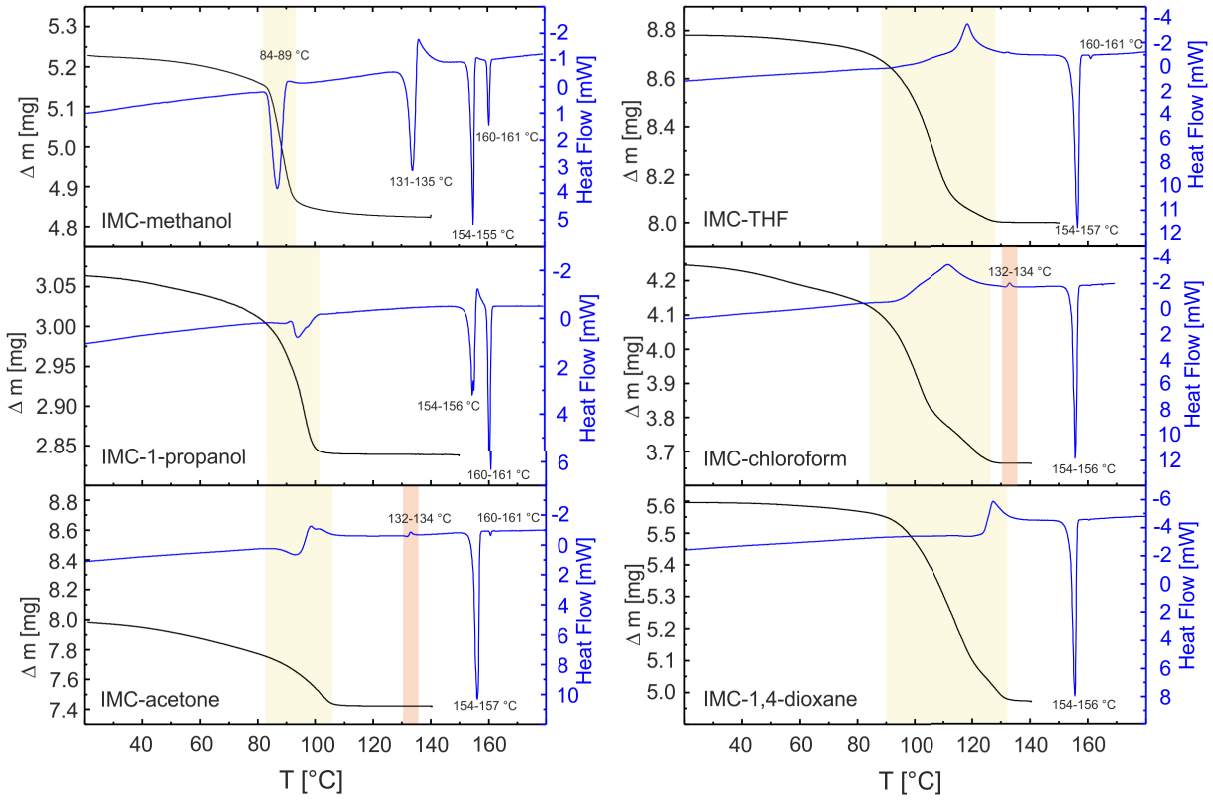

Figure 4.20: The TG analysis (black) and the corresponding DSC experiments (blue) of the indometacin solvates are displayed. The yellow marked areas show the desolvation process of the solvates. The acetone and chloroform solvates have characteristic thermal events at 132-134 °C indicating a solid-solid transition (light red area).

The DSC curve of the methanol solvate shows six thermal events in the range of 70-170 °C. The first endothermic peak which starts at 84 °C and ends at 89 °C corresponds to the desolvation process due to the simultaneous mass loss. This peak is very sharp. This temperature range matches the findings found in the XRD studies where the first solid-solid transition from the methanol solvate to the δ form were detected. The significant desolvation peak allows the determination of the corresponding enthalpy for the desolvation process of the methanol solvate. The value is $\Delta_r H_m^\circ = 36.25 \pm 1.04$ kJ/mol (per mol of methanol or solvate) which is close to the vaporization enthalpies of methanol at 298 K ($\Delta_{vap}H^\circ = 37.43$ kJ/mol)[178] and 373 K ($\Delta_{vap}H^\circ = 32.67$ kJ/mol).[179] This value suggests a medium strong solvate structure with methanol. After the desolvation, a slight exothermic event is apparent which could indicate the conversion of the solvate to a crystalline structure formed upon solvent loss. The second endothermic peak goes from 131 °C to 135 °C. It is the melting point of form δ, which was first described by Borka in 1974.[137] The melting of form δ occurs concomitantly with the crystallization of form α or a mixture of α and γ. Finally at 154-155 °C, there is the melting peak of form α that can be followed by the crystallization of form γ which melts between 159-161 °C.
A different behavior is evidenced by the DSC analyses of the other solvates, where the desolvation process corresponds to a broad endothermic peak followed by an exothermic peak. If this is indeed the case, the desolvation process originates the metastable amorphous phase, which immediately crystallizes to a more stable crystalline phase. Further analysis of the TG and DSC results for the THF, chloroform, and 1,4-dioxane solvates shows a two-step desolvation process, the first one with a higher rate at the beginning followed by a second one with a lower rate. This phenomenon has already been described by Nicolai *et al.*[180] who reported the first step at 100-110 °C and the second one above 110 °C for the indometacin-THF solvate. The first step was assigned to desolvation and the second to the solvent adsorption on the surface of indometacin. The temperature range is in agreement with these three examples. The first step is likely to correspond to a release of the solvent molecules from the solvate framework associated with the change of structure and composition. The second part is the evaporation of adsorbed solvent molecules running and supported by an exothermic event, the crystallization process of a metastable intermediate.
In all cases, endothermic peaks at approx. 155 °C and 160 °C are visible and belong to the melting process of form α and γ, respectively. After the melting of form α, a shoulder of an exothermic process follows. This is a sign for the recrystallization of form γ from the melt. The acetone and chloroform solvates show additionally characteristic

thermal events at 132-134 °C in the DSC (see Figure 4.20, light red area, p. 80). They are typical for solid-solid conversions without a fusion process. These observations support the previous XRD results, where the β form is obtained after the evaporation of acetone and chloroform molecules out of the solvate crystal structure. The β polymorph tends to transform at approx. 133 °C to the more stable form α in both cases.

Considering the structural and thermal analyses of the indometacin solvates, the results demonstrate a strong dependence of the stability on the ability of the solvents to form hydrogen bonds with the carboxyl group of the indometacin molecules. Thus, methanol is suitable to form stable hydrogen bonds due to its size and properties. The methanol solvate is significantly more robust than the hemisolvates with other solvents. The hemisolvates show similar structural features suggesting a similar base framework of indometacin molecules. The solvent molecules do not form hydrogen bonds in a perfect manner. They are more loosely bound in the solvate structures. The basic indometacin molecules framework might form cavities which act as solvent molecule cages. In most cases, the solvent molecules are arranged in channels.

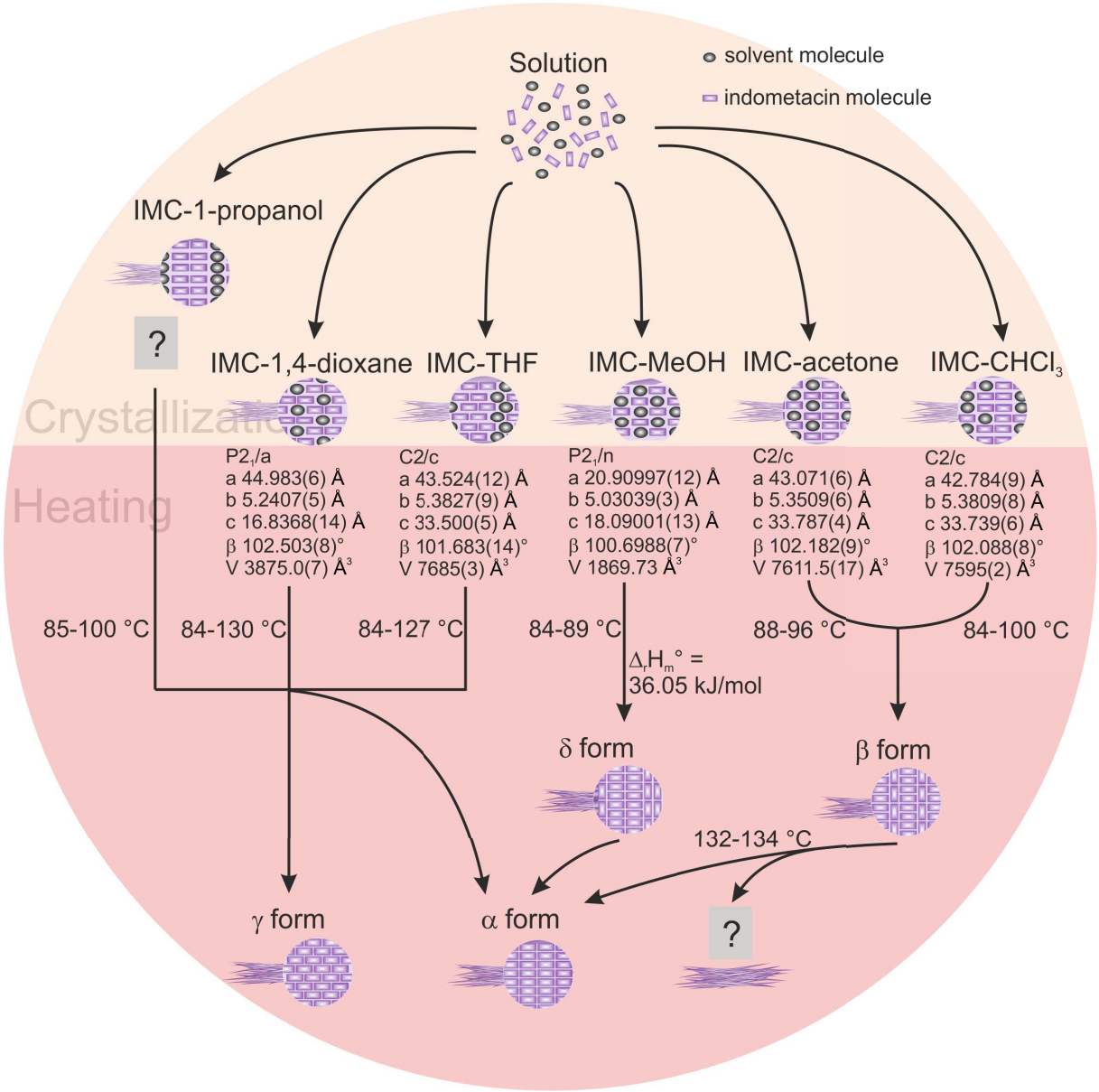

Figure 4.21: The graphic sums up the crystallization results of indometacin from different organic solvents. The formed solvates have undergone heat treatments. The parameters and the intermediates of the transformation pathways to the polymorph α and γ are presented.

5 Discussion

The crystallization results of the organic model systems present three aspects which are guiding the pathways of processes from liquid solution: the levitation in an acoustic field, the use of organic solvents, and the concentration or saturation of the solution during the crystallization. The following sections discuss the influence of these three parameters on the sample, crystallization pathways, and the formation of intermediates and polymorphs of the different systems.

5.1 Contactless crystallization

The droplet crystallization in the levitator allows the evaporation of the solvent via the whole droplet surface without the influence of the any solid surfaces on the nucleation and crystallization process. The custom-made acoustic levitator with flowing nitrogen in the climatic unit stream additionally prevents the entry of foreign particles. The setup and the acoustic field ensure the mixing of the liquid solution within the droplet and enable an approaching homogeneous crystallization. The sample is accessible from all sides during the whole investigation process. This advantage can be used to combine different analytical methods to study the crystallization.
The evaporation principle is based on the different volatilization behavior of two compounds. The dissolved analyte has a low vapor pressurr and the solvent has a relatively high vapor pressure. By evaporating the solvent amount decreases and the analyte concentration rises in the droplet. Thus, the evaporation is accompanied by a mass loss. At the surface of the droplet, the solvent changes from the liquid into the gas phase. Diffusion and convection processes carry the resulting solvent vapor into the surroundings. A thermodynamic equilibrium of the evaporation and condensation between the solvent and its gas phase occurs. This results in a saturation vapor pressure in the immediate environment of the droplet. The successive concentration increase is obtained by the uneven distribution of the solvent and the dissolved analyte in the liquid and gas phase during the thermodynamic equilibrium. This aspect is supported by the flowing nitrogen stream

accelerating the removal of the solvent molecules from the immediate gaseous surroundings of the droplet.
The ultrasonic field experiences a spatial weakening due to the propagation of sound waves in space and the scattering of these waves at the levitated sample.[181] This induces the acoustic convection. In the immediate surroundings of the sample, toroidal vortices systems arise in the gas phase. They form a kind of shell around the sample. The gaseous transfer medium, the air, flows radially in the equatorial plane towards the levitated material, and it flows off axially at the pols of the sample. These two convection currents overlap resulting in an increase of the mass transfer at the surface of levitated liquids.[182] The described effects allow a thorough mixing process within a droplet. This prevents temperature gradients, which can arise due to the evaporation of the solvent, within the droplet. Thus, a maximum temperature increase of 1 °C, caused by the ultrasonic field and the evaporative cooling, are balanced.[109] The temperature during the crystallization process can be regarded as constant. The crystallization can start in the bulk solution, but the initiation at the air-solution surface is very likely.

The crystallization experiments of the model systems show clearly that the polymorphs of ROY and paracetamol arise as pure crystalline forms. The benefit of the use of the acoustic levitator stems from the fact that interactions with solid surfaces influencing the nucleation and growth are avoided. The solid surface induced crystallization and heterogeneous nucleation can promote independent nucleation processes at different localities. This can increase the possibility of concomitant polymorph crystallization.
The isolation of the pure crystalline form I from liquid solution is common.[141] But the targeted crystallization of pure crystalline form II in glass containers was difficult to realize because of its instability and fast transformation in presence of the nucleus contamination to form I. The used setup enables the control of sample surrounding conditions and prevents the heterogeneous nucleation. This might be the reason for the purity of the crystallization products.

5.2 Influencing parameters of crystallization

The crystallization experiments of the model systems clearly demonstrate different crystallization pathways.These pathways are strongly influenced by the solvent, concentration, temperature, and humidity. The results mainly focus on the steering effect of different organic solvents and the concentration at different steps during the crystallization.

5.2.1 Guiding the crystallization via the solvent

The study of the solvent influence was implemented by using the acoustic levitator and keeping the temperature and humidity constantly. In this way, the solvent becomes the central influencing parameter and the impact of the solvent on the outcome of a distinct polymorph could be elucidated.
The solvents can impact the crystallization process in different ways. The results of the crystallization experiments with the compound ROY show an influence of the solvents on the structure of the crystallizing product. In this special case, the conformation of the ROY molecules is one of the key features determining the crystal structure of the crystalline material. In liquid solution, conformers of ROY have preferred nitrophenyl fragments arranged perpendicularly to the thiophene rings, in other words θ_{thio} corresponds roughly to 90°.[128] The yellow colored polymorphs (Y, YN, YT04) adopt conformations with a torsion angle θ_{thio} of 104-113°, which are close to 90°. Considering that Y is the most stable modification at ambient conditions, this might be an explanation for the favored formation of polymorph Y in present of solvent amounts. Additionally, Y forms stabilizing intermolecular hydrogen bonds between the nitrile and amino groups.
Besides the intramolecular changes in terms of different conformations, the intermolecular arrangements of neighboring molecules also have to be considered to understand the crystal forming process and the possible influence of the solvent on this process. Therefore, the centroids of the ROY molecules, which are in the immediate vicinity in the crystal structure, were calculated, and the distances between them are determined to gain information about the coordination environment. Looking at the distance contributions of each polymorph, it is obvious that the polymorphs have their specific distribution patterns (see Figure 5.1 A, p. 88). When crystallization experiments in the acoustic levitator start with concentrations under the saturation, the ROY molecules are completely surrounded by solvent molecules in liquid solution. The evaporation causes an increasing concentration and, therefore, the ROY molecules move closer to each other. The formation of a nucleus requires a certain arrangement and alignment of the analyte molecules. They

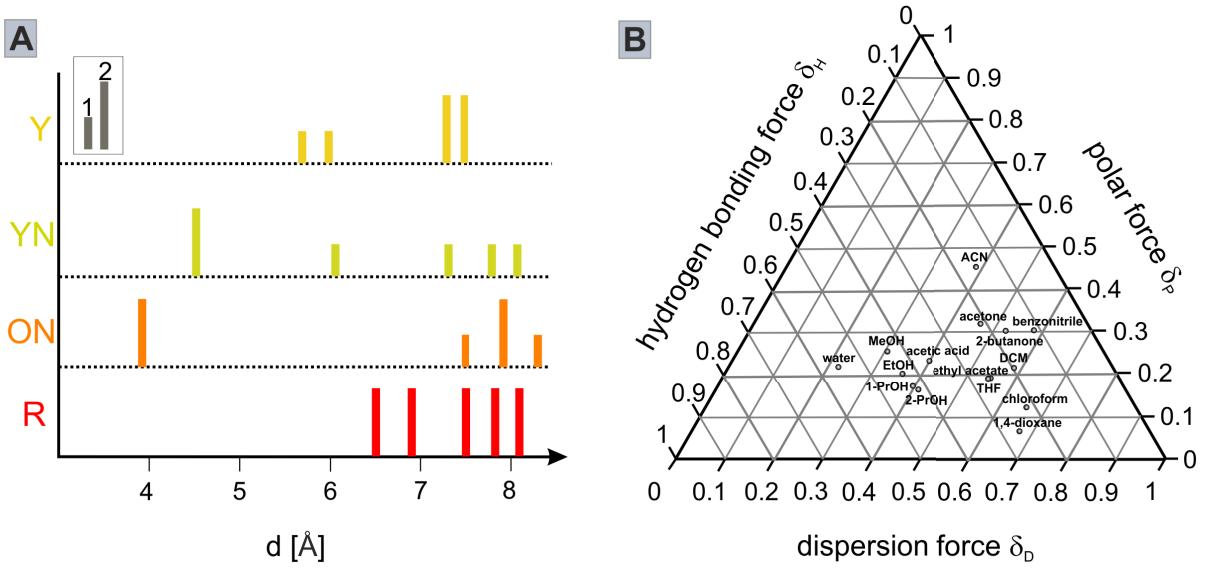

Figure 5.1: A) The graphic shows the distance distributions between the neighboring ROY molecules within the polymorphs Y, YN, ON, and Y. The distances between the centroids are considered. B) The teas plot divides the total cohesive energy of different solvents in three components: the dispersion, polar, and hydrogen bonding force.

need sufficient mobility to implement these steps, so that the present of solvent molecules can hinder sterically this procedure. In the crystal structure of Y, one ROY molecule has six nearest neighbors in the distance of 5.83-7.47 $\AA$. Excluding the polymorph R because of its conformers' instability in liquid solution with the small torsion angle θ_{thio} of 21.7° (see Appendix, Table 6.1, p. 107), the neighboring molecules in the crystal structure of YN and ON are much closer in comparison to Y (see Figure 5.1 A, p. 88). The solvent residues might exacerbate the ROY molecules to pack in a denser way and, thus, to form crystals of YN and ON. This could be a further reason for the favored crystallization of Y, when nucleation starts in present of any solvent amounts. The influence of the solvent on the crystallizing form can be evaluated by using Hansen solubility parameters.[183] They describe the ability of a compound for molecular interactions of nonionic liquids by a dispersion force component δ_D, a hydrogen bonding force component δ_H, and a polar force component δ_P (see Figure 5.1 B, p. 88). This concept is well established and its widespread use for the prediction of miscibilities of liquids, the adsorption of pigments to surfaces, or the ability of compatibility predictions between pharmaceutical materials shows its suitability to evaluate interactions between analyte and solvent molecules, and the outcome of the crystallization experiments. In the case of ROY, the yellow colored polymorphs favor the molecular conformation with nearly perpendicular arrangements

of the thiophene and nitrophenyl ring. The probability to obtain these polymorphs is high with solvents which have a high polarity like acetonitrile or a high tendency to form hydrogen bonds as methanol does. The solvents acetone, benzonitrile, and ethyl acetate forming the polymorph R with YN as a crystalline intermediate are close to each other in the teas graph (see Figure 5.1 B, p. 88). The hydrogen bonds force component of these solvents is low. On the other hand, the dispersion interactions have higher values and the polar interactions are medium strong. The polymorph ON can arise from acetone, benzonitrile, dichloromethane, ethyl acetate, methanol, or 1-propanol. The solvents tend to have high hydrogen bond force components, medium polar and dispersion force values. The evaluation of the Hansen solubility parameters shows the crucial role of hydrogen bonds for the progress of the crystallization pathways. This issue has also been discussed in previous paracetamol studies reporting a strong correlation between the hydrogen bond strength on the torsion angle between the acetamido group and the phenyl plane. The hydrogen bond strength also affects the dynamic and rotational freedom of the methyl group. Paracetamol with its hydroxyl and acetamido group being potential proton donors and proton acceptors, respectively, can interact strongly with solvents showing a high hydrogen bonding force. These interactions directly influence the hydrogen bond strength. Therefore, changes in molecular conformation and polymorphic structure may occur.[184] This assumption is also clarified in the paracetamol crystallization studies investigated with the total X-ray scattering method and the transformed PDFs. Crystallization progress starting from liquid solution is introduced by the evaporation. The subsequently formed amorphous phase has already shown characteristics intermolecular hydrogen bonds which are typical for the correspond polymorph. The results suggest that the nature of the solvent to form hydrogen bonds can also influence the molecular arrangement of the developed amorphous phase. This kind of imprinting of the amorphous phases can push the crystallization to form one specific structure. Taking all these aspects into account, we can assume that the propensity of a solvent to form intermolecular hydrogen bonds can define local structures within in the amorphous phase. Differences in positions of the methyl group and the angle between the phenyl plane and acetamido group arise. The results also show that the crystallization of a specific polymorph can be attributed to nearest neighbor interactions and intermolecular attractive forces between solvent and analyte.

Up to this point, the macroscopic crystallization phenomena are explained with experimental results and the application of models. The theoretical calculations complement the received results by giving deeper insight into interactions on the molecular level. The

use of the MD simulation to study the crystal nucleation is challenging, as the process can take seconds to minutes. The classical MD method can only handle appearances in range of nanoseconds to microseconds. So for now, it is impossible to study the whole crystallization process from nucleation to crystal growth with this procedure. As previously discussed, the crystallization results and the PDF analysis of paracetamol indicate that initial interactions in the solutions already have impact on the pathway. The consideration of the aggregates initially appearing in the solvent solutions is accessible with the timescale of a typical MD run. This offers explanatory approaches to understand the observed crystallization phenomena.

In taking this stance, the methanol and 1-propanol molecules exhibit different molecular volumes in solution. 1-propanol molecules have larger volumes in comparison to methanol molecules. Therefore, they occupy a larger volume influencing the structure of the solution. This can be explained by the smaller solubility of paracetamol in 1-propanol. These two effects can influence the size of the occurring paracetamol clusters in the liquid solutions. Therefore, methanol enables the formation of much bigger clusters in solution. Besides the differences in cluster size, the MD simulations show further variations in the qualitative and quantitative interactions in the different liquid solutions regarding the hydrogen bonds to the neighboring nitrogen atoms and oxygen atoms of the hydroxyl groups. The paracetamol molecules interact stronger with these components of adjacent molecules in methanol than in 1-propanol. How can this affect the outcome of the crystal structure of paracetamol? In order to be able to answer this question, the crystal structure of the polymorphs have to be considered. Therefore, the Hirshfeld analysis is used to study the percentage of the bonds distribution in both polymorphs of paracetamol, where the crystal electron density is partitioned into molecular fragments.[186,187] Figure 5.2 shows the two-dimensional fingerprint plots of the Hirshfeld surface of form I and form II. Each point of the plot is determined by two variables, d_e and d_i, giving the distance of a point on a Hirshfeld surface to the nearest nucleus outside or inside the surface. The color of each point corresponds to the contribution to the surface (blue = small contribution, green = medium contribution, red = high contribution). At first glance, the plots of the structures look very similar. Both forms have strong hydrogen bonds between the carbonyl, hydroxyl, and N−H group resulting in the two characteristic lanes at very short distances. Major differences are visible regarding the so-called C−H wings. They are more distinct and shifted to shorter distances in form II, which come from the pronounced interactions between the C−H units of the ring with other C−H units or the entire π-system of neighboring molecules. This explains the dense packing of form II (1.377 g/cm^3 form

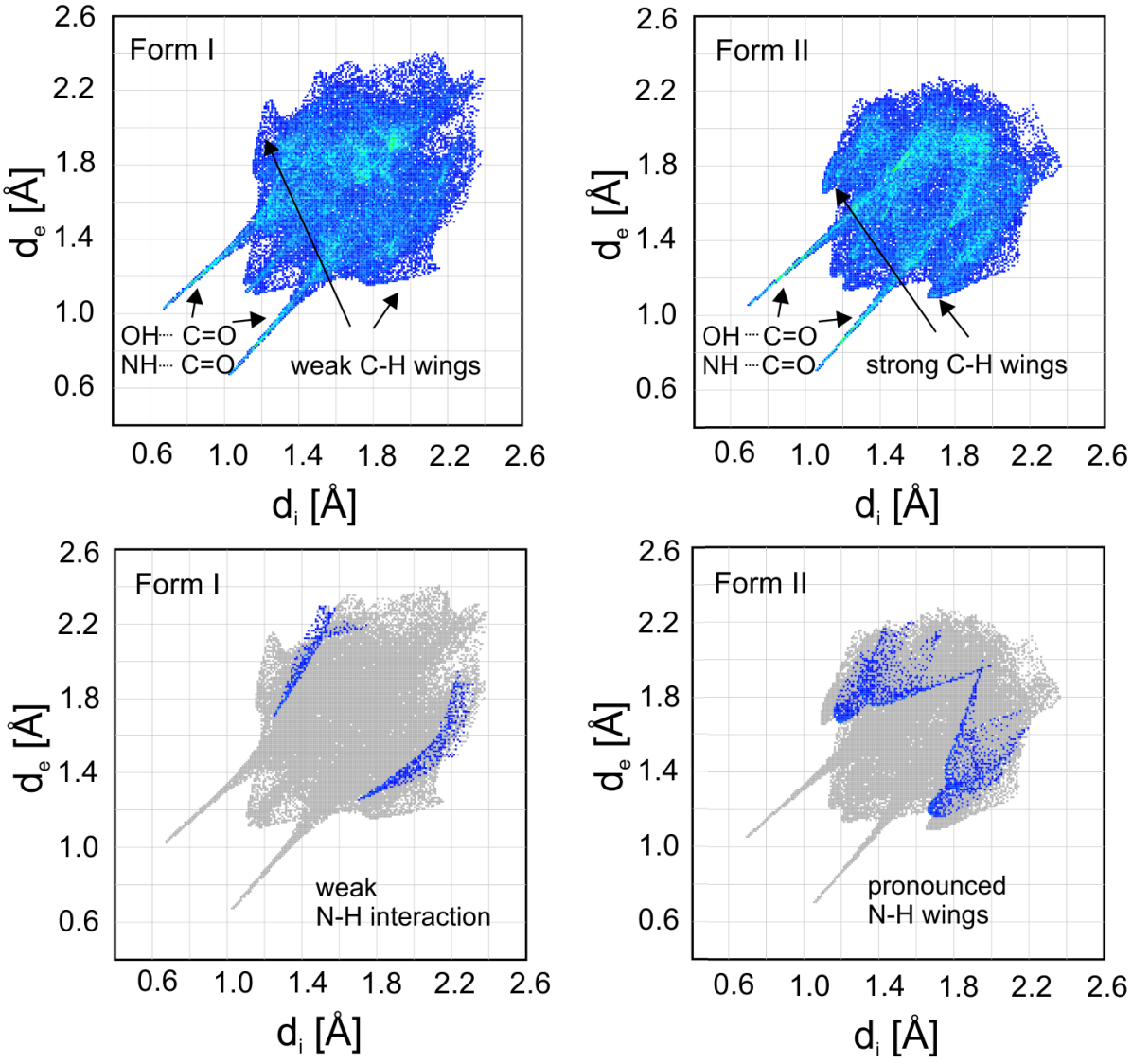

Figure 5.2: The 2D fingerprint plots of the Hirshfeld surface of the paracetamol polymorphs are shown in the upper graphics. The CrystalExplorer 3.1, the database entries HXACAN27 (form I) and HXACAN31 (form II) were used to generate the plots.[185] The two plots below emphasize the different interactions of the nitrogen atom with the rings of neighbored molecules.

II, 1.332 g/cm^3).[141] A related effect can be seen with the interaction of the N−H group. This group only shows pronounced wings in form II (see Figure 5.2, p. 91). The N−H group exhibits greater interaction with the π-system of neighboring molecules. A similar aspect could also be found in the spatial distribution functions (SDFs) of the methanolic solution (see Section 4.2.4, p. 60). The higher cluster size and the stronger interactions with the N−H and hydroxyl group of neighbors fix the neighboring molecules at two points of their functional groups. These aspects may explain why the denser form II is formed preferably from the methanol solution. In the 1-propanol solution, tiny cluster sizes and the only main interaction with the hydroxyl group with neighbors enable a greater range of motion freedom to arrange in the thermodynamically stable form I.
The MD simulations of the liquid solutions and the Hirshfeld surface analysis suggest that depending on the solvent the interactions in solutions are crucial for the outcome of the crystalline structure. This is consistent with the XRD experiments and the PDF analysis where different amorphous phases are detected depending on the choice of the solvent. That means that the imprinting of structure features already starts in the liquid solutions. The aggregation increases with the increasing concentration during the crystallization process. In this way, a preordered amorphous phase which determines the outcome crystal structure is formed.

5.2.2 Crystallization control via the concentration

The advantage of acoustic levitators as sample compartments is the possibility to monitor conveniently the crystallization processes as a function of the concentration. The evaporation of a solvent during the levitation gradually decreases the droplet's volume and, therefore, the corresponding amount of the solvent as well. Measuring the size of the droplet, the time-dependent concentration change is accessible. As the following explanations will show, the influence of the solvent and the concentration are closely linked to each other; they cannot be considered separately.

The contactless crystallization enables the observation of highly supersaturated solutions by the evaporation until the concentration reaches four and a half times of the saturation. This is only possible, if the energy barrier created by the crystal-liquid interfacial free energy is high. The height of the energy barrier is the higher, the larger the differences in local structural arrangements between the crystal and liquid phases are.[14,188] This fact hampers the process of nucleation. Additionally, foreign solid surfaces, which could reduce the contribution of the interfacial free energy, are missing in

levitation. All these aspects allow the high saturation of the solution in the droplet. To the best of my knowledge, the presented experiments of paracetamol are the first ones proceeding via a such high saturation. This supersaturated state is comparable with the amorphous phase of paracetamol.

Experiments with different initial concentrations in 1-propanol and methanol were performed with paracetamol (see Section 4.2.3, p. 57). The careful analysis of the XRD patterns shows that the liquid solutions with the different initial concentrations in 1-propanol have similar scattering maxima at 20.52° 2θ and 9.06° 2θ (see Figure 5.3 A, left, p. 96). Only minor changes are visible concerning the relative intensity of the maxima. The maximum at the lower 2θ value becomes more intense at diluted solution S = 0.1 (light blue arrow). A similar scattering pattern with the two intense curves can be found in the XRD pattern of pure 1-propanol. The strong maximum is assigned to the short-range order between the neighboring alcohol molecules, and the weak side maximum arises from the correlations between hydrogen-bonded alcohol molecules via the hydroxyl groups, which indicates chains formations between the alcohol molecules.[189] That means that the more solvent molecules are present in the solution, the more the chain motif of the solvent molecules are pronounced. Looking at the XRD patterns prior to the crystallization onset, no significant shift of the main scattering maximum is visible (see Figure 5.3 A, right, p. 96). On the other hand, the weak side maximum disappears in all cases. This is an indication that the correlation between hydrogen-bonded solvent molecules is missing, which in turn means the chain structure of the solvent molecules is lost.

The crystallization results of paracetamol show different crystallization pathways depending on the initial concentration, which is only true for the solution in methanol. In methanol, the initial concentrations influence the progress of the saturation and determine the degree of saturation which crystallizes either to form I or form II of paracetamol. At the beginning, the XRD patterns show that the initial highly concentrated solutions (S = 0.8, 1.0) have the same scattering maximum at approx. 24.15° 2θ with a pronounced scattering shoulder between 15-20° 2θ. On the other side, the diluted solution (S = 0.1) exhibits its scattering maximum at 24.55° 2θ, and the shoulder is less developed (see Figure 5.3 B, left, p. 96). The presence of the two intense curves is similar to the solution in 1-propanol and can also be explained with the same interactions. Using this information, the more pronounced side maximum at high saturated concentrations shows the interactions of chains consisted of methanol and paracetamol molecules which are connected via their hydroxyl groups. The shift of the main maximum to higher angle values and the less strong side maximum in the diluted solution suggest differences in interactions and

local structures of high and low initially concentrated solutions. The further evaporation of the methanol during the crystallization process causes a shift of the main maximum to lower angle values in all solutions. Prior to the crystallization, the maximum of the diluted solution moves to 21.45° 2θ, while the maximum of the higher concentrated solution (S = 0.8) shifts to 21.58° 2θ (see Figure 5.3 B, right, p. 96). In both cases, the weak side maxima disappeared. This could be explained by the rearrangement of the paracetamol molecules when methanol molecules evaporated from the solution and the chain structure broke. Minor differences are visible in the displacements and the width of the scattering maxima. By means of the analytical studies we know that from the diluted solution form II arises, and form I develops from the higher concentrated solution, both initiated from its amorphous phase. The analysis of the XRD patterns cannot provide a conclusive answer about the arrangement and similarities of both amorphous phases formed from methanol. When starting with saturated solution the maxima of the state prior to the crystallization is at higher angle in comparison to the previous two solutions and the side maximum is hardly visible. This is due to the fact that methanol residues are still present in the solution when crystallization starts. The experimental studies so far could not clarify, if the observed amorphous phases coming from different initial concentrations in methanol differ from each other.

Within the CNT the Ostwald's rule of stages also provides information about the relation between the supersaturation and the resulting polymorph. According to this, at a sufficiently high supersaturation the most soluble or the least stable form crystallizes first followed by the transformation to the next soluble one through a process of dissolution and crystallization. That means that at highly supersaturated state, the highest energetic form develops continuously until the concentration of the solution reaches the solubility of this form. At that point, the solution is supersaturated regarding the next stable form and the crystallization of this form is introduced. This process leads to a decrease of the solution concentration below the solubility of the first crystallized form which starts to dissolve. Further crystallization of the second form is accompanied by further dissolution of the first form. The whole crystallization and dissolution process continues until the least soluble or most stable form is achieved. The theory implies that unstable forms of a compound crystallize at higher saturations and the stable forms arise at lower saturations. Considering the concentration study results of paracetamol, this theory does not describe the observations. Depending on the initial concentration, the crystallization of the stable form I starts either at lowered supersaturation (S = 2.5-3.9) or

at very high supersaturation (S = 4.6-4.7), while the metastable form II arises at medium supersaturation (S = 4.1-4.4). In this case, not only the concentration at the onset of the crystallization has to be regarded, but also the concentration of the solution at the beginning of the process is important for the resultant crystalline structure.
The initial concentration has influence on the kinetic of the saturation process. High concentrated solutions at the beginning of the evaporation process achieve the supersaturated state or amorphous phase in less time. This is comparable with a fast freeze effect. A denser layer near the air-solution interface could emerge and introduce the nucleation. Even the theoretical calculations provide no further information for possible explanations. However, it is conceivable that the degree of saturation achieved by the evaporation can change the type and size of molecular aggregation of the solute and solvent.
From the teas plot, it is known that the hydrogen bonding force δ_H of methanol is medium strong (see Figure 5.1 B, p. 88). This allows methanol molecules to form chains consisting of fewer than ten monomers.[190] The increasing concentration during the evaporation of the solvent raises the rate and size of molecular aggregates with solute and solvent molecules. More paracetamol molecules are involved in the formation of hydrogen bonds, but also interactions of paracetamol molecules with solvent aggregates are imaginable. A network of stabilizing hydrogen bonds arises. This is related to the viscosity of the solution and the subsequent amorphous phase of paracetamol. As a result, the diffusion and molecule mobility are reduced with increasing supersaturation. At the point of the critical supersaturation, which corresponds to the amorphous phase in most cases, an energy barrier has to be overcome. Smallest impulses can induce the crystallization process. It can be assumed that the properties of the solvent influence the interactions between solute-solute and solute-solvent. As a consequence, the structural arrangements at the point of nucleation is a result of these interactions, which is a key determinant of the crystallization process. Considering that different polymorphs crystallize from these amorphous precursors, and the assumed polyamorphism of paracetamol, we can speculate that not only the nature, but also the number of present solvent molecules in a supersaturated solution triggers the formation of the crystallizing polymorph. Hendriksen and Grant studied the crystallization of paracetamol from aqueous solution focusing on the nucleation in different supersaturation. They suggested that heterogeneous nucleation occurs in low saturated solution and homogeneous nucleation in high supersaturation.[191] The choice of the concentration and, thus, the supersaturation of the crystallization is a main factor to control the initial nucleation processes and the outcome crystalline structure.

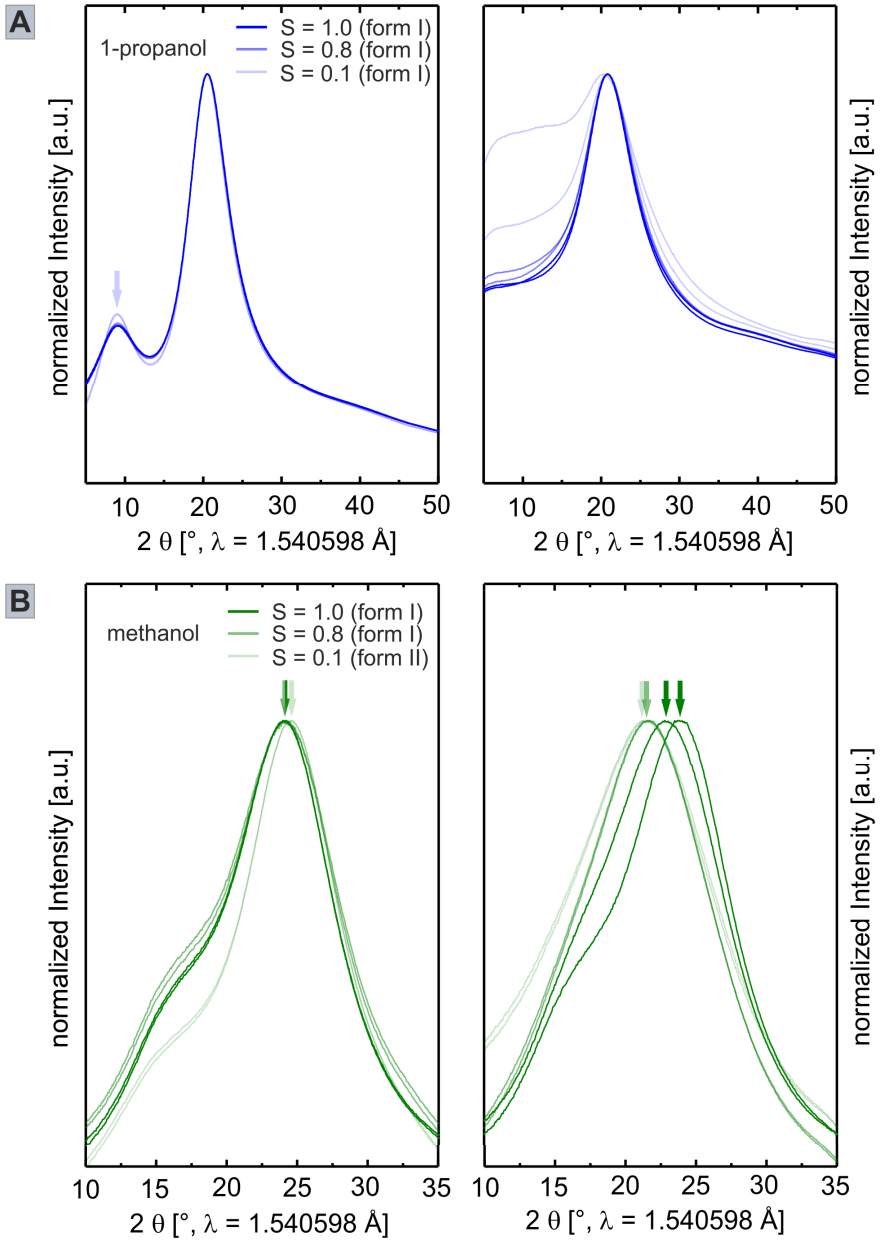

Figure 5.3: The XRD patterns of the paracetamol solution at the beginning (left) and prior to the crystallization of the crystalline forms (right) are presented. The different blue and green colored gradation shows the different saturations of the solutions. The arrows mark the scattering maxima of the XRD patterns. A) The different initial solutions in 1-propanol and the states prior to the crystallization of form I do not show significant shifts of their scattering maxima ($S = c/c_s$, $c_s = 0.59$ mol/l). B) The methanolic solutions have differences in the shifts of the maxima which are already observable and become more pronounced prior to the crystallization ($S = c/c_s$, $c_s = 1.45$ mol/l). Differences result in the formation of either form I or form II.

6 Summary and Outlook

6.1 Summary

The complex crystallization process has to be studied from different points of view to gain an overall comprehension about individual processes and the corresponding necessary conditions. The research of this work concentrates on the crystallization of organic compounds from liquid solutions. To get the targeted access of selected crystallization parameters, the crystallization experiments were performed in an undisturbed stabilized environment to avoid any possible surface influences. Under levitation it is possible to study homogeneous crystallization processes. The climatic unit of the levitator allowed the additional control of the parameters temperature and humidity around the sample. In this way, the main focus of the examinations was on the influence of the solvents and the concentration on the crystallization. Three different organic polymorphic compounds ROY, paracetamol, and indometacin as model systems were studied regarding their crystal forming processes. The use and combination of different analytical techniques supported the identification of the detailed underlying processes. The *in situ* combination of the X-ray scattering experiments with the Raman spectroscopy was a powerful technique for the screening of the crystallization. By means of the X-ray scattering the structural features of occurring crystalline forms and amorphous phases could be explained. The *in situ* Raman spectroscopy was suitable for detection of solvent amounts and the characterization of liquid solutions, amorphous intermediates, and crystalline stages. Both methods provided a deeper insight into early stages of crystallite forming processes during the evaporation of the solvents. Complementary theoretical calculations based on Molecular dynamic simulations helped interpret the experimental phenomena. This enabled us to understand the crystallization on a molecular level. Besides the structural characterization additional thermal analyses gave an insight into kinetic aspects.

The crystallization process of the model systems followed specific pathways different than those predicted by the classical nucleation theory. Initially, the solution increased its concentration introduced by the evaporation of the solvent, followed by the formation

of an amorphous phase as an intermediate which crystallized. The elimination of solid surfaces during this progress facilitated the isolation of only one polymorph, and mixtures of different polymorphs could be avoided. The solvents and their properties triggered the pathway of the crystallization processes resulting in different crystalline forms. This makes the selective crystallization of one polymorph possible. It is presumed that not only the polymorphism is a pronounced phenomenon, but also polyamorphism is a crucial appearance associated with the crystallization of organic compounds from liquid solution. The amorphous phases are intrinsic structures directly related to their crystalline products. Another aspect is the choice of the solvent and the concentration which allowed controlling the formation of a desired crystalline modification. Practical experiences have shown that higher initial concentrations near the saturation yielded selectively the thermodynamically stable form I of paracetamol. By way of contrast, very low initial concentrations provided eventually metastable form II out of an amorphous precursor phase.
The results of this work present the complexity of the crystallization process. They open new venues for studying multiple pathways for crystallization in liquid solution systems. The closer examination of the influencing factors on the crystallization process indicates the big challenge regarding targeted formation of a certain crystal structure. Nevertheless, the control of the surrounding conditions and experimental parameters allowed to gain deeper insight into the mechanisms. In this way, deriving approaches could be gained to extend the understanding of the crystallization process, which contribute to the optimization of manufacturing processes.

6.2 Outlook

The crystallization studies in this research were studied structurally and kinetically in separated experiments. The logical next step is to combine analytical methods where both aspects can be investigated simultaneously. A follow-up project has already started to implement these intentions. A prototype construction of a dynamic vapor sorption (DVS) device with adjustable solvent partial pressures and temperatures includes a video microscope, a Raman adapter, and a precision scales for detecting the weight changes. The reaction can be investigated simultaneously by recording mass changes, image acquisition, and Raman spectra.
First investigations with the DVS device have already shown promising results for kinetically studying the solvation process of indometacin from organic solvents. The isothermal

experiments with increased solvent partial pressure and the application of a model-free method enable extracting the activation energy for the solvation process. This emphasizes the possibility to gain access to energetic parameters via DVS studies.
The DVS device still provides a great potential to study the kinetic of the solvation process in a diverse manner. Different parameters such as the partial pressure, temperature, or crystal size of the starting product can be varied to get information about the kinetic from different perspectives. In combination with the microscope and Raman spectroscopy the structural changes regarding phases and morphology during the solvation process can also be studied more extensively. Additionally, the Raman spectroscopy acts as a connecting method between the *in situ* setup with the synchrotron X-ray scattering experiments and the experiments in the DVS device. Results from both setups provide a profound knowledge for crystallization processes from liquid solutions. They have a great potential for similar systems.

List of Tables

[1] Reuse with permission from T. Gnutzmann, Y. Nguyen Thi, K. Rademann, and F. Emmerling. Solvent-triggered Crystallization of Polymorphs Studied in situ. Cryst. Growth Des., 2014, 14 (12), 6445-6450. Copyright © 2014 American Chemical Society.

[2] Y. Nguyen Thi, K. Rademann, and F. Emmerling, CrystEngComm, 2015, 17, 9029-9036 - Published by The Royal Society of Chemistry.

List of Figures

[1]Reuse with permission from T. Gnutzmann, Y. Nguyen Thi, K. Rademann, and F. Emmerling. Solvent-triggered Crystallization of Polymorphs Studied in situ. Cryst. Growth Des., 2014, 14 (12), 6445-6450. Copyright © 2014 American Chemical Society.

[2]Y. Nguyen Thi, K. Rademann, and F. Emmerling, CrystEngComm, 2015, 17, 9029-9036 - Published by The Royal Society of Chemistry.

[3]T. Y. Nguyen, E. A. Roessler, K. Rademann, and F. Emmerling, „Control of Organic Polymorph Formation: Crystallization Pathways in Acoustically Levitated Droplets“, in: Zeitschrift für Kristallographie-Crystalline Materials, 232(1-3), De Gruyter, 2017, p. 17-21 , Fig. 1/Fig. 7.

Appendix

Table 6.1: The polymorphs of ROY with the corresponding structure information are presented. [192]

Polymorphs	YT04	Y	ON	OP	R	YN	ORP
Crystal system	monoclinic	monoclinic	monoclinic	monoclinic	triclinic	triclinic	orthorhombic
Crystal habit	yellow prisms	yellow prisms	orange needles	orange plates	red prisms	yellow needles	orange-red plates
Space group	$P2_1/n$	$P2_1/n$	$P2_1/c$	$P2_1/n$	$P\bar{1}$	$P\bar{1}$	Pbc
a [$\AA$]	8.2324	8.5001	3.9453	7.9760	7.4918	4.5918	13.177
b [$\AA$]	11.8173	16.413	18.685	13.319	7.7902	11.249	8.0209
c [$\AA$]	12.3121	8.5371	16.3948	11.676	11.911	12.315	22.801
α [°]	90	90	90	90	75.494	71.194	90
beta [°]	102.505	91.767	93.830	104.683	77.806	89.852	90
γ [°]	90	90	90	90	63.617	88.174	90
Volume [$\AA^3$]	1169.36	1190.5	1205.9	1199.9	598.88	601.85	2409.8
Z	4	4	4	4	2	2	8
θ_{thio}[°]	112.8	104.7	52.6	46.1	21.7	104.1	39.4
$\nu_{CN}[cm^{-1}]$	2223	2232	2223	2226	2212	2222	2217

Table 6.2: The table lists and assigns the Raman vibration modes in cm^{-1} of the individual polymorphs of ROY (υ = stretching vibration, δ = deformation vibration).

Amorphous phase	Y	YN	ON	R	Assignment
564	566	569	562	565	
684	688	690	682/696	679	
839	829	827	836	838	
1049	1041/1051	1043	1047	1044	υ(C-C phenyl ring)
1076	1075	1075	1078	1077	
1149	1149	1150	1149	1146	
1162	1162	1160	1161	1161	
1215	1196	1193	1216	1210	
1229	1228	1224	1247		
1266	1269	1263	1277	1262	
1322	1337	1327/1337	1323	1318	
1340	1357	1357	1342	1339	υ(C-NO_2)
	1379	1381	1370	1370	δ(CH_3)
1447	1445	1445	1444	1443/1455	asymmetric δ(CH_3)
1477			1486	1482	
1500	1496	1494	1507	1501	υ(C-C phenyl ring)
1552	1553	1551	1561	1546/1566	asymmetric υ(C-NO_2)
1579	1575	1577	1585	1579	υ(C-C phenyl ring)
2227	2232	2222	2223	2212	υ(C≡N)
2923	2919	2920	2920	2923	υ(C-H methyl group)

Table 6.3: The polymorphs of paracetamol with the corresponding structure features are shown. [135]

Polymorphs	Form I	Form II	Form III
Crystal system	monoclinic	orthorhombic	orthorhombic
Space group	$P2_1/a$	Pcab	$Pca2_1$
a [Å]	12.930(40)	7.406(1)	11.837(36)
b [Å]	9.400(10)	11.837(7)	8.560(25)
c [Å]	7.100(20)	17.162(3)	14.819(45)
β [°]	115.90(20)		
Volume [$Å^3$]	776.27	1504.44	1501.53
Z/Z'	4(1)	8(1)	4(2)

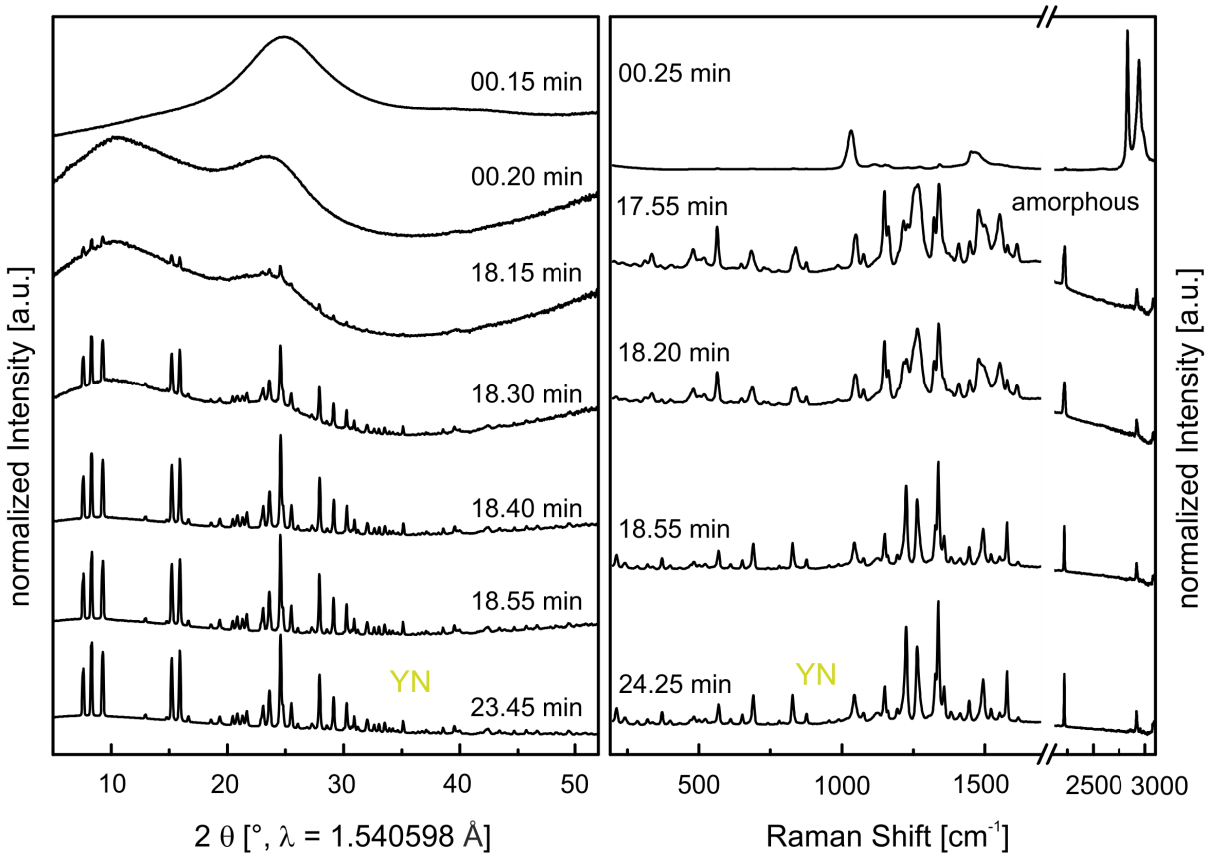

Figure 6.1: The isolation of the polymorph YN only succeeds from a methanolic solution. At the beginning, the Raman band of the C-H vibration at 2835 cm^{-1} is significant for the methanol. The intensity of this signal corresponds with the evaporation of methanol. When methanol vanishes completely, the characteristic Raman spectrum of the amorphous phase with the C≡N vibration at 2227 cm^{-1} appears. After about 18 minutes the crystallization of YN from the amorphous phase occurs and is completed within 1 minute. The C≡N vibration at 2227 cm^{-1} shifts to 2222 cm^{-1}, and reflexes in the X-ray pattern arise.

Table 6.4: The TG analysis of the indometacin-methanol solvate is shown.

run	$m_{initial}$ [mg]	m_{final} [mg]	Δm [mg]	m_{IMC} [mg]	n_{CH_3OH} [mg]	n_{IMC} [mg]	$\frac{n_{CH_3OH}}{n_{IMC}}$
1	5.285	4.848	0.437	4.848	1.3638 e^{-5}	1.355 e^{-5}	1.007
2	3.872	3.579	0.293	3.579	9.1443 e^{-6}	1.000 e^{-5}	0.914
3	2.456	2.270	0.186	2.270	5.8049 e^{-6}	6.345 e^{-6}	0.915
4	3.491	3.231	0.260	3.231	8.1144 e^{-6}	9.031 e^{-6}	0.899
5	4.976	4.589	0.387	4.589	1.2078 e^{-5}	1.283 e^{-5}	0.942
						average	0.935
						standard deviation s	0.0191
						2 s	0.0382

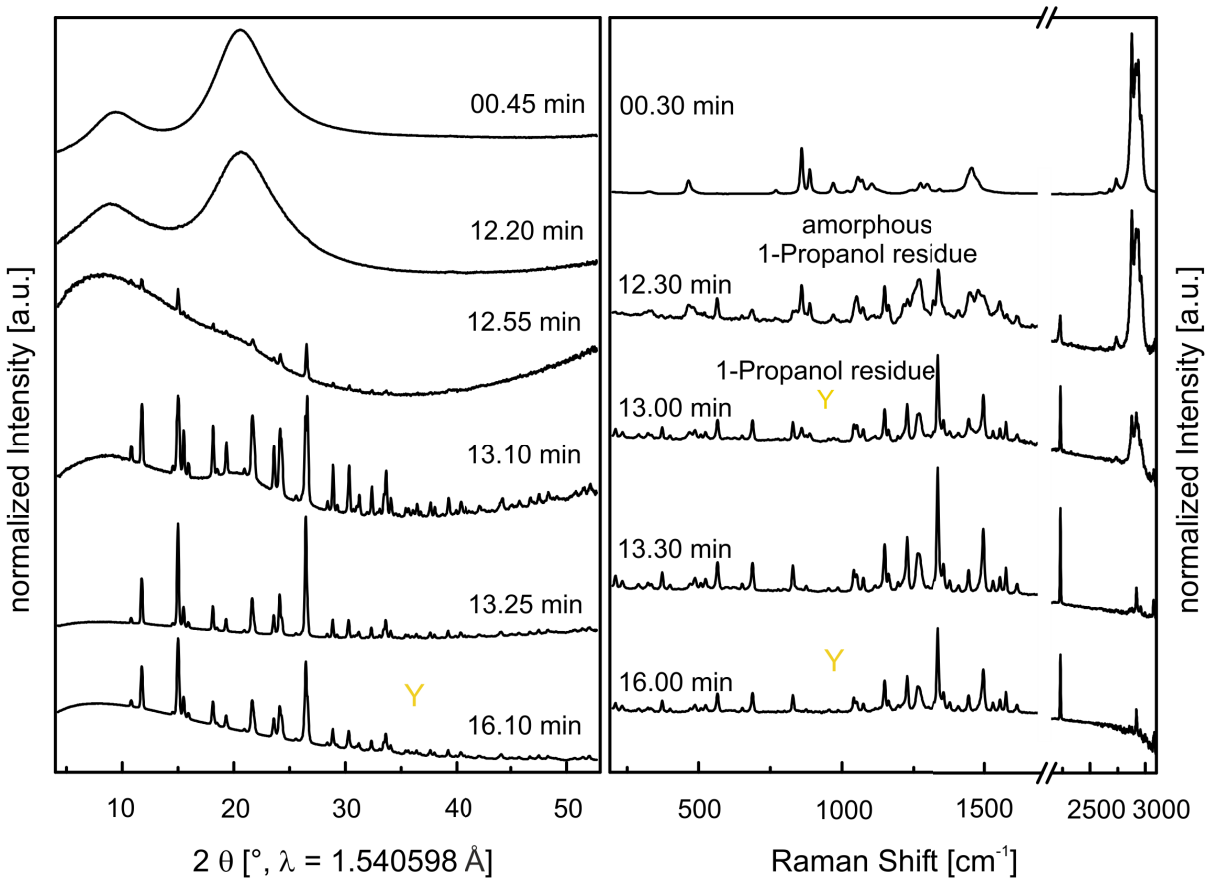

Figure 6.2: The graphic shows the crystallization of Y in present of an amorphous phase and 1-propanol residues. First, the solution has significant signals of 1-propanol at 2878 cm^{-1} and 859 cm^{-1} belonging to the methyl and C−C vibrations. The intensity of these bands decreases with the volatilization of 1-propanol leading to the formation of an amorphous phase. The crystallization of Y starts in present of 1-propanol after 13 minutes. The solvent gradually disappears through the progressive transformation to Y.

Table 6.5: The TG analysis of the indometacin-chloroform solvate is shown.

run	$m_{initial}$ [mg]	m_{final} [mg]	Δm [mg]	m_{IMC} [mg]	n_{CHCl_3} [mg]	n_{IMC} [mg]	$\frac{n_{CHCl_3}}{n_{IMC}}$
1	6.261	5.348	0.913	5.348	7.6482 e^{-6}	1.495 e^{-5}	0.512
2	7.987	6.950	1.037	6.950	8.6869 e^{-6}	1.942 e^{-5}	0.447
3	4.617	4.026	0.591	4.026	4.9508 e^{-6}	1.125 e^{-5}	0.440
4	4.247	3.666	0.581	3.666	8.8670 e^{-6}	1.025 e^{-5}	0.475
						average	0.468
						standard deviation s	0.016
						2 s	0.032

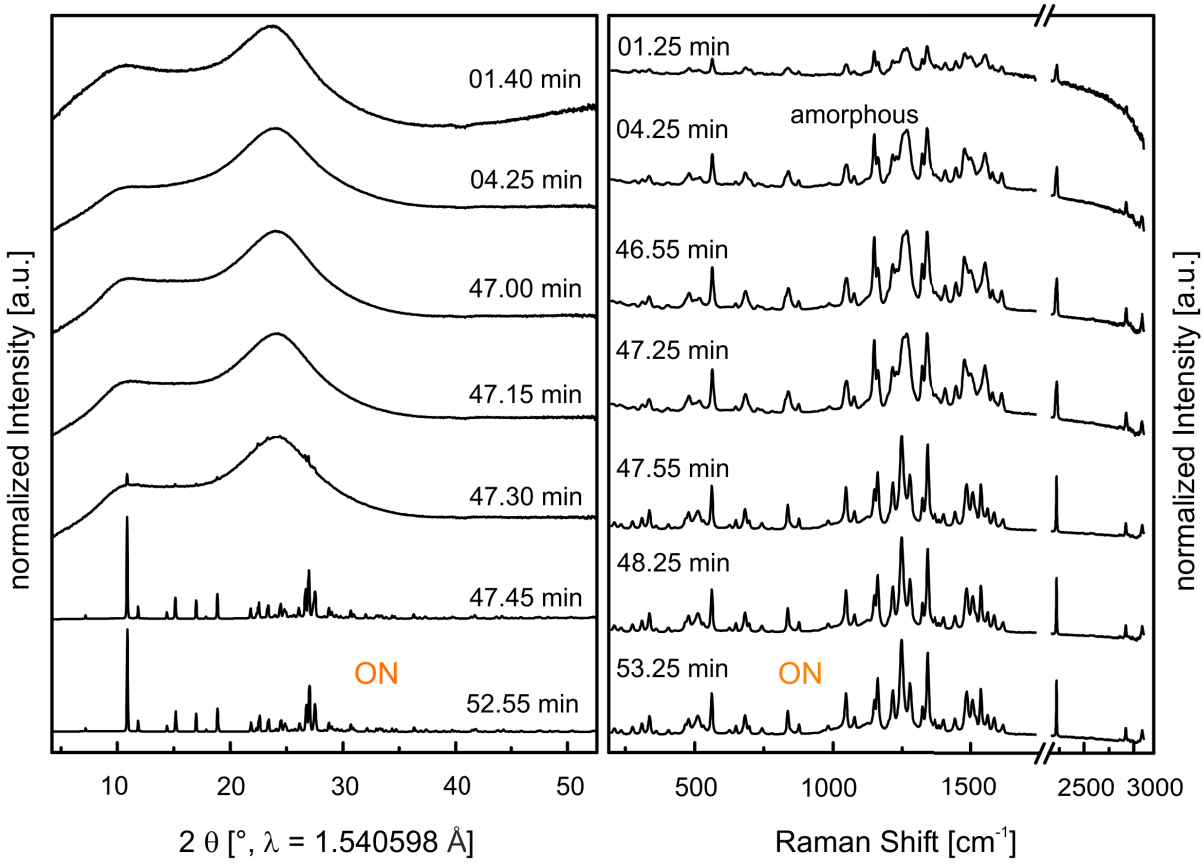

Figure 6.3: The formation of the polymorph ON starts in solution with dichloromethane, which is strongly apparent from the C−Cl and C−H stretch vibrations at 703 cm^{-1} and 2987 cm^{-1}, respectively. Dichloromethane evaporates fast because of its low boiling point and high vapor pressure. The progressive evaporation is proportional to the intensity decrease of the dichloromethane vibration modes. After 04.25 min the solvent vanishes completely and an amorphous phase with its characteristic Raman signals develops. This metastable phase remains for about 43 minutes. Crystallization is identified by the occurrence of first reflexes in the diffractogram and the shift of the C≡N vibration from 2227 cm^{-1} to 2223 cm^{-1} after 47.30 min.

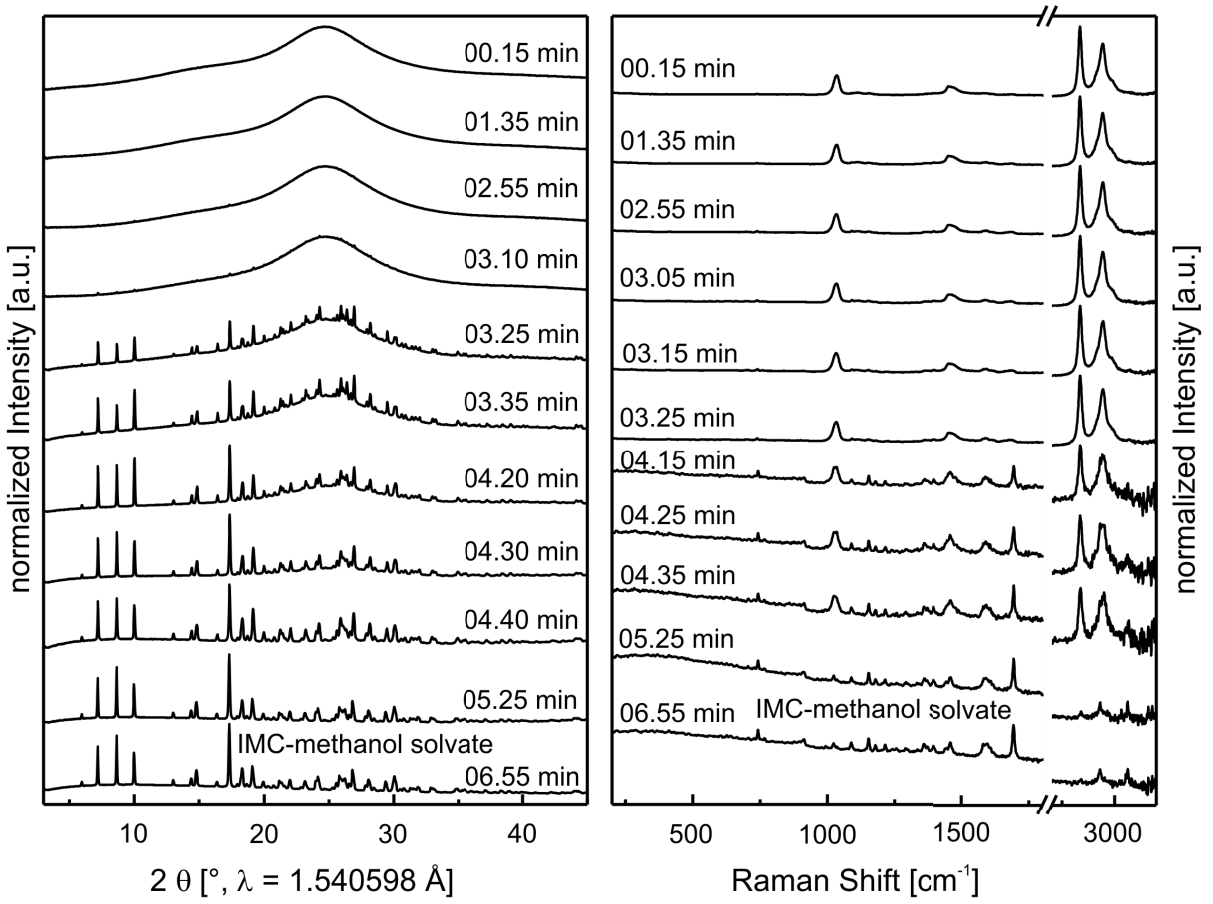

Figure 6.4: The crystallization process of the indometacin solvate with methanol was studied time-resolved with synchrotron XRD (left) and Raman spectroscopy (right).

Table 6.6: The TG analysis of the indometacin-acetone solvate is presented.

run	$m_{initial}$ [mg]	m_{final} [mg]	Δm [mg]	m_{IMC} [mg]	$n_{(CH_3)_2CO}$ [mg]	n_{IMC} [mg]	$\frac{n_{(CH_3)_2CO}}{n_{IMC}}$
1	6.307	5.870	0.437	5.870	7.5242 e^{-6}	1.641 e^{-5}	0.459
2	7.986	7.419	0.567	7.419	9.7625 e^{-6}	2.074 e^{-5}	0.471
3	6.018	5.590	0.428	5.590	7.3693 e^{-6}	1.562 e^{-5}	0.472
4	7.920	7.234	0.686	7.234	1.1811 e^{-6}	2.022 e^{-5}	0.584
5	6.476	5.973	0.503	5.973	8.6606 e^{-6}	1.669 e^{-5}	0.519
						average	0.501
						standard deviation s	0.023
						2 s	0.046

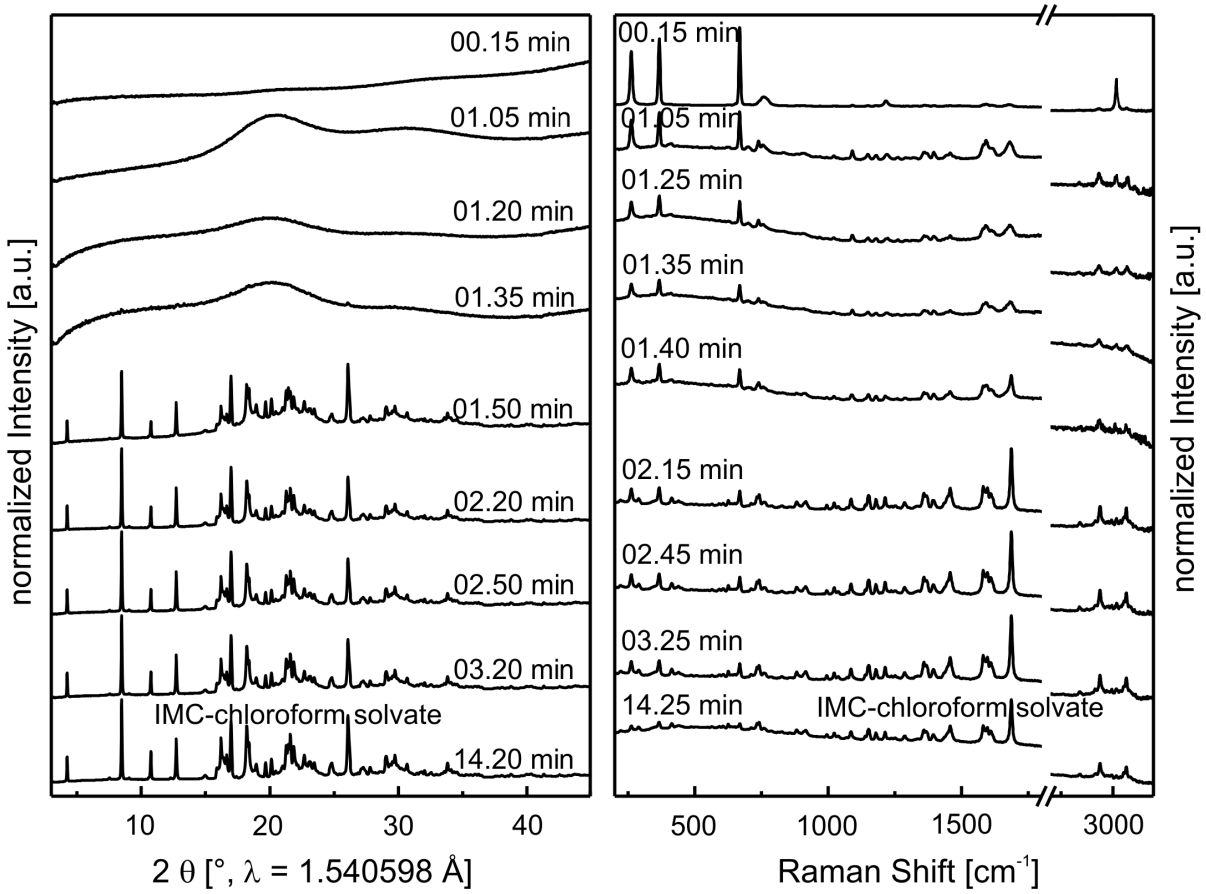

Figure 6.5: The crystallization process of the indometacin solvate with chloroform was studied time-resolved with synchrotron XRD (left) and Raman spectroscopy (right).

Table 6.7: The TG analysis of the indometacin-tetrahydrofuran solvate is presented.

run	$m_{initial}$ [mg]	m_{final} [mg]	Δm [mg]	m_{IMC} [mg]	$n_{C_4H_8O}$ [mg]	n_{IMC} [mg]	$\frac{n_{C_4H_8O}}{n_{IMC}}$
1	7.776	7.059	0.717	7.059	9.9437 e^{-6}	1.973 e^{-5}	0.504
2	7.966	7.245	0.721	7.245	9.9992 e^{-6}	2.025 e^{-5}	0.494
3	7.908	7.200	0.708	7.200	9.8189 e^{-6}	2.012 e^{-5}	0.488
4	4.813	4.393	0.420	4.393	5.8248 e^{-6}	1.228 e^{-5}	0.474
5	8.783	7.997	0.786	7.997	1.0901 e^{-5}	2.235 e^{-5}	0.488
						average	0.490
						standard deviation s	0.0048
						2 s	0.0096

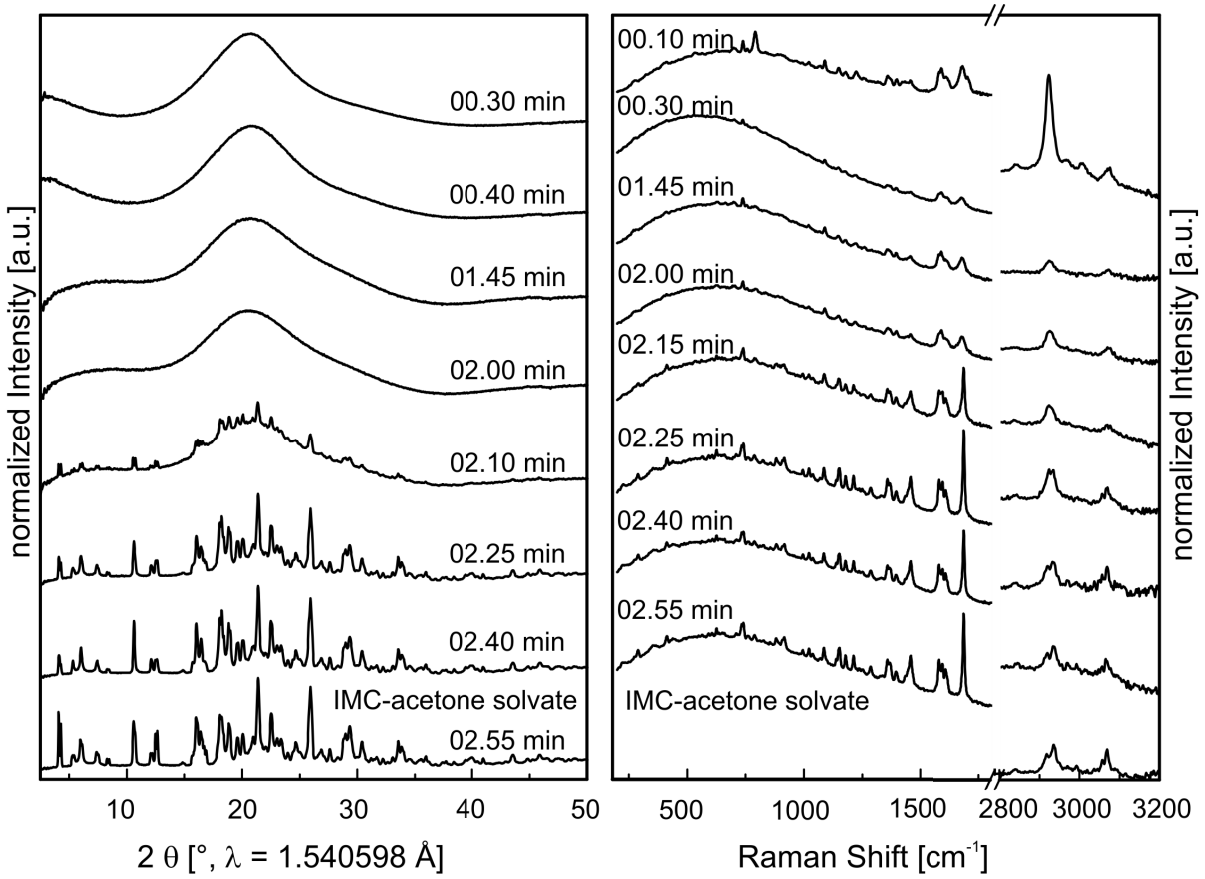

Figure 6.6: The crystallization process of the indometacin solvate with acetone was studied time-resolved with synchrotron XRD (left) and Raman spectroscopy (right).

Table 6.8: The TG analysis of the indometacin-1,4-dioxane solvate is shown.

run	$m_{initial}$ [mg]	m_{final} [mg]	Δm [mg]	m_{IMC} [mg]	$n_{C_4H_8O_2}$ [mg]	n_{IMC} [mg]	$\frac{n_{C_4H_8O_2}}{n_{IMC}}$
1	5.417	4.796	0.621	4.796	7.0484 e^{-6}	1.340 e^{-5}	0.526
2	9.530	8.442	1.088	8.442	1.2349 e^{-5}	2.360 e^{-5}	0.523
3	5.594	4.973	0.621	4.973	7.0484 e^{-6}	1.390 e^{-5}	0.507
4	7.012	6.239	0.773	6.239	8.7736 e^{-6}	1.744 e^{-5}	0.503
5	9.500	8.451	1.049	8.451	1.1906 e^{-5}	2.362 e^{-5}	0.504
						average	0.513
						standard deviation s	0.0049
						2 s	0.0098

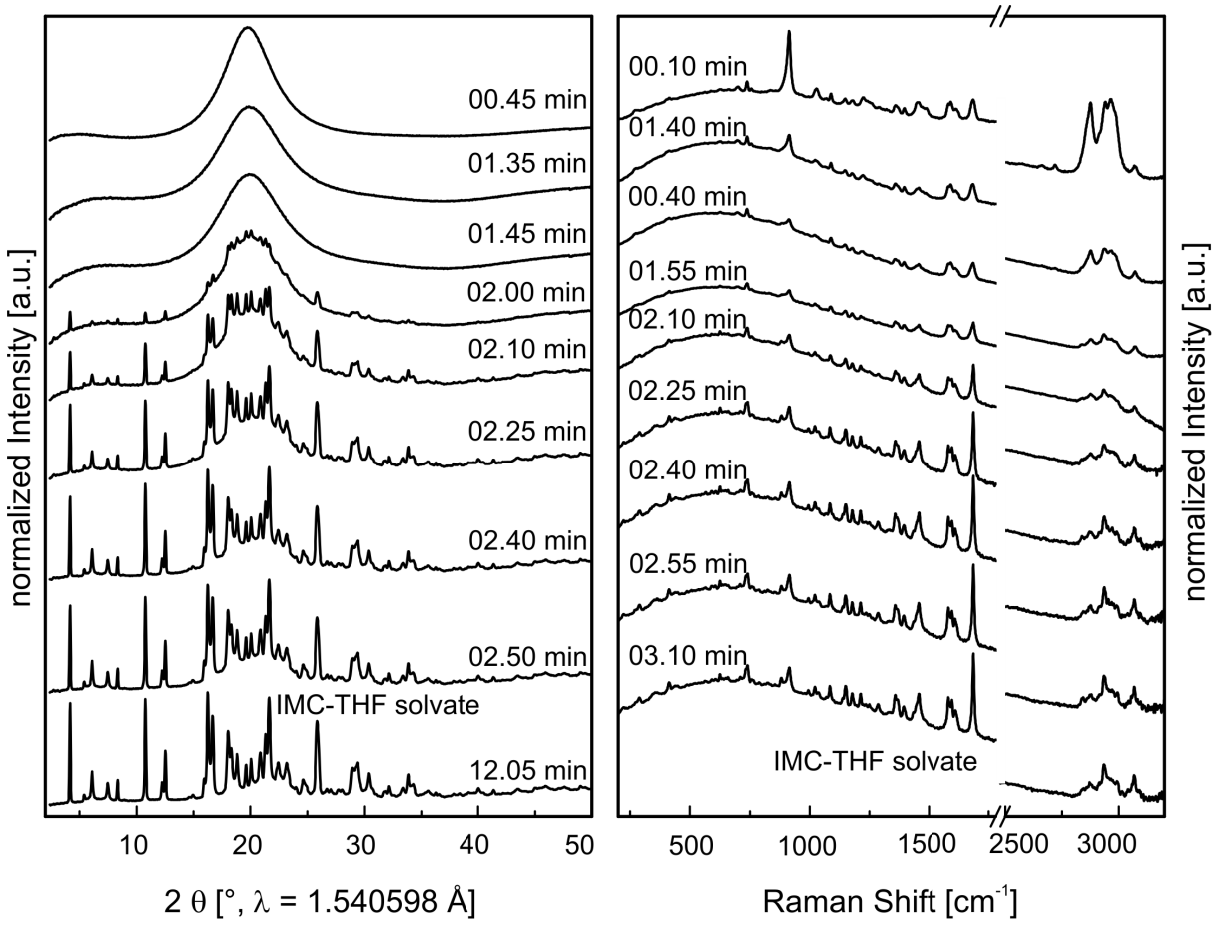

Figure 6.7: The crystallization process of the indometacin solvate with tetrahydrofuran was studied time-resolved with synchrotron XRD (left) and Raman spectroscopy (right).

Table 6.9: The TG analysis of the indometacin-1-propanol solvate is shown.

run	$m_{initial}$ [mg]	m_{final} [mg]	Δm [mg]	m_{IMC} [mg]	$n_{C_3H_8O}$ [mg]	n_{IMC} [mg]	$\frac{n_{C_3H_8O}}{n_{IMC}}$
1	3.094	2.830	0.264	2.830	4.3930 e^{-6}	7.910 e^{-6}	0.555
2	4.060	3.746	0.314	3.746	5.2251 e^{-6}	1.047 e^{-5}	0.499
3	6.568	6.013	0.555	6.013	9.2354 e^{-6}	1.681 e^{-5}	0.550
4	3.078	2.838	0.240	2.838	3.9937 e^{-6}	7.932 e^{-6}	0.503
5	4.589	4.206	0.383	4.206	6.3732 e^{-6}	1.176 e^{-5}	0.542
6	3.542	3.277	0.265	3.277	4.4097 e^{-6}	9.159 e^{-6}	0.481
						average	0.522
						standard deviation s	0.0126
						2 s	0.0252

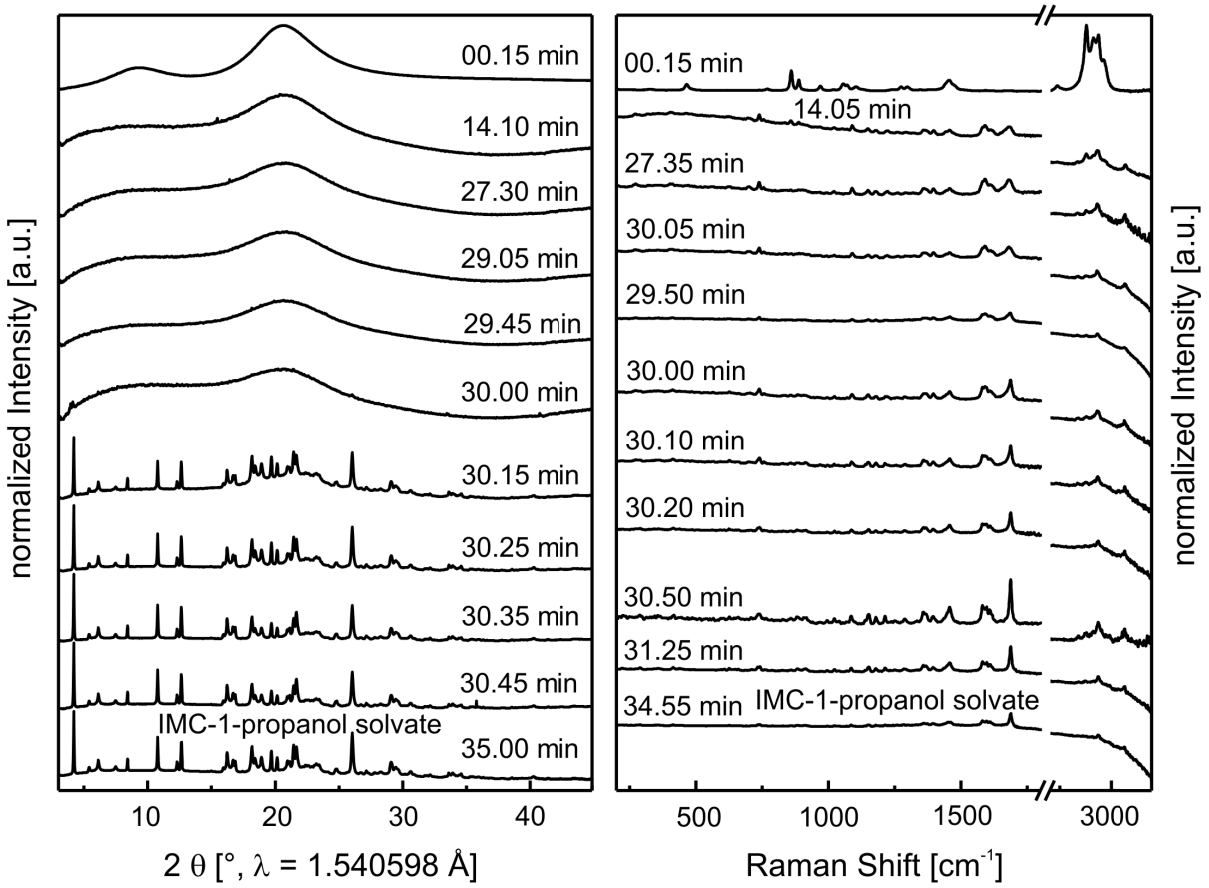

Figure 6.8: The crystallization process of the indometacin solvate with 1-propanol was studied time-resolved with synchrotron XRD (left) and Raman spectroscopy (right).

Table 6.10: The determination of the desolvation enthalpy of the indometacin-methanol by means of the DSC is shown.

run	$m_{solvate}$ [mg]	$n_{solvate}$ [mg]	m_{CH_3OH} [mg]	m_{IMC} [mg]	T_{on} [K]	T_{max} [K]	Δh [J g^{-1}] solvate	Q [J]	Δ_{desolv}h [J g^{-1}] methanol	Δ_{desolv}H [kJ mol^{-1}]
1	2.061	5.287 e^{-6}	0.169	1.892	358	361	94.399	0.1946	1148.4723	36.80
2	1.744	4.473 e^{-6}	0.143	1.600	358	361	91.959	0.1603	1118.7928	35.85
3	1.821	4.672 e^{-6}	0.150	1.672	358	361	95.838	0.1745	1165.9855	37.36
4	1.881	4.826 e^{-6}	0.155	1.727	357	361	89.783	0.1689	1092.3155	35.00
									average	36.25
									standard deviation s	0.52
									2 s	1.04

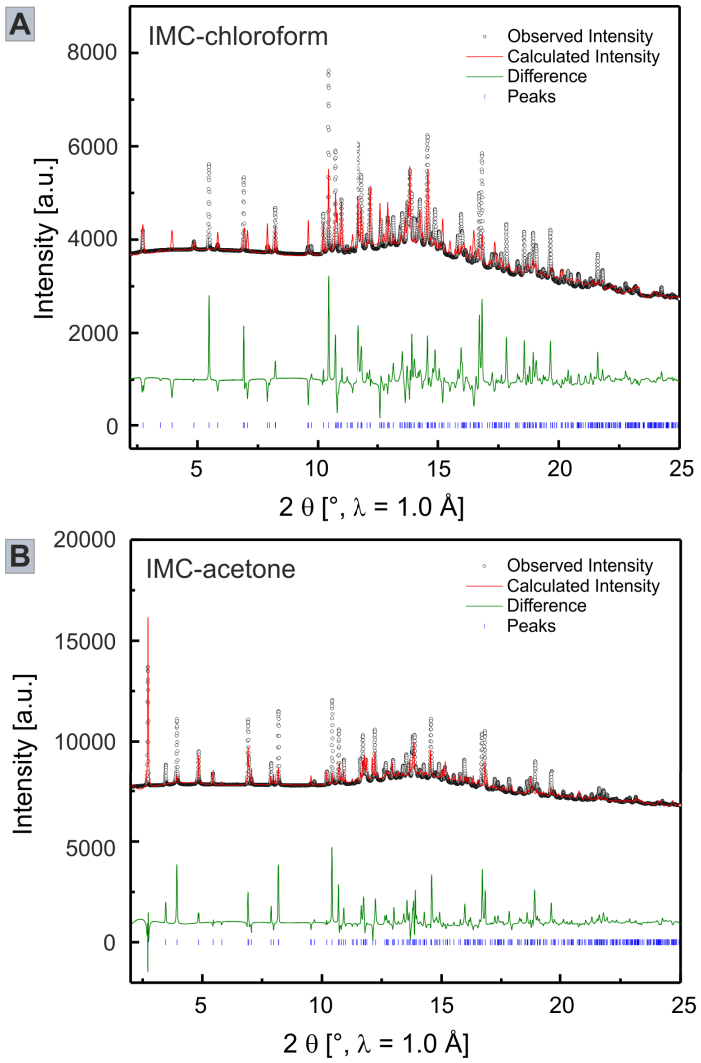

Figure 6.9: The Rietveld refinements of the indometacin-chloroform (A) and indometacin-acetone solvate structures (B) with the scattered X-ray intensity under ambient conditions are shown as a function of the diffraction angle 2θ. The observed pattern (black circles), the best Rietveld fit profile (red line), the reflection positions (blue tick marks), and the difference curve (green line) between the observed and calculated profiles are visible. The R values are $R_p = 6.04$ and $R_{wp} = 10.18$ for the indometacin-chloroform and $R_p = 7.74$ and $R_{wp} = 12.77$ the for the indometacin-acetone solvate, respectively.

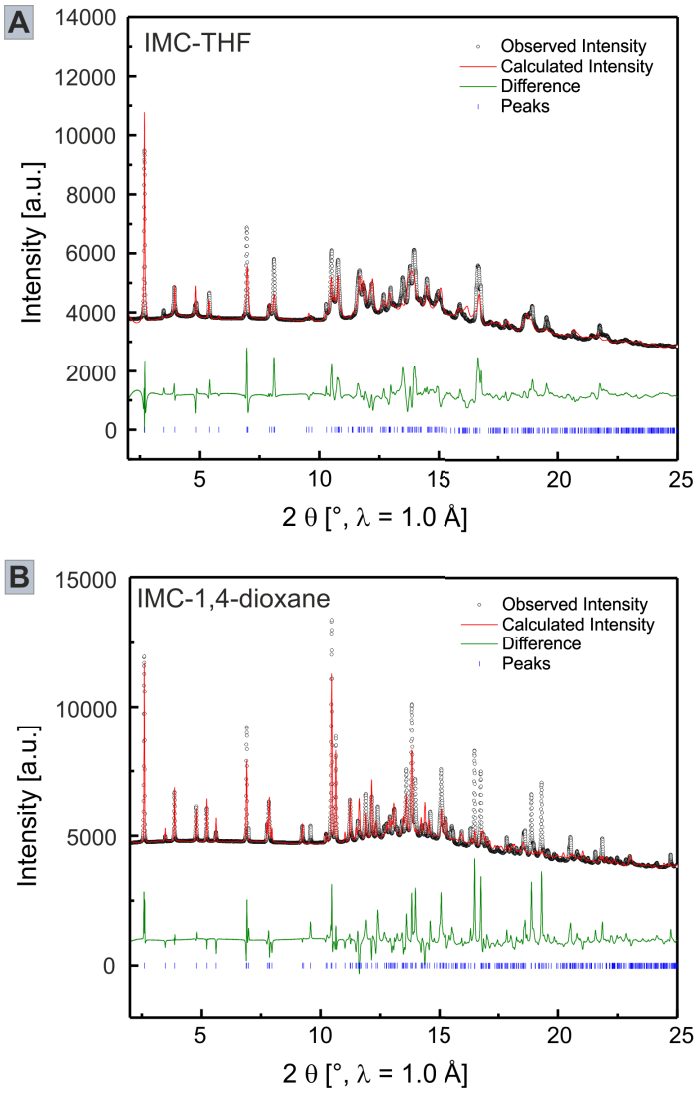

Figure 6.10: The Rietveld refinements of the indometacin-THF (A) and the indometacin-1,4-dioxane solvate structures (B) with the scattered X-ray intensity under ambient conditions are shown as a function of the diffraction angle 2θ. The observed pattern (black circles), the best Rietveld fit profile (red line), the reflection positions (blue tick marks), and the difference curve (green line) between the observed and calculated profiles are visible. The R values are $R_p = 5.96$ and $R_{wp} = 9.02$ for the indometacin-THF and $R_p = 8.83$ and $R_{wp} = 13.90$ the for indometacin-1,4-dioxane solvate, respectively.

Bibliography

[1] I. Sunagawa. Natural Crystallization. *Journal of Crystal Growth*, 42:214–223, 1977.

[2] D. Gebauer, M. Kellermeier, J. D. Gale, L. Bergstrom, and H. Cölfen. Pre-nucleation Clusters as Solute Precursors in Crystallisation. *Chemical Society Reviews*, 43(7): 2348–2371, 2014.

[3] C. Sun, D. Xu, and D. Xue. Direct in situ ATR-IR Spectroscopy of Structural Dynamics of $NH_4H_2PO_4$ in Aqueous Solution. *Crystengcomm*, 15(38):7783–7791, 2013.

[4] J. W. Gibbs. On the Equilibrium of Heterogeneous Substances. *Transactions of the Connecticut Academy of Arts and Sciences*, 3:108–248, 1876.

[5] M. Volmer and A. Weber. Germ-Formation in Oversaturated Figures. *Zeitschrift für physikalische Chemie*, 119:277–301, 1925.

[6] R. Becker and W. Doering. Kinetische Behandlung der Keimbildung in übersättigten Dämpfen. *Annalen Der Physik*, 416(8):719–752, 1935.

[7] J. Frenkel. A Gerneral Theory of Heterophase Fluctuations and Pretransition Phenomena. *Journal of Chemical Physics*, 7(7):538–547, 1939.

[8] D. Kashchiev. *Nucleation: Basic theory with applications*. Butterworth-Heinemann, Oxford, 2000.

[9] P. Hartman and W. G. Perdok. On the Relations between Structure and Morphology of Crystals. *Acta Crystallographica*, 8(1):49–52, 1955.

[10] P. Hartman and W. G. Perdok. On the Relations between Structure and Morphology of Crystals. *Acta Crystallographica*, 8(9):521–524, 1955.

[11] P. Hartman and W. G. Perdok. On the Relations between Structure and Morphology of Crystals. *Acta Crystallographica*, 8(9):525–529, 1955.

[12] W. K. Burton, N. Cabrera, and F. C. Frank. The Growth of Crystals and the Equilibrium Structure of their Surfaces. *Philosophical Transactions of the Royal Society A*, 243:299–358, 1951.

[13] A. W. Vere. *Crystal growth: principles and progress.* Plenum Press, New York, 1987.

[14] K. F. Kelton, G. W. Lee, A. K. Gangopadhyay, R. W. Hyers, T. J. Rathz, J. R. Rogers, M. B. Robinson, and D. S. Robinson. First X-ray Scattering Studies on Electrostatically Levitated Metallic Lliquid: Demonstrated Influence of Local Icosahedral Order on the Nucleation Barrier. *Physical Review Letters*, 90:195504, 2003.

[15] X. Y. Liu. Heterogeneous Nucleation or Homegeneous Nucleation. *Journal of Chemical Physics*, 112(22):9949–9955, 2000.

[16] J. Baumgartner, A. Dey, P. H. H. Bomans, C. Le Coadou, P. Fratzl, N. A. J. M. Sommerdijk, and D. Faivre. Nucleation and Growth of Magnetite from Solution. *Nature Materials*, 12(4):310–314, 2013.

[17] H. Y. Yoshikawa, Y. Hosokawa, and H. Masuhara. Spatial Control of Urea Crystal Growth by Focused Femtosecond Laser Irradiation. *Crystal Growth & Design*, 6(1): 302–305, 2006.

[18] B. C. Knott, V. Molinero, M. F. Doherty, and B. Peters. Homogeneous Nucleation of Methane Hydrates: Unrealistic under Realistic Conditions. *Journal of the American Chemical Society*, 134(48):19544–19547, 2012.

[19] E. Sanz, C. Vega, J. R. Espinosa, R. Caballero-Bernal, J. L. F. Abascal, and C. Valeriani. Homogeneous Ice Nucleation at Moderate Supercooling from Molecular Simulation. *Journal of the American Chemical Society*, 135(40):15008–15017, 2013.

[20] A. Navrotsky. *Proceedings of the National Academy of Sciences U. S. A.*, 101: 12096–12101, 2004.

[21] W. J. Habraken, J. Tao, L. J. Brylka, H. Friedrich, L. Bertinetti, A. S. Schenk, A. Verch, V. Dmitrovic, P. H. H. Bomans, P. M. Frederik, J. Laven, P. van der Schoot, B. Aichmayer, G. de With, J. J. De Yoreo, and N. A. J. M. Sommerdijk. Ion-association Complexes Unite Classical and Non-classical Theories for the Biomimetric Nucleation of Calcium Phosphate. *Nature Communications*, 4:1507, 2013.

[22] E. Beniash, R. A. Metzler, R. S. K. Lam, and P. U. P. A. Gilbert. Transient Amorphous Calcium Phosphate in Forming Enamel. *Journal of Structural Biology*, 166(2):133–143, 2009.

[23] L. A. Gower and D. J. Odom. Deposition of Calcium Carbonate Films by a Polymer-induced Liquid-precursor (PILP) Process. *Journal of Crystal Growth*, 210(4):719–734, 2000.

[24] D. Li, M. H. Nielsen, J. R. I. Lee, C. Frandsen, J. F. Banfield, and J. J. De Yoreo. Direction-specific Interaction Control Crystal Growth by Oriented Attachment. *Science*, 336(6084):1014–1018, 2012.

[25] R. Demichelis, P. Raiteri, J. D. Gale, D. Quigley, and D. Gebauer. Stable Prenucleation Mineral Clusters Are Liquid-like Ionic Polymers. *Nature Communications*, 2:590, 2011.

[26] O. Galkin, K. Chen, R. L. Nagel, R. E. Hirsch, and P. G. Vekilov. Liquid-Liquid Separation in Solution of Normal and Sickle Cell Hemoglobin. *Proceedings of the National Academy of Sciences of the United States of America*, 99(13):8479–8483, 2002.

[27] J. W. Cahn and J. E. Hilliard. Free Energy of a Nonuniform System. 3.Nucleation in a 2-Component Incompressible Fluid. *Journal of Chemical Physics*, 31(3):688–699, 1959.

[28] L. A. Gower and D. A. Tirrell. Calcium Carbonate Films and Helices Grown in Solution of Poly(aspartate). *Journal of Crystal Growth*, 191:154–160, 1998.

[29] S. E. Wolf, J. Leiterer, M. Kappl, F. Emmerling, and W. Tremel. Early Homogenous Amorphous Precursor Stages of Calcium Carbonate and Subsequent Crystal Growth in Levitated Droplets. *Journal of the American Chemical Society*, 130(37):12342–12347, 2008.

[30] S. E. Wolf, L. Mueller, R. Barrea, C. J. Kampf, J. Leiterer, U. Panne, T. Hoffmann, F. Emmerling, and W. Tremel. Carbonate-coordinated Metal Complexes Precede the Formation of Liquid Amorphous Mineral Emulsions of Divalent Metal Carbonates. *Nanoscale*, 3(3):1158–1165, 2011.

[31] M. Faatz, F. Grohn, and G. Wegner. Amorphous Calcium Carbonate: Synthesis and Potential Intermediate in Biomineralization. *Advanced Materials*, 16(12):996–1000, 2004.

[32] D. Gebauer and H. Cölfen. Prenucleation Clusters and Non-classical Nucleation. *Nano Today*, 6(6):564–584, 2011.

[33] J. J. De Yoreo, P. U. P. A. Gilbert, N. A. J. M. Sommerdijk, R. L. Penn, S. Whitelam, D. Jöster, H. Zhang, J. D. Rimer, A. Navrotsky, J. F. Banfield, A. F. Wallace, F. M. Michel, F. C. Meldrum, H. Cölfen, and P. M. Dove. Crystallization by Particle Attachment in Synthetic, Biogenic, and Geologic Environments. *Science*, 349: aaa6760, 2015.

[34] R. L. Penn and J. F. Banfield. Imperfect Oriented Attachment: Dislocation Generation in Defect-free Nanocrystals. *Science*, 281:969–971, 1998.

[35] K. K. Sand, J. D. Rodriguez-Blanco, E. Makovicky, L. G. Benning, and S. L. S. Stipp. Crystallization of CaO_3 in Water-alcohol Mixtures: Spherulitic Growth, Polymorph Stabilization, and Morphology Change. *Crystal Growth & Design*, 12: 842–853, 2012.

[36] M. H. Nielsen, S. Aloni, and J. J. De Yoreo. In situ TEM Imaging of CaO_3 Nucleation Reveals Coexistence of Direct and Indirect Pathways. *Science*, 345:1158–1162, 2014.

[37] A. I. Lupulescu and J. D. Rimer. In situ Imaging of Silicate-1 Surface Growth Reveals the Mechanism of Crystallization. *Science*, 344(6185):729–732, 2014.

[38] P. W. Voorhees. The Theory of Ostwald Ripening. *Journal of Statistical Physics*, 38(1):231–252, 1985.

[39] F. Wöhler and J. Liebig. Untersuchungen über das Radikal der Benzoesäure. *Annalen der Pharmacie*, 3(3):249–282, 1832.

[40] J. Thun, L. Seyfarth, J. Senker, Dinnebier R. E., and J. Breu. Polymorphism in Benzamide: Solving a 175-Year-Old Riddle. *Angewandte Chemie*, 46(35):6729–6731, 2007.

[41] A. Gavezzotti and G. Filippini. Polymorphic Forms of Organic-Crystals at Room Conditions - Thermodynamic and Structural Implications. *Journal of the American Chemical Society*, 117(49):12299–12305, 1995.

[42] T. L. Threlfall. Analysis of Organic Polymorphs - A Review. *Analyst*, 120:2436–2460, 1995.

[43] J.-P. Brog, C.-L. Chanez, A. Crochet, and K. M. Fromm. Polymorphism, What It Is and How to Identify It: A Systematic Review. *RSC Advances*, 3:16905–16931, 2013.

[44] W. Ostwald. Studien über die Bildung und Umwandlung fester Körper. 1. Abhandlung: Übersättigung und Überkaltung. *Zeitschrift Für Physikalische Chemie*, 22: 289–330, 1897.

[45] J. Bauer, S. Spanton, R. Henry, J. Quick, W. Dziki, W. Porter, and J. Morris. Ritonavir: An Extraordinary Example of Conformational Polymorphism. *Pharmaceutical Research*, 18(6):859–866, 2001.

[46] P. H. Poole, T. Grande, F. Sciortino, H. E. Stanley, and C. A. Angell. Amorphous Polymorphism. *Computational Materials Science*, 4(4):373–382, 1995.

[47] T. Loerting, V. V. Brazhkin, and T. Morishita. Multiple Amorphous-amorphous Transitions. *Advances in Chemical Physics*, 143:29–82, 2009.

[48] J. Wiedersich, A. Kudlik, J. Gottwald, G. Benini, I. Roggatz, and E. Rossler. On Polyamorphism of Triphenyl Phosphite. *Journal of Physical Chemistry B*, 101(30): 5800–5803, 1997.

[49] B. C. Hancock, E. Y. Shalaev, and S. L. Shamblin. Polyamorphism: A Pharmaceutical Science Perspective. *Journal of Pharmacy and Pharmacology*, 54(8):1151–1152, 2002.

[50] M. M. Koza, B. Geil, K. Winkel, C. Kohler, F. Czeschka, M. Scheuermann, H. Schober, and T. Hansen. Nature of Amorphous Polymorphism of Water. *Physical Review Letters*, 94(12), 2005.

[51] R. J. Hemley, J. Badro, and D. M. Teter. Polymorphism in Crystalline and Amorphous Silica at High Pressures. *Physics Meets Mineralogy, Cambride University Press*, pages 173–204, 2000.

[52] J. H. E. Cartwright, A. G. Checa, J. D. Gale, D. Gebauer, and C. I. Sainz-Diaz. Calcium Carbonate Polyamorphism and Its Role in Biomineralization: How Many Amorphous Calcium Carbonates Are There? *Angewandte Chemie-International Edition*, 51(48):11960–11970, 2012.

[53] X. Gang and C. L. Chien. Polymorphism of Amorphous Pure Iron. *Journal of Applied Physics*, 61(8):3246–3248, 1987.

[54] K. Winkel, W. Hage, T. Loerting, S. L. Price, and E. Mayer. Carbonic Acid: From Polyamorphism to Polymorphism. *Journal of the American Chemical Society*, 129 (45):13863–13871, 2007.

[55] H. G. Brittain. Polymorphism and Solvatomorphism 2010. *Journal of Pharmaceutical Sciences*, 101(2):464–484, 2012.

[56] W. C. McCrone. *Physics and Chemistry of the Organic Solid State*, volume 2, pages 725-767. Interscience, London, 1965.

[57] T. Morita. Miniature Piezoelectric Motors. *Sensors and Actuators A Physical*, 103: 291–300, 2003.

[58] T. Amano, Y. Koike, S. Nakamura, K. Ueha, and Y. Hashimoto. A Multi-Transducer Near Field Acoustic Levitation System for Noncontact Transportation of Large-sized Planar Objects. *Japanese Journal of Applied Physics*, 39:2982–2985, 2000.

[59] S. Santesson and S. Nilsson. Airborne Chemistry: Levitation in Chemical Analysis. *Analytical and Bioanalytical Chemistry*, 378(7):1704–1709, 2004.

[60] F. Priego-Capote and L. de Castro. Ultrasound-assisted Levitation: Lab-on-a-drop. *Trends in Analytical Chemistry*, 25(9):856–867, 2006.

[61] A. Scheeline and R. L. Behrens. Potential of Levitated Drops to Serve as Microreactors for Biophyical Measurements. *Biophysical Chemistry*, 165:1–12, 2012.

[62] M. C. Schlegel, K. J. Wenzel, A. Sarfraz, U. Panne, and F. Emmerling. A Wall-free Climate Unit for Acoustic Levitators. *Review of Scientific Instruments*, 83(5): 055101, 2012.

[63] E. G. Lierke. Akustische Positionierung-Ein umfassender Überblick über Grundlagen und Anwendungen. *Acustica*, 82:220–237, 1996.

[64] J. Leiterer, W. Leitenberger, F. Emmerling, A. F. Thünemann, and U. Panne. The Use of an Acoustic Levitator to Follow Crystallization in Small Droplets by Energy-dispersive X-ray Diffraction. *Journal of Applied Crystallography*, 39:771–773, 2006.

[65] J. Leiterer, F. Delissen, F. Emmerling, A. F. Thünemann, and U. Panne. Structure Analysis Using Acoustically Levitated Droplets. *Analytical and Bioanalytical Chemistry*, 391(4):1221–1228, 2008.

[66] U. Bentrup, J. Radnik, U. Armbruster, A. Martin, J. Leiterer, F. Emmerling, and A. Brückner. Linking Simultaneous in situ WAXS/SAXS/Raman with Raman/ATR/UV-VIS Spectroscopy: Comprehensive Insight into the Synthesis of Molybdate Catalyst Precursors. *Topics in Catalysis*, 52(10):1350–1359, 2009.

[67] M. Klimakow, J. Leiterer, J. Kneipp, E. Rössler, U. Panne, K. Rademann, and F. Emmerling. Combined Synchrotron XRD/Raman Measurements: In situ Identification of Polymorphic Transitions during Crystallization Processes. *Langmuir*, 26 (13):11233–11237, 2010.

[68] J. Polte, T. T. Ahner, F. Delissen, S. Sokolov, F. Emmerling, A. F. Thünemann, and R. Krähnert. Mechanism of Gold Nanoparticle Formation in the Classical Citrate Synthesis Method Derived from Coupled in situ XANES and SAXS Evaluation. *Journal of the American Chemical Society*, 132(4):1296–1301, 2010.

[69] J. Radnik, U. Bentrup, J. Leiterer, A. Brückner, and F. Emmerling. Levitated Droplets as Model System for Spray Drying of Complex Oxide: A Simultaneous in situ X-ray Diffraction/Raman Study. *Chemistry of Materials*, 23(24):5425–5431, 2011.

[70] A. Sarfraz, M. C. Schlegel, J. Wright, and F. Emmerling. Advanced Gas Hydrate Studies at Ambient Conditions Using Suspended Droplets. *Chemical Communications*, 47(33):9369–9371, 2011.

[71] M. C. Schlegel, A. Sarfraz, U. Müller, U. Panne, and F. Emmerling. First Seconds in a Building's Life-in situ Synchrotron X-ray Diffraction Study of Cement Hydration on the Millisecond Timescale. *Angewandte Chemie International Edition*, 51(20): 4993–4996, 2012.

[72] M. Raju, A. C. T. van Duin, and K. A. Fichthorn. Mechanism of Oriented Attachment of TiO_2 Nanocrystals in Vacuum and Humid Environments: Reactive Molecular Dynamics. *Nano Letters*, 14(4):1836–1842, 2014.

[73] L. A. Stevens, K. P. Götz, A. Fonari, Y. Shu, R. M. Williamson, J.-L. Brédas, V. Coropceanu, O. D. Jurchescu, and G. E. Collis. Temperature-mediated Polymor-

phism in Molecular Crystals: The Impact on Crystal Packing and Charge Transport. *Chemistry of Materials*, 27:112–118, 2015.

[74] A. M. Triggle, E. Shefter, and D. J. Triggle. Crystal Structures of Calcium Channel Antagonists: 2,6-Dimethyl-3,5-dicarbomethoxy-4-[2-nitro, 3-cyano, 4-(dimethylamino), and 2,3,4,5,6-pentafluorophenyl]-1,4-dihydropyridine. *Journal of Medicinal Chemistry*, 23(12):1442–1445, 1980.

[75] E. Gunn, I. A. Guzei, T. Cai, and L. Yu. Polymorphism of Nifedipine: Crystal Structure and Reversible Transition of the Metastable Beta Polymorph. *Crystal Growth & Design*, 12(4):2037–2043, 2012.

[76] M. Bortolotti, I. Lonardelli, and G. Pepponi. Determination of the Crystal Structure of Nifedipine Form C by Synchrotron Powder Diffraction. *Acta Crystallographica Section B-Structural Science*, 67:357–364, 2011.

[77] A. Dey, P. H. H. Bomans, F. A. Müller, J. Will, P. M. Frederik, G. de With, and N. A. J. M. Sommerdijk. The Role of Prenucleation Clusters in Surface-induced Calcium Phosphate Crystallization. *Nature Materials*, 9(12):1010–1014, 2010.

[78] W. Friedrich, P. Knipping, and M. Laue. Interference Appearances in X-rays. *Annalen der Physik*, 41(10):971–988, 1913.

[79] W. H. Bragg and W. L. Bragg. The Reflection of X-rays by Crystals. *Proceedings of the Royal Society of London A*, 88(605):428–438, 1913.

[80] F. Zernike and J. A. Prins. Die Beugung von Röntgenstrahlen in Flüssigkeiten als Effekt der Molekülanordnung. *Zeitschrift für Physik A Hadrons and Nuclei*, 41(2): 184–194, 1927.

[81] T. Egami and S. J. L. Billinge. *Underneath the Bragg Peaks: Structural Analysis of Complex Materials*, volume 7. Pergamon Materials Series, 2003.

[82] H. Hertz. Die Kräfte elektrischer Schwingungen, behandelt nach der Maxwell'schen Theorie. *Annalen der Physik*, 272:1–22, 1889.

[83] D. Iwanenko and I. Pomeranchuk. On the Maximal Energy Attainable in a Betatron. *Physical Review*, 65(11/12):343–343, 1944.

[84] L. Arzimovitch and I. Pomeranchuk. The Radiation of Fast Electrons in the Magnetic Field. *Zhurnal Eksperimentalnoi i Teoreticheskoi Fiziki*, 16(5):379–390, 1946.

[85] G. D. Preston. The Crystal Stucture of alpha-Manganese. *The London, Edinburgh, and Dublin Philosophical Magazine and Journal of Science*, 5(33):1198–1206, 1928.

[86] G. D. Preston. The Crystal Structure of beta-Manganese. *The London, Edinburgh, and Dublin Philosophical Magazine and Journal of Science*, 5(33):1207–1225, 1928.

[87] A. J. King and G. L. Clark. The Crystal Structure of Barium. *Journal of the American Chemical Society*, 51(6):1709–1711, 1929.

[88] M. H. Preston, M. Jr. Edward, and F. C. Blake. The Atomic Arrangement in the Crystal of Orthorhombic Iodine. *Journal of the American Chemical Society*, 50(6): 1583–1600, 1928.

[89] J. D. Bernal, D. M. Crowfoot, R. C. Evans, and A. F. Wells. Crystallography. (1934-1935). *Annual Reports on the Progress of Chemistry*, 32:181–242, 1935.

[90] D. Crowfoot Hodgkin. The X-ray Analysis of Complicated Molecules. *Science*, 150 (3699):979–988, 1965.

[91] J. D. Watson and F. H. C. Crick. Molecular Structure of Nucleic Acids. *Nature*, 171:737–738, 1953.

[92] B. E. Warren, H. Krutter, and O. Morningstar. Fourier Analysis of X-ray Patterns of Vitreous SiO_2 and B_2O_2. *Journal of the American Ceramic Society*, 19:202–206, 1936.

[93] B. E. Warren and J. Biscoe. The Structure of Silica Glass by X-ray Diffraction Studies. *Journal of the American Ceramic Society*, 21:49–54, 1938.

[94] R. Kaplow, T. A. Rowe, and B. L. Averbach. Atomic Arrangement in Vitreous Selenium. *Physical Review*, 168:1068, 1968.

[95] H. P. Klug and L. E. Alexander. *X-ray Diffraction Proceedures for Polycrystalline and Amorphous Materials*. Wiley New York, 2nd edition, 1974.

[96] D. D. Kofalt, S. Nano, K.-M. Wong, and S. J. Poon. Differential Anomalous-X-ray-scattering Studies of Icosahedral and Amorphous Palladiumuranium-silicon ($Pd_{58.8}U_{20.6}Si_{20.6}$). *Physical Review Letters*, 57:114–117, 1986.

[97] V. Petkov, I.-K. Jeong, J. S. Chung, M. F. Thorpe, S. Kycia, and S. J. L. Billinge. High Real-space Resolution Measurements of the Local Structure of $Ga_{1-x}In_xAs$ Using X-ray Diffraction. *Physical Review Letters*, 83:4089–4092, 1999.

[98] P. J. Chupas, X. Y. Qiu, J. C. Hanson, P. L. Lee, C. P. Grey, and S. J. L. Billinge. Rapid-acquisition Pair Distribution Function (RA-PDF) Analysis. *Journal of Applied Crystallography*, 36:1342–1347, 2003.

[99] V. Petkov, S. J. L. Billinge, S. D. Shastri, and B. Himmel. Polyhedral Units and Network Connectivity in Calcium Aluminosilicate Glasses from High Energy X-ray Diffraction. *Physical Review Letters*, 85(16):3436–3439, 2000.

[100] V. Petkov, S. J. L. Billinge, P. Larson, S. D. Mahanti, T. Vogt, K. K. Rangan, and M. G. Kanatzidis. Structure of Nanocrystalline Materials Using Atomic Pair Distribution Function Analysis: Study of $LiMoS_2$. *Physical Review*, B65:092105, 2002.

[101] S. J. L. Billinge, T. Dykhne, P. Juhas, E. Bozin, R. Taylor, A. J. Florence, and K. Shankland. Characerisation of Amorphous and Nanocrystalline Molecular Materials by Total Scattering. *CrystEngComm*, 12:1366–1368, 2010.

[102] D. Prill, P. Juhas, M. U. Schmidt, and S. J. L. Billinge. Modelling Pair Distribution Functions (PDFs) of Organic Compounds: Describing Both Intra- and Intermolecular Correlation Functions in Calculated PDFs. *Journal of Applied Crystallography*, 48:171–178, 2015.

[103] K. Nagashio, Y. Takamura, and K. Kuribayashi. Containerless Solidification of Peritectic and Eutectic Ceramics Using Aero-acoustic Levitator. *Materials Science Forum*, 329-330:173–178, 2000.

[104] Y. Cerenius, A. Oskarsson, S. Santesson, S. Nilsson, and L. Kloo. Preliminary Tests on the Use of an Acoustic Levitator for Liquid X-ray Diffraction Experiments. *Journal of Applied Crystallography*, 36:163–164, 2003.

[105] S. E. Wolf, J. Leiterer, V. Pipich, R. Barrea, F. Emmerling, and W. Tremel. Strong Stabilization of Amorphous Calcium Carbonate Emulsion by Ovalbumin: Gaining Insight into the Mechanism of 'Polymer-Induced Liquid Precursor' Processes. *Journal of the American Chemical Society*, 133(32):12642–12649, 2011.

[106] A. Smekal. Zur Quantentheorie der Dispersion. *Naturwissenschaften*, 11(43):873–875, 1923.

[107] T. Hirschfeld and B. Chase. FT-Raman Spectroscopy: Development and Justification. *Applied Spectroscopy*, 40(2):133–137, 1986.

[108] A. Biswas. Solidification of Acoustically Levitated o-Terphenyl Crystsals: A Raman Study. *Journal of Crystal Growth*, 147:155–164, 1995.

[109] A. N. Davies, P. Jacob, A. Stockhaus, R. Kuckuk, W. Hill, R. Hergenroder, A. Zybin, and D. Klockow. Acoustic Trap for Simplified Micro-sample Handling in Laser Spectroscopy. *Applied Spectroscopy*, 54(12):1831–1836, 2000.

[110] R. Tuckermann, L. Puskar, M. Zavabeti, R. Sekine, and D. McNaughton. Chemical Analysis of Acoustically Levitated Drops by Raman Spectroscopy. *Analytical and Bioanalytical Chemistry*, 394:1433–1441, 2009.

[111] C. Esen, T. Weigel, V. Sprynchak, and G. Schweiger. Raman Spectroscopy on Deformed Droplets: Theory and Experiment. *Journal of Quantitative Spectroscopy & Radiative Transfer*, 89:79–85, 2004.

[112] S. Biedasek, M. Abboud, H.-U. Moritz, and A. Stammer. Online-analysis on Acoustically Levitated Droplets. *Macromolecular Symposia*, 259:390–396, 2007.

[113] M. Lopez-Pastor, A. Dominguez-Vidal, J. Ayora-Canada, T. Laurell, M. Valcarcel, and B. Lendl. Containerless Reaction Monitoring in Ionic Liquis by Means of Raman Microspectroscopy. *Lab on a Chip*, 7(1):126–132, 2007.

[114] M. J. O'neill and E. S. Watson. Differential microcalorimeter, 1966.

[115] M. J. O'neill. Measurement of Specific Heat Functions by Differential Scanning Calorimetry. *Analytical Chemistry*, 38(10):1331–1336, 1966.

[116] B. Perrenot and G. Widmann. Polymorphism by Differential Scanning Calorimetry. *Thermochimica Acta*, 234:31–39, 1994.

[117] S. Qi, P. Avalle, R. Saklatvala, and D. Q. M. Craig. An Investigation into the Effect of Thermal History on the Crystallisation Behaviour of Amorphous Paracetamol. *European Journal of Pharmaceutics and Biopharmaceutics*, 69:364–371, 2008.

[118] A. W. Coats and J. P. Redfern. Thermogravimetric Analysis. A Review. *Analyst*, 88:906–924, 1963.

[119] W. Nernst and E. H. Riesenfeld. Über quantitative Gewichtsanalyse mit sehr kleinen Substanzmengen. *European Journal of Inorganic Chemistry*, 36(2):2086–2093, 1903.

[120] A. Joseph, C. E. S. Bernardes, A. S. Viana, M. F. Minas da Piedade, and M. E. Minas da Piedade. Kinetics and Mechanism of the Thermal Dehydration of a Robust and Yet Metastable Hemihydrate of 4-Hydroxynicotinic Acid. *Crystal Growth & Design*, 15:3511–3524, 2015.

[121] C. E. S. Bernardes, M. E. Minas da Piedade, and J. N. Canongia Lopes. The Structure of Aqueous Solutions of a Hydrophilic Ionic Liquid: The Full Concentration Range of 1-Ethyl-3-methylimidazolim Ethylsulfate and Water. *The Journal of Physical Chemistry B*, 115:2067–2074, 2011.

[122] K. Shimizu, C. E. S. Bernardes, and J. N. Canongia Lopes. Structure and Aggregation in the 1-Alkyl-3-methylimidazolium Bis(trifluoromethylsulfonyl)imide Ionic Liquid Homologous Series. *The Journal of Physical Chemistry B*, 118(2):567–576, 2014.

[123] C. E. S. Bernardes, K. Shimizu, A. I. M. C. L. Ferreira, L. M. N. B. F. Santos, and J. N. Canongia Lopes. Structure and Aggregation in the 1,3-Dialkyl-imidazolium Bis(trifluoromethylsulfonyl)imide Ionic Liquid Family: 2. From Single to Double Long Alkyl Side Chains. *The Journal of Physical Chemistry B*, 118(24):6885–6895, 2014.

[124] C. E. S. Bernardes. AGGREGATES: Finding Structures in Simulation Results of Solutions. *Journal of Computational Chemistry*, 38:753–765, 2017.

[125] R. J. Davey, S. L. M. Schröder, and J. H. ter Horst. Nucleation of Organic Crystals - A Molecular Perspective. *Angewandte Chemie International Edition*, 52:2166–2179, 2013.

[126] D. O. Calligaro, J. Fairhurst, T. M. Hotten, N. A. Moore, and D. E. Tupper. The Synthesis and Biological Activity of Some Known and Putative Metabolites of the Atypical Antipsychotic Agent Olanzapine (LY170053). *Bioorganic & Medicinal Chemistry Letters*, 7(1):25–30, 1997.

[127] L. Yu. Polymorphism in Molecular Solids: An Extraordinary System of Red, Orange, and Yellow Crystals. *Accounts of Chemical Research*, 43(9):1257–1266, 2010.

[128] L. Yu, G. A. Stephenson, C. A. Mitchell, C. A. Bunnell, S. V. Snorek, J. J. Bowyer, T. B. Borchardt, and S. R. Stowell, J. G.; Byrn. Thermochemistry and Coformational Polymorphism of a Hexamorphic Crystal System. *Journal of the American Chemical Society*, 122:585–591, 2000.

[129] C. A. Mitchell, L. Yu, and M. D. Ward. Selective Nucleation and Discovery of Organic Polymorphs through Epitaxy with Single Crystal Substrates. *Journal of the American Chemical Society*, 123:10830–10839, 2001.

[130] S. Chen, I. A. Guzei, and L. Yu. New Polymorphs of ROY and New Record for Coexisting Polymorphs of Solved Structures. *Journal of the American Chemical Society*, 127(27):9881–9885, 2005.

[131] S. Chen, H. Xi, and L. Yu. Cross Nucleation between ROY Polymorphs. *Journal of the American Chemical Society*, 127:17439–17444, 2005.

[132] G. A. Stephenson, T. B. Borchardt, S. R. Byrn, J. Bowyer, C. A. Bunnell, S. V. Snorek, and L. Yu. Conformational and Color Polymorphism of 5-Methyl-2-(2-nitrophenyl)amino-3-thiophenecarbonitrile. *Journal of Pharmaceutical Sciences*, 84 (11):1385–1386, 1995.

[133] M. Haisa, S. Kashino, R. Kawai, and H. Maeda. The Monoclinic Form of p-Hydroxyacetanilide. *Acta Crystallographica Section B-Structural Science*, 32:1283–1285, 1976.

[134] M. Haisa, S. Kashino, and H. Maeda. The Orthorhombic Form of p-Hydroxyacetanilide. *Acta Crystallographica Section B-Structural Science*, 30:2510–2512, 1974.

[135] M.-A. Perrin, M. A. Neumann, H. Elmaleh, and L. Zaske. Crystal Structure Determination of the Elusive Paracetamol Form III. *Chemical Communications*, (22): 3181–3183, 2009.

[136] X. Chen, K. R. Morris, U. J. Griesser, S. R. Byrn, and J. G. Stowell. Reactivity Differences of Indomethacin Solid Forms with Ammonia Gas. *Journal of the American Chemical Society*, 124(50):15012–15019, 2002.

[137] L. Borka. The Polymorphism of Indomethacine. New Modifications, their Melting Behavior and Solubility. *Acta Pharmaceutica Suecica*, 11(3):295–303, 1974.

[138] T. J. Kistenmacher and R. E. Marsh. Crystal and Molecular Structure of an Antiinflammatory Agent Indometahacin, 1-(p-Chlorobenzoyl)-5-methoxy-2-methylindole-3-acetic Acid. *Journal of the American Chemical Society*, 94(4):1340–1345, 1972.

[139] S. A. Surwase, J. P. Boetker, D. Saville, B. J. Boyd, K. C. Gordon, L. Peltonen, and C. J. Strachan. Indomethacin: New Polymorphs of an Old Drug. *Molecular Pharmaceutics*, 10(12):4472–4480, 2013.

[140] H. N. Morse. Über eine neue Darstellungsmethode der Acetylamidophenole. *Berichte der deutschen chemischen Gesellschaft*, 11(1):232–233, 1878.

[141] G. Nichols and C. S. Frampton. Physicochemical Characterization of the Orthorhombic Polymorph of Paracetamol Crystallized from Solution. *Journal of Pharmaceutical Sciences*, 87(6):684–693, 1998.

[142] M. D. Lang, A. L. Grzesiak, and A. J. Matzger. The Use of Polymer Heteronuclei for Crystalline Polymorph Selection. *Journal of the American Chemical Society*, 124:14834–14835, 2002.

[143] A. Burger. Zur Interpretation von Polymorphie-Untersuchungen. *Acta Pharmaceutica Technologica*, 28:1–20, 1982.

[144] M. L. Peterson, S. L. Morissette, C. McNulty, A. Goldsweig, P. Shaw, M. LeQuesne, J. Monagle, N. Encina, J. Marchionna, A. Johnson, J. Gonzalez-Zugasti, A. V. Lemmo, S. J. Ellis, M. J. Cima, and O. Almarson. Iterative High-throughput Polymorphism Studies on Acetaminophen and an Experimentally Derived Structure for Form III. *Journal of the American Chemical Society*, 124(37):10958–10959, 2002.

[145] F. D. Hart and P. L. Boardman. Indomethacin - A New Non-steroid Anti-inflammatory Agent. *British Medical Journal*, 2(5363):965–970, 1963.

[146] S. Y. Lin. Isolation and Solid-state Characteristics of a New Crystal Form of Indomethacin. *Journal of Pharmaceutical Sciences*, 81(6):572–576, 1992.

[147] S. Y. Lin, K. S. Chen, and H. S. Teng. Effect of Protective Colloids on the Induction of Polymorphic Changes in Indomethacin Agglomerates After Solvent Evaporation from o/w Emulsions. *Journal of Microencapsulation*, 16(1):39–47, 1999.

[148] K. J. Crowley and G. Zografi. Cryogenic Grinding of Indomethacin Polymorphs and Solvates: Assessment of Amorphous Phase Formation and Amorphous Phase Physical Stability. *Journal of Pharmaceutical Sciences*, 91(2):492–507, 2002.

[149] P. A. Slavin, D. B. Sheen, E. E. A. Shepherd, J. N. Sherwood, N. Feeder, R. Docherty, and S. Milojevic. Morphological Evaluation of the gamma-Polymorph of Indomethacin. *Journal of Crystal Growth*, 237:300–305, 2002.

[150] P. J. Cox and P. L. Manson. Indomethacin tert-Butanol Solvate at 120 K. *Acta Crystallographica Section E*, 59(8):o1189–o1191, 2003.

[151] J. G. Stowell, S. R. Byrn, G. Zografi, and M. Yoshioka. *Private Communication*, 2002.

[152] O. Paris, C. H. Li, S. Siegel, G. Weseloh, F. Emmerling, H. Riesemeier, A. Erko, and P. Fratzl. A New Experimental Station for Simultaneous X-ray Microbeam Scanning for Small- and Wide-angle Scattering and Fluorescence at BESSY II. *Journal of Applied Crystallography*, 40:S466–S470, 2007.

[153] K. S. Wallwork, B. J. Kennedy, and D. Wang. The High Resolution Powder Diffraction Beamline for the Australian Synchrotron. *AIP Conference Proceedings*, 879(1): 879–882, 2007.

[154] P. R. Willmott, D. Meister, S. J. Leake, A. Bergamaschi, M. Böge, M. Calvi, C. Cancellieri, N. Casati, A. Cervellino, Q. Chen, C. David, U. Flechsig, F. Gozzo, B. Henrich, S. Jäggi-Spielmann, B. Jakob, I. Kalichava, P. Karvinen, J. Krempasky, A. Lüdeke, R. Lüscher, S. Maag, C. Quitmann, M. L. Reinle-Schmitt, T. Schmidt, B. Schmitt, A. Streun, I. Vartiainen, M. Vitins, X. Wang, and R. Wullschleger. The Materials Science Beamline Upgrade at the Swiss Light Source. *Journal of Synchrotron Radiation*, 20:667–682, 2013.

[155] A. P. Hammersley, S. O. Svensson, M. Hanfland, A. N. Fitch, and D. Hausermann. Two-dimensional Detector Software: From Real Detector to Idealised Image or Two-theta Scan. *High Pressure Research*, 14(4-6):235–248, 1996.

[156] P. Juhas, T. Davis, C. L. Farrow, and S. J. L. Billinge. PDFgetX3: A Rapid and Highly Automatable Program for Processing Powder Diffraction Data into Total Scattering Pair Distribution Functions. *Journal of Applied Crystallography*, 46:560–566, 2013.

[157] W. I. F. David, K. Shankland, J. van de Streek, E. Pidcock, W. D. S. Motherwell, and J. C. Cole. DASH: A Program for Crystal Structure Determination from Powder Diffraction Data. *Journal of Applied Crystallography*, 39:910–915, 2006.

[158] A. Boultif and D. Louer. Indexing of Powder Diffraction Patterns for Low-symmetry Lattices by the Successive Dichotomy Method. *Journal of Applied Crystallography*, 24:987–993, 1991.

[159] Topas Version 5. General Profil and Structure Analysis Software for Powder Diffraction Data (User Manual). *Bruker AXS: Karlsruhe*, 1999-2014.

[160] H. M. Rietveld. Line Profiles of Neutron Powder-diffraction Peaks for Structure Refinement. *Acta Crystallographica*, 22(151-152):151–152, 1967.

[161] H. M. Rietveld. A Profile Refinement Method for Nuclear and Magnetic Structures. *Journal of Applied Crystallography*, 2:65–71, 1969.

[162] I. T. Todorov, W. Smith, K. Trachenko, and M. T. Dove. DL POLY 3: New Dimensions in Molecular Dynamics Simulations via Massive Parallelism. *Journal of Materials Chemistry*, 16:1911–1918, 2006.

[163] L. Martinez, R. Andrade, E. G. Birgin, and J. M. Martinez. PACKMOL: A Package for Building Initial Configuration for Molecular Dynamics Simulations. *Journal of Computational Chemistry*, 30(13):2157–2164, 2009.

[164] C. E. S. Bernardes and A. Joseph. Evaluation of the OPLS-AA Force Field for the Study of Structural and Energetic Aspects of Molecular Organic Crystals. *The Journal of Physical Chemistry A*, 119:3023–3034, 2015.

[165] W. L. Jorgensen, D. S. Maxwell, and J. Tirado-Rives. Development and Testing of the OPLS All-Atom Force Field on Conformational Energetics and Properties of Organic Liquids. *Journal of the American Chemical Society*, 118:11225–11236, 1996.

[166] G. Kaminski and W. L. Jorgensen. Performance of the AMBER94, MMFF94, and OPLS-AA Force FField for Modeling Organic Liquids. *The Journal of Physical Chemistry*, 100(46):18010–18013, 1996.

[167] R. A. Granberg and A. C. Rasmuson. Solubility of Paracetamol in Pure Solvents. *Journal of Chemical and Engineering Data*, 44(6):1391–1395, 1999.

[168] R. L. Sobocinski and J. E. Pemberton. Determination of Alcohol Solvent Orientation and Bonding at Silver Electrodes Using Surface-enhanced Raman-scattering - Methanol, Ethanol, 1-Propanol, and 1-Pentanol. *Langmuir*, 8(8):2049–2063, 1992.

[169] A. Luczak, L. J. Jallo, R. N. Dave, and Z. Iqbal. Polymorph Stabilization in Processed Acetaminophen Powders. *Powder Technology*, 236:52–62, 2013.

[170] K. Nollenberger, A. Gryczke, Ch. Meier, J. Dressman, M. U. Schmidt, and S. Brühne. Pair Distribution Function X-ray Analysis Explains Dissolution Characteristics of Felodipine Melt Extrusion Products. *Journal of Pharmaceutical Sciences*, 98(4):1476–1486, 2009.

[171] B. A. Kolesov, M. A. Mikhailenko, and E. V. Boldyreva. Dynamics of the Intermolecular Hydrogen Bonds in the Polymorphs of Paracetamol in Relation to Crystal Packing and Conformational Transitions: A Variable-temperature Polarized Raman Spectroscopy Study. *Physical Chemistry Chemical Physics*, 13(31):14243–14253, 2011.

[172] E. B. Burgina, V. P. Baltakhinov, E. V. Boldyreva, and T. P. Shakhtschneider. IR Spectra of Paracetamol and Phenacetin. 1. Theoretical and Experimental Studies. *Journal of Structural Chemistry*, 45(1):64–73, 2004.

[173] F. E. Malherbe and H. J. Bernstein. The Infrared and Raman Spectra of p-Dioxane. *Journal of the American Chemical Society*, 74(17):4408–4410, 1952.

[174] J. Y. Kao, C. M. McGoverin, K. A. Graeser, T. Rades, and K. C. Gordon. Measurement of Amorphous Indomethacin Stability with NIR and Raman Spectroscopy. *Vibrational Spectroscopy*, 58:19–26, 2012.

[175] J. I. Langford and D. Louer. Powder Diffraction. *Reports on Progress in Physics*, 59:131–234, 1996.

[176] C. J. Strachan, T. Rades, and K. C. Gordon. A Theoretical and Spectroscopic Study of gamma-Crystalline and Amorphous Indometacin. *Journal of Pharmacy and Pharmacology*, 59(2):261–269, 2007.

[177] H. Yamamoto. A New Syntheses of 1-(p-Chlorobenzoyl)-5-methoxy-3-indolylacetic Acid and its Polymorphism. *Chemical and Pharmaceutical Bulletin*, 16(1):17–19, 1968.

[178] V. Majer and V. Svoboda. *Enthalpies of Vaporization of Organic Compounds: A Critical Review and Data*. Blackwell Scientific, Oxford, 1985.

[179] F. Vesely, L. Svab, R. Provaznik, and V. Svoboda. Enthalpies of Vaporization at High-Pressures for Methanol, Ethanol, Propan-1-ol, Propan-2-ol, Hexane, and Cyclohexane. *Journal of Chemical Thermodynamics*, 20(8):981–983, 1988.

[180] B. Nicolai, R. Ceolin, and I. B. Rietveld. Polymorphism and Solvation of Indomethacin. *Journal of Thermal Analysis and Calorimetry*, 102(1):211–216, 2010.

[181] G. Brenn, L. J. Deviprasath, F. Durst, and C. Fink. Evaporation of Acoustically Levitated Multi-component Liquid. *International Journal of Heat and Mass Transfer*, 50:5073–5086, 2007.

[182] R. Tuckermann, S. Bauerecker, and B. Neidhart. Schwebende Tröpfchen. *Angewandte Physik: Physik in unserer Zeit*, 32:69–75, 2001.

[183] C. M. Hansen. *Hansen Solubility Parameters: A User's Handbook*. CRC Press, 2007.

[184] I. D. H. Oswald, D. R. Allan, P. A. McGregor, W. D. S. Motherwell, S. Parsons, and C. R. Pulham. The Formation of Paracetamol (Acetaminophen) Adducts with Hydrogen-bond Acceptors. *Acta Crystallographica Section B-Structural Science*, 58: 1057–1066, 2002.

[185] S. K. Wolff, D. J. Grimwood, J. J. McKinnon, M. J. Turner, D. Jayatilaka, and M. A. Spackman. CrystalExplorer 3.1. *University of Western Australia, Perth*, 2012.

[186] J. J. McKinnon, D. Jayatilaka, and M. A. Spackman. Toward Quantitative Analysis of Intermolecular Interactions with Hirshfeld Surfaces. *CrystEngComm*, pages 38814–3816, 2007.

[187] M. A. Spackman and Jayatilaka. Hirshfeld Surface Analysis. *CrystEngComm*, 11: 19–32, 2009.

[188] D.-H. Kang, H. Zhang, H. Yoo, H. H. Lee, S. Lee, G. W. Lee, H. Lou, X. Wang, Q. Cao, D. Zhang, and J. Jiang. Interfacial Free Energy Controlling Glass-forming Ability of Cu-Zr Alloys. *Scientific Reports*, 4:5167, 2014.

[189] K. S. Vahvaselka, R. Serimaa, and M. Torkkeli. Determination of Liquid Structures of the Primary Alcohols Methanol, Ethanol, 1-Propanol, 1-Butanol and 1-Octanol by X-ray Scattering. *Journal of Applied Crystallography*, 28:189–195, 1995.

[190] M. Haughney, M. Ferrario, and I. R. McDonald. Molecular Dynamics Simulation of Liquid Methanol. *The Journal of Physical Chemistry*, 91:4934–4940, 1987.

[191] B. A. Hendriksen and D. J. W. Grant. The Effect of Structurally Related Substances on the Nucleation Kinetics of Paracetamol (Acetaminophen). *Journal of Crystal Growth*, 156:252–260, 1995.

[192] L. Yu. Color Changes Caused by Conformational Polymorphism: Optical-crystallography, Single-crystal Spectroscopy, and Computational Chemistry. *Journal of Physical Chemistry A*, 106(3):544–550, 2002.

Danksagung

Die vorliegende Arbeit wurde im Rahmen des Schwerpunktprogramms SPP1415 „Kristalline Nichtgleichgewichtsphasen (KNG) - Präparation, Charakterisierung und in-situ-Untersuchung der Bildungsmechanismen“ der Deutschen Forschungsgemeinschaft (DFG) angefertigt. Ich bedanke mich bei der DFG für die finanzielle Unterstützung und die Möglichkeit, ein Teil des Projektes bearbeiten zu dürfen. Ich danke ebenfalls dem „COST Action CM1402“-Projekt für die Finanzierung des wissenschaftlichen Aufenthaltes an der Universität Lissabon in Portugal. Die Arbeit wurde an der Bundesanstalt für Materialforschung und -prüfung im Fachbereich 1.3 Strukturanalytik durchgeführt.
Meinem Betreuer Prof. Rademann möchte ich für die Erstellung des Erstgutachtens und den zielführenden, wissenschaftlichen Austausch danken. Prof. Kolb und Prof. Balasubramanian danke ich ebenfalls für die Erstellung der Gutachten.
Mein besonderer Dank gilt vor allem Dr. Franziska Emmerling für die außergewöhnliche Betreuung und die unermüdliche Unterstützung während der gesamten Zeit. Vor allem bin ich für die Freiheiten und das entgegengebrachte Vertrauen dankbar, die meine Entwicklung auf wissenschaftlicher und persönlicher Ebene vorantrieben haben.
Allen Kollegen der gesamten Arbeitsgruppe 1.3 danke ich für die enge Zusammenarbeit und die fruchtbare Arbeitsatmosphäre. Besonders möchte ich an der Stelle Carsten Prinz, Dr. Ralf Bienert, Klaus-Jürgen Wenzel und den restlichen Mitstreitern für die tatkräftige Unterstützung und Hilfsbereitschaft während den Synchrotron-Messzeiten danken. Ohne euch hätte es nur halb so viel Spaß gemacht.
Prof. Minas da Piedade und Dr. Carlos Bernardes danke ich für die anregende, wissenschaftliche Kooperation und den lehrreichen Aufenthalt in Lissabon.
Großer Dank gebührt meiner Familie, insbesondere meinem Freund Fritz. Danke für die lieben Worte und Unterstützung in jeglicher Hinsicht.

Selbstständigkeitserklärung

Ich erkläre, dass ich die vorliegende Dissertation selbstständig und nur unter Verwendung der von mir gemäß §7 Absatz 3 der Promotionsordnung der Mathematisch - Naturwissenschaftlichen Fakultät, veröffentlich im Amtlichen Mitteilungsblatt der Humboldt-Universität zu Berlin Nr. 126/2014 am 18. November 2014, angegebenen Hilfsmittel angefertigt habe.